

Imperial College of Science, Technology and Medicine
Department of Electrical and Electronic Engineering

Impedance Model Analysis and Measurement for Power System Stability

Yue Zhu

Submitted in part fulfilment of the requirements for
the degree of Doctor of Philosophy and for the Diploma
of Imperial College London, 04 August 2022

Abstract

Electric power systems are transforming from synchronous machine (SG) dominated systems to composite grids in which inverter-based resources (IBRs) coexist with SGs. The lack of standardisation of IBRs leads vendors to treat their control algorithms as commercial secrets and they are willing to disclose only black-box models that give input-output relationships but no internal details. An impedance model spectrum is commonly put forward as a black-box model useful for stability analysis.

Several types of impedance models have been proposed to represent the dynamic characteristics of a complete power networks. A study is undertaken to compare two types of networked impedance models: those based on direct nodal or loop analysis and those based on a whole-system formulation. The underlying relationship between eigenvalues of the impedance matrix and the oscillatory modes of the network for both model types have been unclear but are resolved here and the relative merits of the models are established.

Through examining eigenvalue sensitivity, a proposal is made for an impedance participation factor that can identify root-causes of low damping. It is proved that the impedance participation factor is related to the classic state-space participation via a chain-rule relationship. Based on the chain-rule, a grey-box approach is developed as a generic method for root-cause tracing in impedance models. It has three degrees of transparency according to the available information and they are aggregated participation, damping contribution, and key parameters. The grey-box approach can indicate appropriate re-tuning of parameters that would shift the oscillatory mode in a desired direction in complex plain so as to stabilise the system. The theoretical contributions are verified through three different scales of case study: a simple three-node passive circuit, a modified IEEE 14-bus system and a modified NETS-NYPS 68-bus system.

A significant advantage of using an impedance model is that the model can, in principle, be measured online with injection of a small-signal perturbation. However, a vital issue of concern is error caused by noise in the measured signals since this will determine the magnitude of injected perturbation required and the practicality of arranging that. To address this issue, a noise analysis process for impedance measurement is proposed in this thesis, from which guidance on selecting an appropriate injection magnitude can be provided. To verify the proposed analysis process, a power-hardware-in-the-loop system is built where a high-bandwidth power amplifier (OP1400 series) is used to inject the perturbation.

The theoretical developments and noise analysis presented in this thesis combine to offer stability analysis and root-cause tracing of the type normally found only in white box state-space models but here are available in models built from equipment manufacturers' black-box models or from measurement-based models.

Acknowledgements

I am very pleased to have this opportunity to give my acknowledgements to all the people who have contributed to my work and have supported me during my PhD.

I would like to express my sincere gratitude to my supervisor, Prof. Timothy C. Green, for his continuous support, guidance and supervision through out my time at Imperial College London. His profound knowledge, rigorous attitude, and passion toward research will benefit my entire career as well as my whole personal life.

I am very grateful to my co-supervisor, as well as a good friend, Dr Yunjie Gu, for his constructive guidance on my research and great support in all aspects. I also want to thank my colleague, Dr Yitong Li, for the technical suggestions I have received from him. I am thankful to Prof. Xin Xiang for hosting my research visit to Zhejiang University. Special thanks to Mr Yifan Zhang for helping me with the experiments.

I am highly honoured to have Prof. Janusz Bialek and Dr Balarko Chaudhuri as my PhD viva examiners. I am very thankful to them for the useful discussions and valuable feedback on my thesis. I would also like to thank my PhD milestone assessor, Dr Fei Teng, for his helpful advice on my work.

Many thanks to my colleagues at Imperial College London for their help and friendship. They are Dr Philip Clemow, Dr Adrià Junyent-Ferré, Dr Joan Marc Rodríguez Bernuz, Dr Caspar Collins, Dr Enrique Ortega Calderon, Dr Kathryn Wills, Ms Eugenie Ducoin, Mr Nikhil Singh, Mr Fredrik Smith, Mr Mohamed Aldarmon, Mr Chengwei Liu, Mr Jintao Guo and all my other colleagues. I would also like to thank all my friends in UK and China for the enjoyable time we have spent.

Last, but most importantly, I would like to thank my wife Dr Yubing Hu and my parents Mr Xuebing Zhu and Ms Jianhong Niu, for their immense support and endless love.

Statement of Originality

I, Yue Zhu, confirm that this work is the result of my own endeavor, and all work undertaken by other authors is appropriately referenced.

Copyright Declaration

The copyright of this thesis rests with the author. Unless otherwise indicated, its contents are licensed under a Creative Commons Attribution-NonCommercial 4.0 International Licence (CC BY-NC).

Under this licence, you may copy and redistribute the material in any medium or format. You may also create and distribute modified versions of the work. This is on the condition that: you credit the author and do not use it, or any derivative works, for a commercial purpose.

When reusing or sharing this work, ensure you make the licence terms clear to others by naming the licence and linking to the licence text. Where a work has been adapted, you should indicate that the work has been changed and describe those changes.

Please seek permission from the copyright holder for uses of this work that are not included in this licence or permitted under UK Copyright Law.

List of Abbreviations

SG	Synchronous machine
IBR	Inverter based resource
RES	Renewable energy sources
PV	Photovoltaic
BESS	Battery energy storage systems
PSS	Power system stabilizer
SO	System operator
EMT	Electro-magnetic transient
RMS	Root-mean-square
PCC	Point of common coupling
GNC	Generalized Nyquist criterion
RMA	Resonance mode analysis
SNR	Signal-to-noise ratio
PLL	Phase locked loop
PHIL	Power hardware-in-the-Loop
HIL	Hardware-in-the-loop
DUT	Device under test
PI	Power interface
PA	Power amplifier
RTT	Real-time target
WSS	Wide-sense stationary
WGN	White Gaussian noise
PSD	Power density spectrum
FFT	Fast Fourier transform
PDF	Probability density function
AI	Artificial intelligence

Nomenclature

State-Space Related

A, a_{ki}	state-space matrix and its elements
u_{in}	vector of the input for state-space model
y_o	vector of the output for state-space model
Ψ, ψ_k	left-eigenvector matrix of A and its k -th row
Φ, ϕ_k	right-eigenvector matrix of A and its k -th column
λ	a nonspecific eigenvalue of the state-space matrix A
λ_i	the i -th eigenvalue of the state-space matrix A

Networked Impedance Related

R_{ki}	the residue of Z_{kk}^{sys} corresponding to the pole λ_i .
$S_\gamma, S_{\gamma,ki}$	critical admittance-eigenvalue sensitivity matrix and its elements
$S_\lambda, S_{\lambda,ki}$	eigenvalue sensitivity matrix and its elements
$Y^{nodal}, Y_{ki}^{nodal}$	nodal admittance model and its elements
Y^{sys}, Y_{ki}^{sys}	whole-system admittance model and its elements
$Y_{det}^{nodal}(\lambda)$	$\det(Y^{nodal}(s)) _{s=\lambda}$, the determinant of Y^{nodal} at λ
Y_A, Y_{Ak}	apparatus admittance matrix (a diagonal matrix) and its elements
Y_N, Y_{Nki}	nodal admittance matrix and its elements
Z^{loop}, Z_{ki}^{loop}	loop impedance model and its elements
Z^{sys}, Z_{ki}^{sys}	whole-system impedance model and its elements
Z_A, Z_{Ak}	apparatus impedance matrix (a diagonal matrix) and its elements
Z_{Gk}, Y_{Gk}	grid-side impedance and admittance seen from the k -th node
$p_{\lambda,Z}$	impedance participation factor
$p_{\lambda,\rho}$	parameter participation factor

$s_{\lambda,y}$	admittance sensitivity factor
$s_{\lambda,\rho}$	parameter sensitivity factor
w_γ, u_γ	left and right eigenvectors of $Y^{\text{nodal}}(\lambda)$ corresponding to γ , normalised as $w_\gamma^\top u_\gamma = 1$.
y	admittance of a non-specific component in the system
γ	critical admittance-eigenvalue, the zero-eigenvalue of $Y^{\text{nodal}}(\lambda)$
ω_r	a resonant frequency
ξ	the missing coefficient of S_γ

Nyquist-based Analysis Related

L, L_{ki}	return ratio matrix for Nyquist-based stability analysis and its elements
V_S, I_S	voltage source and current source from the source-side equivalent circuit
Z_L, Y_L	load-side impedance and admittance
Z_S, Y_S	output impedance and output admittance from the source-side equivalent circuit
$p_{i,k}$	eigenloci participation factor, the participation factor of the k -th apparatus in the i -th eigenlocus ι_i
w_ι, u_ι	left and right eigenvectors of L corresponding to ι
ι	a non-specific eigenlocus (an eigenvalue of L)
ι_i	the i -th eigenvalue of L

Impedance Measurement Related

$G_W(t)$	modelled white Gaussian noise
$H_i(t)$	modelled i -th harmonic in the noise
I_c	measured amplitude of small-signal current output at f_c
I_{c0}	true value of the amplitude of small-signal current output at f_c
N_c	errors in I_c caused by the noise
$N_M(t)$	modelled noise
$R_{nn}(l)$	autocorrelation of the noise, l is an integer
$Y_{\text{meas}}^{\text{sys}}(f_c)$	measured value of Y^{sys} at f_c
$Y_{\text{true}}^{\text{sys}}(f_c)$	true value of Y^{sys} at f_c
f_c	frequency point of the measurement
$n(t)$	measured noise

$\eta(f_c)$ relative error of the admittance measurement at f_c

Others

m number of states

n number of buses

\tilde{i}, \tilde{v} vector of input small-signal current and voltage

$\Delta i, \Delta v$ vector of output small-signal current and voltage

ρ system parameter

Math Operators

$E(\cdot)$ expected value of a random variable

$\text{Res}_\lambda(\cdot)$ residue of (\cdot) at λ

$U(0, 2\pi)$ uniform distribution between 0 and 2π

$\text{adj}(\cdot)$ adjugate of the matrix

$\text{eig}(\cdot)$ the eigenvalues of the matrix

$\text{tr}(\cdot)$ trace of the matrix

$\mathcal{N}(\mu, \sigma^2)$ normal distribution of mean μ and variance σ^2

$(\cdot)_{-\text{Re}}, (\cdot)_{-\text{Im}}$ real and imaginary part of the complex number (\cdot)

$\langle \cdot, \cdot \rangle$ Frobenius inner product

$\| \cdot \|$ Frobenius norm

\top matrix transpose

$-$ complex conjugate

$*$ conjugate transpose: $(\cdot)^* = \overline{(\cdot)}^\top$

Contents

Abstract	i
Acknowledgements	iii
Statement of Originality	v
Copyright Declaration	vii
List of Abbreviations	ix
Nomenclature	xi
1 Introduction	1
1.1 Stability Challenges with the High Penetrations of IBRs	1
1.2 Impedance Models in Three-Phase AC systems	3
1.2.1 Illustration of Impedance Model	4
1.2.2 Impedance Model of an IBR	6
1.2.3 Impedance Models for Nyquist-based Stability Assessment	12
1.3 Motivations and Objectives of this Thesis	15
1.3.1 Networked Impedance Models	15
1.3.2 Modal Analysis in Impedance Models	16
1.3.3 Errors of Impedance Measurement	17
1.3.4 Objectives of this Thesis	18
1.4 Thesis Structure	19

2	Networked Impedance Models and Comparative Study	20
2.1	Frame Alignment	21
2.2	Formulation	24
2.2.1	Nodal-loop Model	24
2.2.2	Whole-system Models	27
2.2.3	Associations	30
2.2.4	Illustration	30
2.3	Relationship between Networked Impedance and State-Space	32
2.4	Comparisons	35
2.4.1	Sensitivity/Participation Analysis	35
2.4.2	Measurability	35
2.4.3	Use with Incomplete Data	36
2.4.4	Full comparison	37
2.5	Summary	39
3	Root-cause Analysis in Networked Impedance Models	40
3.1	Review of Existing Modal Analysis Methods in Impedance Models	40
3.1.1	The Resonance mode analysis Method	41
3.1.2	Nyquist-based Participation Analysis for the Whole System	47
3.1.3	Key Research Gaps and Work Described in this Chapter	50
3.2	Participation Analysis in Impedance Models	52
3.2.1	Impedance Participation Factor	53
3.2.2	Parameter Participation Factor and the Chain Rule	55
3.3	Impedance-based Eigenvalue Sensitivity Theory	57
3.3.1	State-Space Eigenvalue Sensitivity Derived from Impedance Model	57
3.3.2	Comprehensive Theory for Root-cause Analysis	60
3.4	The Grey-box Approach	63
3.4.1	Grey-Box Layer-1	63
3.4.2	Grey-Box Layer-2	66

3.4.3	Grey-Box Layer-3	66
3.5	Practical Implementation	67
3.6	Summary	69
4	Case Studies: Applications of the Grey-box Approach	71
4.1	Three-node Passive Circuit	71
4.2	Modified IEEE 14-bus System	75
4.3	Modified NETS-NYPS 68-bus System	82
4.4	Summary	89
5	Impedance Measurement and Noise Analysis	90
5.1	Review of Impedance Measurement Techniques	90
5.1.1	Injection Topology	91
5.1.2	Injection Waveform	94
5.1.3	Work Described in this Chapter	95
5.2	Online Measurement Test Bench	95
5.2.1	Introduction of PHIL technique	96
5.2.2	Experiment Test Bench	97
5.3	Noise Analysis for Measurement	100
5.3.1	Discussion of measurement error	101
5.3.2	Methodology	104
5.4	Measurement Results	112
5.4.1	300 Hz admittance measurement	113
5.4.2	Frequency sweep for admittance measurement	115
5.5	Summary	117
6	Conclusions, Publications, and Future Work	118
6.1	Conclusions	118
6.2	List of Publications	119
6.3	Future Work	121

6.3.1	Root-cause Analysis in Hybrid Systems	121
6.3.2	Impedance Measurement Improvement	121
A	Mathematical Proofs	123
A.1	Proof of one zero-valued eigenvalue	123
A.2	Proof of critical admittance-eigenvalue	124
A.3	Proof of Lemma 1	125
A.4	Proof of Eigenvalue Sensitivity Matrix	127
A.5	proof of equation (3.31)	129
A.6	proof of Premise 5.3	130
B	Mathematical Preliminaries	132
B.1	Residue	132
B.2	Frobenius Inner Product	133
B.3	Complex Function Derivative	133
B.4	Wide-sense stationary stochastic process	134
B.5	Law of large numbers	134
B.6	Autocorrelation	135
B.7	Wiener–Khinchin theorem	136
B.8	Monte Carlo Method	136
C	Mathematical Illustrations	137
C.1	Illustration of LEMMA 1	137
D	System Data	139
D.1	Modified IEEE 14-bus System	139
D.2	Modified NETS-NYPS 68-bus System	144
D.3	Triphase 10 kVA inverter schematic	150
	Bibliography	150

List of Tables

3.1	Comparisons of different methods for power system root-cause tracing	52
4.1	critical admittance-eigenvalue sensitivity and eigenvalue sensitivity for selected components in the grey-box layer 1, 2	73
4.2	Parameter sensitivity in the grey-box layer 3 and tuning results under 5% increment	74
4.3	Grey-box layer-3: significant parameter sensitivity factors in A11, A12 and A13 with respect to 18.87 Hz mode	79
4.4	Vector fitting results: poles and residues corresponding to 18.87 Hz mode	82
4.5	Significant parameter participation factors for the three selected modes	87
5.1	Parameters of modelled noise	108

List of Figures

1.1	Line to line RMS voltage (the blue waveforms) and reactive power output (the orange waveform) from Hornsea, 10 minutes prior to the 9 August 2019 power outage in the UK, in response to a 2% voltage step change, showing that a low-damped mode had been existed [18].	2
1.2	(a) An impedance spectrum, in Bode plot form, measured at one node of a modified IEEE 14-bus network. (b) Step-response of active power at that node, showing that a 18.9 Hz oscillation can be observed which matches the peak observed in the Bode plot.	5
1.3	Small-signal impedance model of a single-phase IBR: (a) single-port illustration. (b) Thévenin equivalent circuit defining the impedance model. (c) Norton equivalent circuit defining the admittance model.	7
1.4	Small-signal impedance model of a three-phase IBR in $d-q$ frame: (a) two-port illustration. (b) IBR impedance model in $d-q$ frame. (c) IBR admittance model in $d-q$ frame.	7
1.5	(a) Illustration of the design of a droop-controlled grid-forming inverter. (b) Impedance circuit model of the grid-forming inverter [53]. <i>Copyright © 2021, IEEE.</i>	10
1.6	Positive-sequence impedance spectra of a 2 MVA BESS inverter measured by National Renewable Energy Laboratory (NREL) when it is operated in grid-following and grid-forming control modes [56]. <i>Copyright © 2019, IEEE.</i>	11
1.7	$d-d$ axis admittance spectrum of a grid-following inverter at different operating points, showing that the spectrum varies along with the change of operating points [61]. <i>Copyright © 2020, IEEE.</i>	11
1.8	Single-line diagram of Nyquist-based formulation of impedance models in power systems: (a) source-side and load-side bi-partition. (b) Thévenin equivalent circuit. (c) Norton equivalent circuit.	14
1.9	Single-line diagram of a meshed network with multiple sources, loads and branches, showing that it is difficult to separate the system into a source-side and a load-side.	14
2.1	The spectrum of impedance at the PCC of a simple interconnected ac power electronics system, showing that the model does not match with simulation results if the frames are not aligned [47]. <i>Copyright © 2020, IEEE.</i>	22

2.2	(a) Frame alignment in impedance modeling: a local swing frame is first aligned to a local steady frame, with dynamics introduced via dynamic angle ε_k , local steady frame is then aligned to the global steady frame. ε and ξ are angle differences between frames. (b) Signal flow diagram of frame-dynamics-embedding impedance transformation, showing how a local swing frame is transformed into a local steady frame [76]. <i>Copyright</i> © 2021, <i>IEEE</i>	23
2.3	Formulation of nodal-loop models: (a) nodal admittance model Y^{nodal} . (b) Loop impedance model Z^{loop}	28
2.4	Formulation of whole-system models: (a) whole-system impedance model Z^{sys} . (b) whole-system admittance model Y^{sys}	29
2.5	(a) A simple three-node system with two IBRs. (b) The formulation of Y_A and Y_N	31
2.6	Whole-system impedance model derived from state-space representation.	33
2.7	Comparisons of networked impedance models.	38
3.1	Eigenloci of $L(s)$ in an eight-node system: (a) full view, (b) zoomed-in view. ι_1 and ι_2 encircle $(-1, 0j)$ so that the system is unstable [90]. <i>Copyright</i> © 2021, <i>IEEE</i>	48
3.2	The relationship between impedance participation factor and state participation factor and the chain-rule for participation propagation.	56
3.3	Illustration of the theory for root-cause analysis in impedance models. The blocks in golden, purple and grey, as well as all the arrows in red are developed in this thesis. The noise analysis process for impedance measurement (the orange blocks) is also developed in this thesis as given in Chapter 5. The green blocks refer to the RMA method proposed previously and reviewed in Chapter 3.1.1	64
3.4	Illustration of the three-layer grey-box. In Layer-1, estimates of the potential participants are created based on the upper bound of $\Delta\lambda$ subject to $\ \Delta y\ = \epsilon\ y\ $. In Layer-2, the contribution of a participant to mode damping is estimated based on the real part of $\Delta\lambda$ subject to $\Delta y = \epsilon y$. In Layer-3, the most effective parameter within the participating apparatus is identified, and parameter re-tuning facilitated, via the admittance-parameter sensitivity.	65
4.1	3-node simple passive circuit.	72
4.2	Eigenvalue plot of the system when parameters are swept from 100% to 105% respectively.	75
4.3	Modified IEEE-14 bus system with 3 extra IBRs.	76
4.4	Bode diagram of whole system impedance Z_{kk}^{sys} at nodes with sources, presented in $d-d$ axis.	77
4.5	Grey-box layer-1 and layer-2 results for 18.87 Hz mode, showing that apparatus at nodes 11, 12 and 13, and the adjacent impedances branches have the highest participations. The layer-2 results are normalized to the sum of absolute values.	78

4.6	Oscillation propagation in the system. The circles represent the sensitivity of 18.87 Hz mode to nodes and branches, indicating the origins and the propagation of the oscillation. The circle radii are proportional to the results in the grey-box layer-1, and the filling color is determined by the sign of the real-part in layer-2.	78
4.7	Re-tuned system with an increase in current control bandwidth of A11, A12 and A13 by 20%, 50% and 28.5%, respectively: (a) Bode plot of the $d-d$ term of $Z_{12,12}^{sys}$ showing the mode reshaped as predicted; (b) Time domain simulation: active power of A12 during a 100% demand increase at bus 12 at $t=35$ s, showing significant improvement in system damping after tuning.	80
4.8	Frequency response data points taken from the spectrum of $Z_{12,12}^{sys}$ and $Z_{13,13}^{sys}$ in $d-d$ axis and the spectra of 20-order transfer functions from the vector fitting results.	81
4.9	Modified NETS-NYPS 68 bus system, with 6 extra grid-following inverters, and a grid-forming inverter replacing the synchronous machine at bus 15.	83
4.10	Bode diagram of whole system admittance \hat{Y}_{kk} at nodes with sources, presented in $d-d$ axis.	84
4.11	Participation analysis of the three under-damped modes using Layer-1 and Layer-2 of the grey-box, where the results in Layer-2 is normalized to the sum of absolute values.	85
4.12	Grey-box Layer-3 analysis for the three under-damped modes. The parameter participation factors are represented as vectors around the associated modes showing the amplitude and direction of the eigenvalue variation subject to parameter perturbations. The parameter perturbations are proportional to the original value of parameters. The number in the parentheses in the subscript of each parameter indicates the number of the apparatus being analysed.	86
4.13	Apparent power output of A11, A15 and A29 during two transients: load-61 disconnected at $t = 10$ s, and load-42 increased 5% at $t = 12$ s. (a) De-tuned system with obvious oscillations during transient process; (b) Re-tuned by increase of $K_{F(11)}$ by 100%, decrease of $K_{D(15)}$ by 60%, and increase of $f_{i(28)}$ and $f_{i(29)}$ each by 50%, giving significant improvement in system stability; (c) Counter-tuned by increase of $K_{D(15)}$ by 50% leading to instability.	88
4.14	Eigenvalue plot of the 68-bus system before and after tuning the parameters, showing that mode-1,2,3 are shifted leftwards as predicted.	89
5.1	Small-signal injection topologies for impedance or admittance measurement: (a) independent current injection source. (b) Independent voltage injection source. (c) Noninvasive current injection from grid-following inverter. (d) Noninvasive voltage injection from grid-forming inverter.	92
5.2	Basic configuration of PHIL system [134]. <i>Copyright</i> © 2016, IEEE.	97
5.3	Single-line diagram of the three-phase experiment: (a) illustration of the aiming tested system. (b) Configuration of the tested system in PHIL platform.	99
5.4	Experiment platform for the system.	99

5.5	Method of noise analysis and injection determination for impedance or admittance measurement.	104
5.6	Waveform of d -axis current, with sample rate of 20 kHz on two timescales. Abundant noises can be observed.	105
5.7	(a) Autocorrelation of the noise: the diamond shape is in accordance with the feature of WSS process. The value at 0 is 0.01099, which is the total power of the noise. Harmonics of various frequencies are seen in the autocorrelation. (b) PSD of the noise, showing the power of each harmonic.	107
5.8	Measured noise and the modelled noise, showing that the two are closely similar. . .	108
5.9	Histogram of noise impact on admittance measurements from 1 Hz to 1 kHz.	110
5.10	PDF of noise impact based on kernel density estimation.	111
5.11	Absolute error caused by noise plotted at the 95% confidence level, i.e., there is 95% probability that the error is smaller than the value indicated by this curve.	112
5.12	Repeated tests of 300 Hz injection captured as oscilloscope screenshots. (a) A series of injections with random intervals. The yellow waveform is the injected signal on d axis voltage \tilde{v} , green is the phase-a voltage, blue is the phase-a current, magenta is the d axis current i_d . (b) Zoomed in view, showing that \tilde{v} is not obvious in the overall voltage v_a voltage, but clearly causes a current perturbation in i_a and i_d . The system is also stable during the injections.	114
5.13	Histogram of relative errors from 1000 tests showing that the measurement errors are all confined within 12%.	115
5.14	Bode plots acquired from frequency sweeps under different injection amplitude: (a) 15 V injection amplitude. (b) 10 V injection amplitude. (c) 5 V injection amplitude. (d) 2 V injection amplitude.	116
D.1	Triphase 10 kVA inverter schematic.	151

Chapter 1

Introduction

1.1 Stability Challenges with the High Penetrations of IBRs

The deployment of renewable energy sources (RES) is progressing rapidly around the world. In 2020, RES generated an estimated 29.0% of global electricity, up from 27.3% in 2019 [1]. By 2021, renewable electricity generation had expanded by more than 8% to reach 8,300 TWh, the fastest year-on-year growth since the 1970s [2]. On 29 January 2021, wind generation in the UK reached 19.6 GW, which was the highest ever share of the electricity mix across the country at 66.2% [3]. Not only is this remarkable for the growth in renewable energy but also, because wind, photovoltaic (PV) and battery energy storage system (BESS) generation use inverters to export power, inverter-based resources (IBRs) are replacing synchronous generators (SGs) and becoming the dominant sources in power systems [4].

Although IBR facilitates remarkable climate change mitigation and economic benefits, the high level of IBRs in power systems is causing stability challenges. Instabilities induced by IBRs are observed worldwide and the characteristics are evidently different to those of SG-dominated grids including the issue of harmonic pollution in the grid [5–15]. A recent example is that on 9 August 2019, following a lightning strike, two modules in Hornsea 1 wind farm deloaded from around 737 MW to zero due to a technical fault which included oscillatory behaviour and contributed to a large-scale power outage in the UK [16, 17]. According to the technical report from Ørsted, the company who runs Hornsea 1,

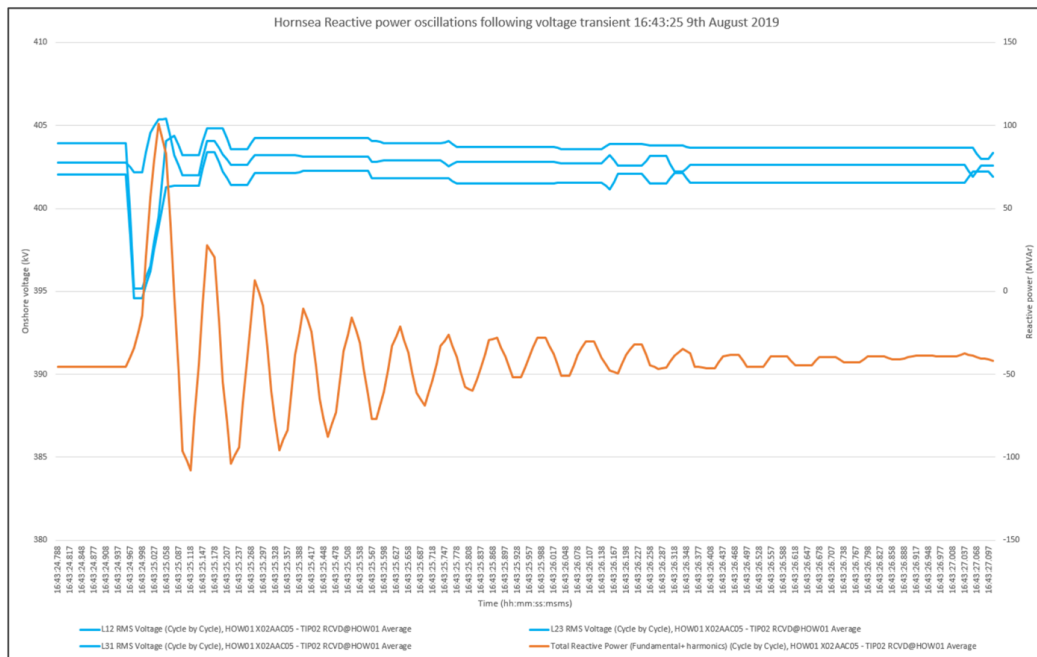


Figure 1.1: Line to line RMS voltage (the blue waveforms) and reactive power output (the orange waveform) from Hornsea, 10 minutes prior to the 9 August 2019 power outage in the UK, in response to a 2% voltage step change, showing that a low-damped mode had been existed [18].

this deload was a knock-on effect caused by insufficient damping of resonance: the lightning strike triggered oscillatory response in the wind farm system, which in turn caused unexpected wind farm control response, which further led to the wind farm deload [18]. In the investigation of this event, oscillations were also spotted at Hornsea 1 wind farm during a 2% voltage step change 10 minutes prior to the blackout event, as shown in Fig. 1.1. Such oscillations indicate that a low-damped mode had been existed in the system before the power outage happened. Although Ørsted stated that this was the first time such oscillations had led to a deload of a windfarm, it is crucial to recognise that low-damped modes in an IBR dominated system are risks to system stability. To this end, it is important to assess the system stability, to identify the potential risks (low-damped modes) and tune the system to increase the damping to avoid such events.

For conventional grids, state-space modelling is the mainstream approach for stability assessment. Typically, state-space models can be used for identifying instability (through eigenvalue mapping) [19–23], for tracing the root-cause of instability (through eigenvalue sensitivity and participation factors) [24–27] and for damping design (through pole-placement, linear matrix inequalities etc) [28–30]. The establishment of a state-space model relies on a set of state variables and parameters combined in

the equations that describe the dynamics of each of the components in the system. As a result, state-space modelling requires the full-knowledge of the system and is considered to be an open model, often described as a white-box model. Such a model is feasible in an SG-dominated system because SGs are largely standardised and have common models, such as the widely used linear magnetic circuit model [31]. Importantly, the controllers of SGs, such as exciters and power system stabilizers (PSS), also exist as commonly-used standard types [32, 33].

Unlike SG, the dynamic behaviour of IBRs is highly dependent on the internal control system which is extremely flexible and far from standardised. Manufacturers treat their control algorithms as critical proprietary technology and when, asked to disclose models to system operators (SOs) for stability prediction, they prefer to disclose only a black-box model which obscures details of internal working. The black-box models provided by manufactures are usually in complied binary library files such as '.lib' and '.dll' files that can be incorporated in standard time-step simulators of power system of the electro-magnetic transient (EMT) or root-mean-square (RMS) form. In this format, the control algorithms can be invoked by a numerical solver and are then used for time-domain simulation [34–36]. Such models can represent dynamics, nonlinear dynamics, with high fidelity, hence offering explicit and convincing results for stability validation. However, the EMT simulation is very time-consuming, especially for large scale power systems and when exhaustive studies of many operating point variations are needed, while the RMS simulation only considers the fundamental frequency values. In addition, the underlying stability risks sometimes cannot be observed from time-domain simulation.

Considering the challenges described in this section, a less time-consuming but more interpretive black-box model is desired for SOs to assess the stability of power systems with high penetrations of IBRs.

1.2 Impedance Models in Three-Phase AC systems

Due to the restriction of binary library files as a model of IBR, research attention has fallen on an alternative black-box model: the impedance model, or equivalently the admittance model [37–40]. Such

models are frequency-domain models representing linearised small-signal dynamics via frequency spectra or transfer functions.

1.2.1 Illustration of Impedance Model

Impedance, or admittance, expresses the frequency-dependent relationship between voltage and current at the output ports of a device or a system. Typically, the symbol $Z(s)$ is employed to represent an impedance, where s is a complex number frequency parameter $s = \sigma \pm j\omega$, with real numbers σ and ω . Similarly, the symbol $Y(s)$ is usually used to represent admittance. An impedance given in transfer function format is usually expressed as a polynomial such as

$$Z(s) = \frac{a_n s^n + a_{n-1} s^{n-1} + \cdots + a_1 s + a_0}{b_m s^m + b_{m-1} s^{m-1} + \cdots + b_1 s + b_0}. \quad (1.1)$$

For physical systems, $\{a_0, a_1, \cdots, a_m\}$ and $\{b_0, b_1, \cdots, b_n\}$ are all real numbers. Alternatively, an impedance can be written in a pole-zero form as

$$Z(s) = \frac{(s - z_n)(s - z_{n-1}) \cdots (s - z_1)}{(s - p_m)(s - p_{m-1}) \cdots (s - p_1)}, \quad (1.2)$$

where $\{p_1, p_2, \cdots, p_m\}$ are the poles of the system while $\{z_1, z_2, \cdots, z_n\}$ are the zeros. The location of the poles and zeros in the complex plane can provide qualitative insights into the response characteristics of a system. It is worth mentioning that for physical systems, zeros and poles are either real-valued numbers or conjugate pairs of complex numbers. For a proper system, the number of zeros cannot exceed the number of poles. Another representation is the pole-residue form as

$$Z(s) = \frac{r_m}{s - p_m} + \frac{r_{m-1}}{s - p_{m-1}} + \cdots + \frac{r_1}{s - p_1}, \quad (1.3)$$

where $\{r_1, r_2, \cdots, r_m\}$ refer to the residues in line with the poles, which are either real numbers or conjugate pairs of complex numbers, depending on the corresponding poles $\{p_1, p_2, \cdots, p_m\}$.

In addition to transfer functions, impedance can also be represented by a frequency spectrum, expressed as $Z(j\omega)$, and depicted in Bode plots. Bode plots are helpful for stability analysis and control

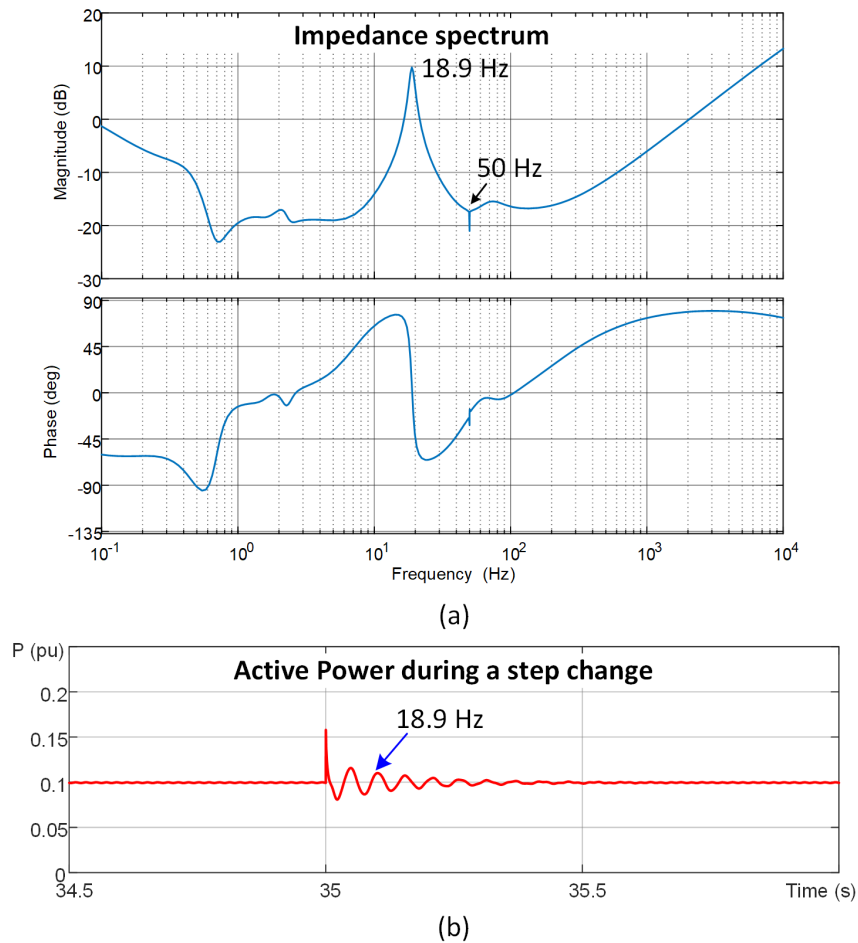


Figure 1.2: (a) An impedance spectrum, in Bode plot form, measured at one node of a modified IEEE 14-bus network. (b) Step-response of active power at that node, showing that a 18.9 Hz oscillation can be observed which matches the peak observed in the Bode plot.

design in that they allow assessment of phase margin [41, 42]. A frequency spectrum also offers a straightforward way of identifying poorly damped modes in a system because these modes typically appear as 'peaks' in Bode plots, and the smaller the damping of the mode, the more significant the peak will be [43]. Fig. 1.2(a) shows the impedance spectrum measured at one node of a modified IEEE 14-bus network, where a significant peak is visible at 18.9 Hz. This indicates that the system contains a 18.9 Hz oscillatory mode. Fig. 1.2(b) shows a time-domain simulation of the active power at that node during a step change of the load in the system. It is clear that a 18.9 Hz oscillation is generated during the transient period, which confirms the presence of the mode seen in the spectrum.

In general, impedance models offer some interpretability in the sense of poles and zeros in transfer functions, as well as resonance peaks in the spectrum.

1.2.2 Impedance Model of an IBR

We first describe an impedance model of an IBR in a single-phase system. A single-phase IBR can be treated as a single-port system, as shown in Fig. 1.3(a). A single-port system can be represented in two ways. An IBR working as a voltage source, such as grid-forming inverter, can be represented in a Thévenin equivalent circuit in which its output impedance $Z_S(s)$ is in series with an internal voltage source V_S [37, 44, 45], as shown in Fig. 1.3(b). This impedance $Z_S(s)$ describes the way in which the output voltage changes for changes in output current. And because an impedance model is essentially a linearised small-signal model, the definition of impedance needs to be established in small-signal scope, i.e., a small-signal perturbation is introduced around an equilibrium value. In the Thévenin equivalent circuit in Fig. 1.3(b), a small-signal perturbation \tilde{i} on the output current is introduced, while the internal source V_S is unperturbed and treated as 0 for small-signal analysis. In such a condition, the small-signal output voltage Δv at the port is

$$\Delta v = Z_S(s) \cdot \tilde{i}, \quad (1.4)$$

where $Z_S(s)$ is defined as the impedance model of this IBR since it describes the relationship between the small-signal voltage and small-signal current at the port. In the alternative case for an IBR behav-

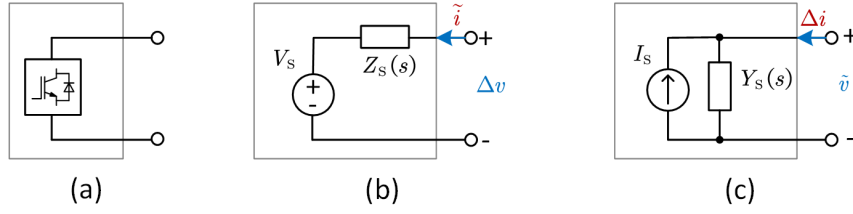


Figure 1.3: Small-signal impedance model of a single-phase IBR: (a) single-port illustration. (b) Thévenin equivalent circuit defining the impedance model. (c) Norton equivalent circuit defining the admittance model.

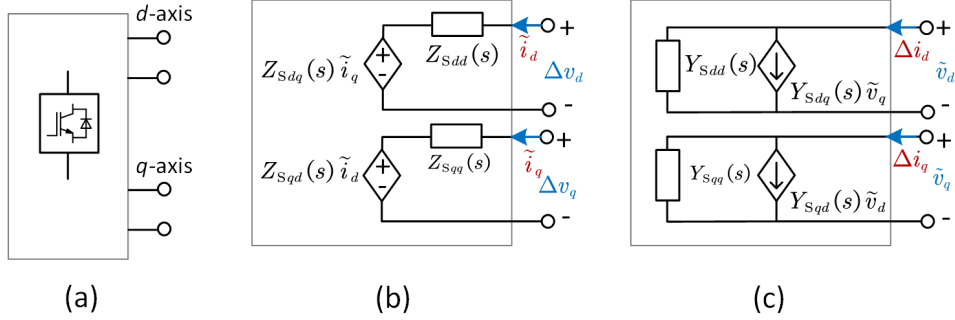


Figure 1.4: Small-signal impedance model of a three-phase IBR in d - q frame: (a) two-port illustration. (b) IBR impedance model in d - q frame. (c) IBR admittance model in d - q frame.

ing as current source, such as grid-following inverter, a Norton equivalent circuit can be used where the output admittance $Y_S(s)$ is in parallel with a current source I_S [46–48], as shown in Fig. 1.3(c). Similarly, when introducing a small-signal voltage \tilde{v} at the output port, the resulting small-signal current will be

$$\Delta i = Y_S(s) \cdot \tilde{v}, \quad (1.5)$$

where $Y_S(s)$ is defined as the admittance model of this IBR.

Now we extend the IBR impedance models to three-phase AC systems. Because the system is three-phase, a frame transformation is usually applied in which the stationary frame is transformed to the synchronously rotating d - q frame, such that the three-phase ac system becomes two coupled dc systems [49]. The IBR is then seen as a two-port system in the d - q frame, as shown in Fig. 1.4(a). Fig. 1.4(b) shows the formulation of the IBR impedance model, where two Thévenin equivalent circuits are employed. In addition to the impedance, each circuit contains a small-signal current-controlled voltage source (effectively a trans-impedance) that represents the coupling between the d -axis and the q -axis. The steady, unperturbed, internal voltage sources are omitted. In contrast to

the single-phase example, the small-signal variations in d - q frame are vectors of dimension 2 and the impedance element in Fig. 1.3(b) is replaced by a 2×2 matrix in d - q frame [50], such that:

$$\begin{bmatrix} \Delta v_d \\ \Delta v_q \end{bmatrix} = \begin{bmatrix} Z_{Sdd}(s) & Z_{Sdq}(s) \\ Z_{Sqd}(s) & Z_{Sqq}(s) \end{bmatrix} \cdot \begin{bmatrix} \tilde{i}_d \\ \tilde{i}_q \end{bmatrix}, \quad (1.6)$$

where, the impedance model of an IBR in d - q frame is defined as

$$Z_S(s) = \begin{bmatrix} Z_{Sdd}(s) & Z_{Sdq}(s) \\ Z_{Sqd}(s) & Z_{Sqq}(s) \end{bmatrix}. \quad (1.7)$$

Similarly, Fig. 1.4(c) demonstrates the IBR admittance model in d - q frame, where two Norton equivalent circuits are employed and two controlled current sources are presented. The unperturbed internal current sources are omitted. The relationship between the small-signal voltage input and current output is

$$\begin{bmatrix} \Delta i_d \\ \Delta i_q \end{bmatrix} = \begin{bmatrix} Y_{Sdd}(s) & Y_{Sdq}(s) \\ Y_{Sqd}(s) & Y_{Sqq}(s) \end{bmatrix} \cdot \begin{bmatrix} \tilde{v}_d \\ \tilde{v}_q \end{bmatrix}. \quad (1.8)$$

The admittance model of an IBR $Y_S(s)$ in d - q frame is then defined as

$$Y_S(s) = \begin{bmatrix} Y_{Sdd}(s) & Y_{Sdq}(s) \\ Y_{Sqd}(s) & Y_{Sqq}(s) \end{bmatrix}. \quad (1.9)$$

The characteristics of the impedance of an IBR is basically shaped by its hardware (resistance, inductance and capacitance) and software (control loop parameters). There are many approaches to acquiring impedance model expressions of IBRs. A common approach is to use an analytical method, such as traditional linearisation [50, 51], harmonic linearisation [39, 52], or through equivalent circuit manipulation (known as an impedance circuit model) [53]. Such methods use parameter values of the IBR to calculate the transfer function of the impedance model. Taking an impedance (rather than admittance) circuit model as an example, using the principles of equivalent-circuit formation (applications of Ohm's Law, Superposition Theorem, Thévenin's or Norton's equivalent circuits), the control loops of an inverter can be visualised as discrete circuit elements in an impedance circuit, with

values calculated from the control parameters. Fig. 1.5(a) illustrates the typical control arrangement of a grid-forming inverter, where explanations of the parameters can be found in appendix D.2. By applying the impedance circuit model analysis, the equivalent circuit of Fig. 1.5(b) can be created in which the controllers, virtual impedances, cross-coupling and decoupling effects, and feed-forward of output-current and output-voltage can all be represented by a collection of impedance elements shown with dashed lines to distinguish them from physical impedances. The impedances have been colour-coded to identify them with specific control elements. The calculation of each impedance elements and the additional effect of the droop controller can be found in [53].

The analytical method is limited in applicability to cases where full knowledge of the design of the IBR is available, thus its use is dependent on the cooperation of vendors and is not fully available to the SO by default. Besides this, an impedance model is essentially a small-signal model established upon steady state and so the model would vary according to the operating point of the system and the operating point of a power systems is expected to vary widely. The relationship between an impedance model and the operating point is yet not fully understood. Furthermore, because of the difference between analytical equations based on simplifying assumptions and detailed hardware implementations, the analytical impedance models cannot completely describe the behavior of a real IBR. An alternative approach to acquire impedance models is the measurement-based method which opens promising opportunities for impedance models [54,55]. A measurement-based model is found from a set of real rather than notional voltage or current perturbations applied to an IBR at a range of frequencies and the corresponding measured responses. Fig. 1.6 [56] shows the positive-sequence impedance spectra of a 2 MVA BESS inverter measured by National Renewable Energy Laboratory (NREL) when the BESS inverter was operated in grid-following and grid-forming control modes. This demonstrates measurement-based impedance spectra can be obtained on power system apparatus without knowing any design details and can thus help either vendors to assess their own modelling or help SOs to acquire independent models.

From a measured spectrum, a corresponding transfer function can be obtained using the vector fitting technique [57]. Impedance measurement can be fulfilled online [58,59] and thus can be used as a data-driven approach for stability assessment [60]. A very recent research work [61] combines an artificial neural network method with the impedance measurement method to identify the model under various

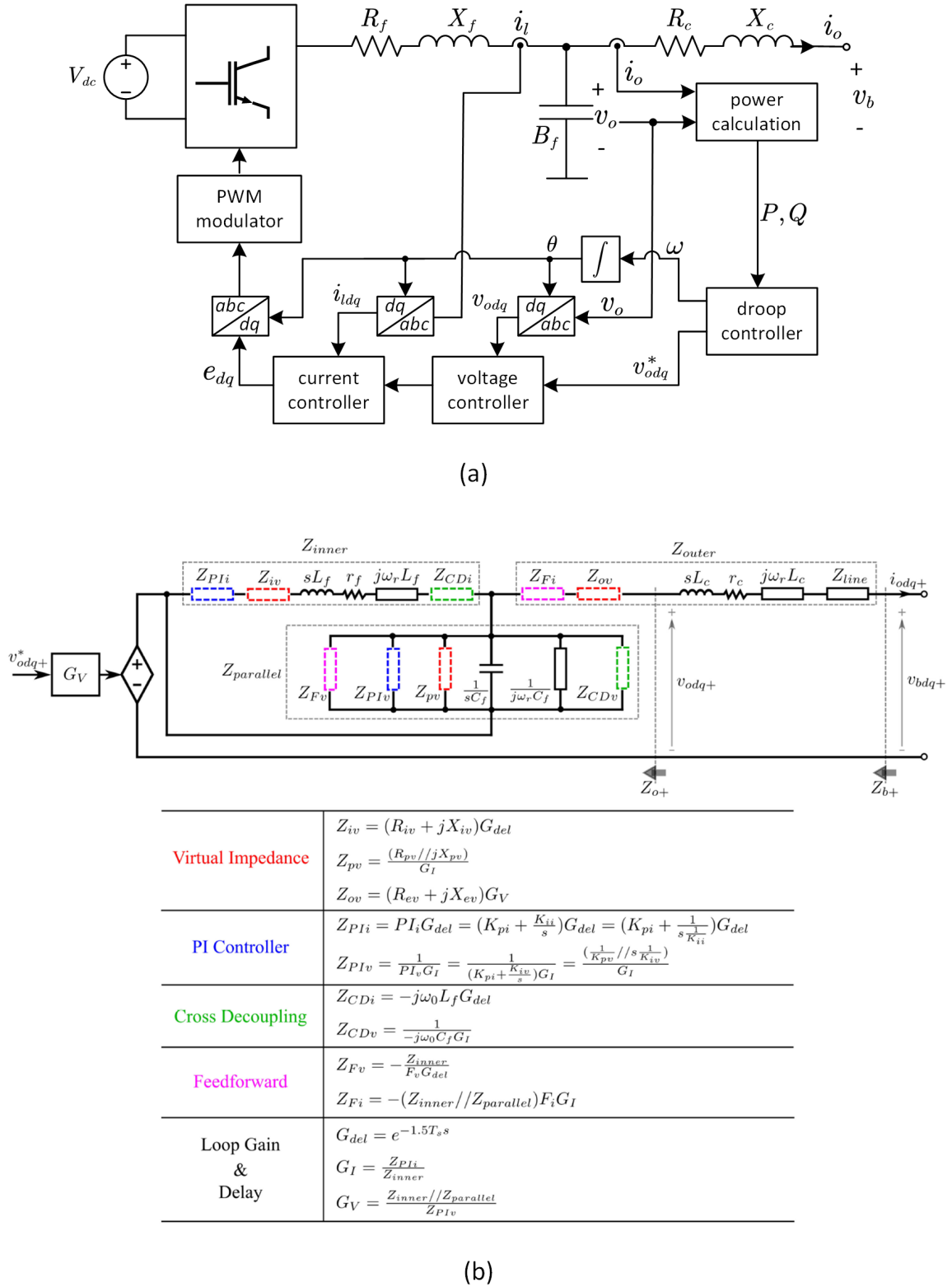


Figure 1.5: (a) Illustration of the design of a droop-controlled grid-forming inverter. (b) Impedance circuit model of the grid-forming inverter [53]. Copyright © 2021, IEEE..

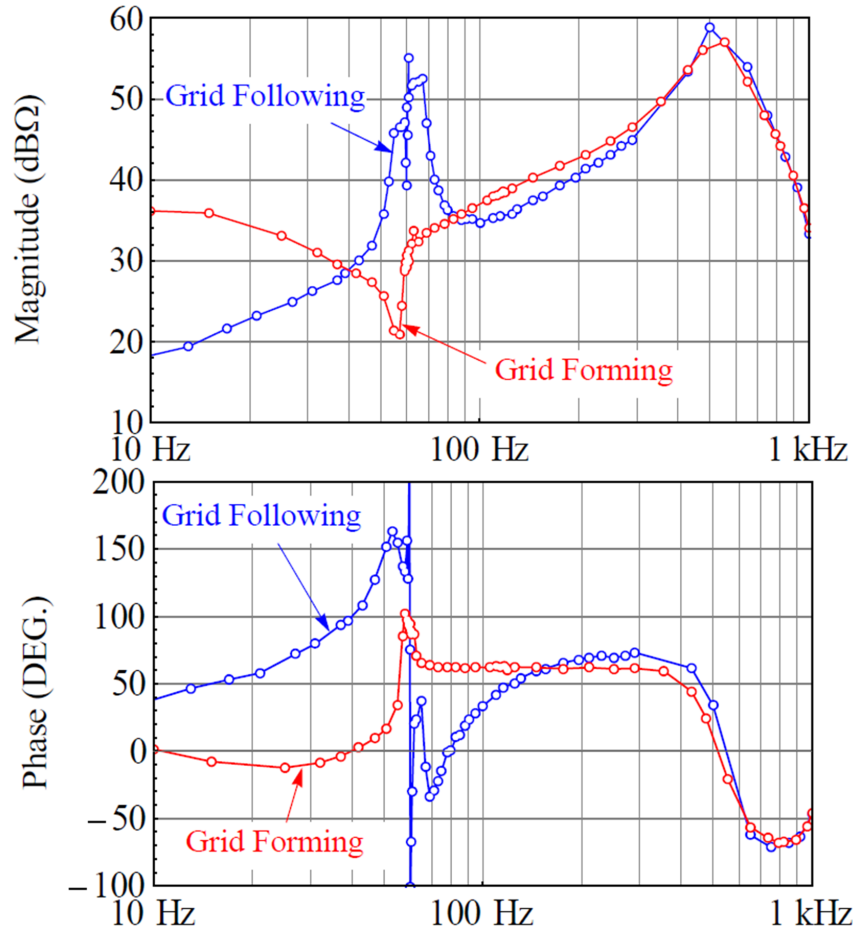


Figure 1.6: Positive-sequence impedance spectra of a 2 MVA BESS inverter measured by National Renewable Energy Laboratory (NREL) when it is operated in grid-following and grid-forming control modes [56]. Copyright © 2019, IEEE.

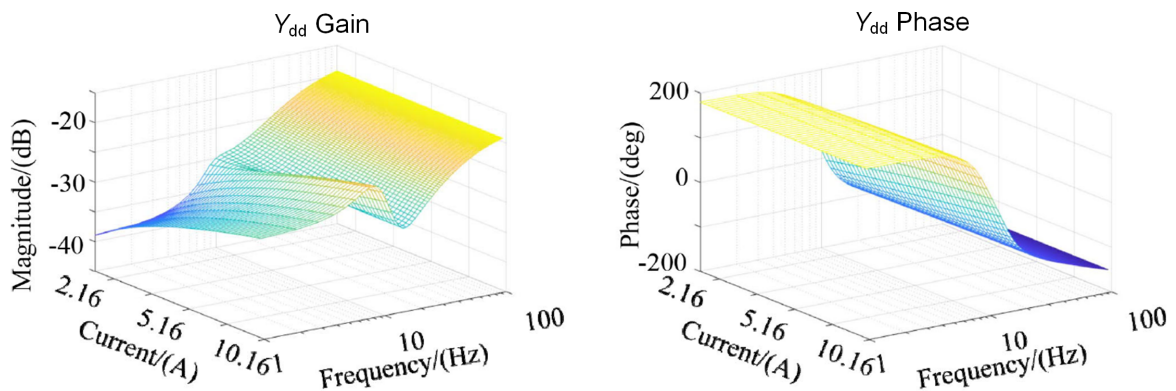


Figure 1.7: d - d axis admittance spectrum of a grid-following inverter at different operating points, showing that the spectrum varies along with the change of operating points [61]. Copyright © 2020, IEEE.

operating points which is said to offer more reliable results in varying conditions. Fig. 1.7 [61] shows the admittance spectrum of a grid-following inverter equipped with phase-locked loop (PLL) working at different operating points. It can be noticed that the admittance spectrum of an inverter can vary according to the changes of its output current. This means that a single spectrum at one operating point is sometimes not sufficient to describe all the dynamic characteristics of the inverter, and online measurement is needed to cover different situations. Still, as a matter of fact, measurement error caused by noise is not yet fully analysed, so the choice of perturbation amplitude to apply rests on the experience of researchers rather than analysis. Impedance measurement techniques and related issues will be discussed in detailed in Chapter 5.1.

1.2.3 Impedance Models for Nyquist-based Stability Assessment

The use of impedance models has been popular in the power electronic field used mainly to analyse the interactions between a power electronic converter (source) and a load connected at the output of the converter [62–64]. Considering a case where a voltage source converter $V_S(s)$ with internal impedance $Z_S(s)$ is connected with a load with admittance of $Y_L(s)$, the load current $I_L(s)$ can be derived as

$$I_L(s) = V_S(s) \frac{Y_L(s)}{1 + Z_S(s) Y_L(s)}. \quad (1.10)$$

The load voltage can then be acquired:

$$V_L(s) = \frac{I_L(s)}{Y_L(s)} = V_S(s) \frac{1}{1 + Z_S(s) Y_L(s)}. \quad (1.11)$$

In such way, the relationship between input voltage $V_S(s)$ and output voltage $V_L(s)$ can be written as a closed-loop transfer function as $1/(1 + Z_S(s) Y_L(s))$ and the corresponding loop transfer function is $Z_S(s) Y_L(s)$. The Nyquist criterion can then be applied: the system will be closed-loop stable if and only if the number of counter-clockwise encirclements about $(-1, 0j)$ by the Nyquist plot of $Z_S(s) Y_L(s)$ be equal to the number of right half plane (RHP) poles of $Z_S(s) Y_L(s)$. This stability assessment method was widely applied to low-voltage DC distribution networks [65–67], but has been extended to 3-phase AC systems in the d - q frame to predict the stability at the point of common

coupling (PCC) [45,49,68–71]. The extension of the impedance method to 3-phase AC systems opens up a path to using impedance representation as an analytical tool for power systems.

To apply the Nyquist Criterion in a power system, the system first needs to be separated into two parts: a source-side part and a load-side part. Fig. 1.8(a) shows the single-line diagram of such a bi-partition, where an IBR is presented as the source and a load is connected at the other side. An IBR working as a voltage source, such as grid-forming inverter, can be represented in a Thévenin equivalent circuit in which its output impedance $Z_S(s)$ is in series with a voltage source $V_S(s)$, and the load is represented as an admittance $Y_L(s)$, as shown in Fig. 1.8(b). In the alternative case of an IBR behaving like current source, such as grid-following inverter, a Norton equivalent circuit can be applied where output admittance $Y_S(s)$ is in parallel with a current source $I_S(s)$, and the load is represented as an impedance $Z_L(s)$, as shown in Fig. 1.8(c). Taking a Thévenin equivalent circuit as an example:

$$Z_S(s) = \begin{bmatrix} Z_{Sdd}(s) & Z_{Sdq}(s) \\ Z_{Sqd}(s) & Z_{Sqq}(s) \end{bmatrix}, Y_L(s) = \begin{bmatrix} Y_{Ldd}(s) & Y_{Ldq}(s) \\ Y_{Lqd}(s) & Y_{Lqq}(s) \end{bmatrix}, V_S(s) = \begin{bmatrix} V_{Sd}(s) \\ V_{Sq}(s) \end{bmatrix}. \quad (1.12)$$

In such a representation, the voltage at the PCC can be derived as [72]

$$V_{\text{PCC}}(s) = (I + Z_S(s)Y_L(s))^{-1} V_S(s), \quad (1.13)$$

where I is an identity matrix. Since the system is a multi-input and multi-output (MIMO) system in d - q frame, the generalised Nyquist stability criterion (GNC) needs to be employed for stability assessment of the matrix form of the transfer function. From (1.13), the return ratio matrix $L(s)$ can be defined as

$$L(s) = Z_S(s)Y_L(s), \quad (1.14)$$

such that

$$L(s) = \begin{bmatrix} L_{dd}(s) & L_{dq}(s) \\ L_{qd}(s) & L_{qq}(s) \end{bmatrix}. \quad (1.15)$$

Because the system is now extended to MIMO, the term ‘return ratio matrix’ is employed, which is in contrast with ‘loop transfer function’ in a SISO systems. $L(s)$ contains two frequency-dependent

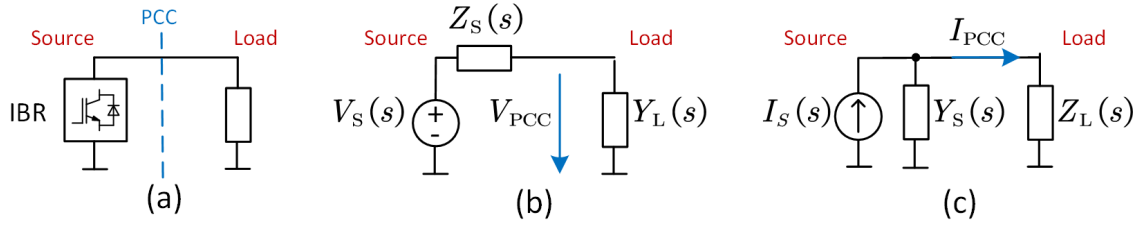


Figure 1.8: Single-line diagram of Nyquist-based formulation of impedance models in power systems: (a) source-side and load-side bi-partition. (b) Thévenin equivalent circuit. (c) Norton equivalent circuit.

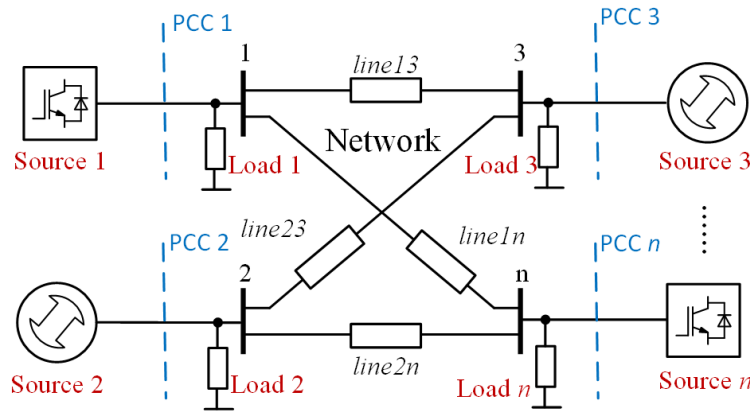


Figure 1.9: Single-line diagram of a meshed network with multiple sources, loads and branches, showing that it is difficult to separate the system into a source-side and a load-side.

eigenvalues: $t_1(s)$ and $t_2(s)$, the traces of which in the complex plane are also called a set of characteristic loci (eigenloci). According to the GNC [73, 74], the system will be closed-loop stable if and only if the net sum of anticlockwise encirclements of the critical point $(-1, 0j)$ by the set of eigenloci of $L(s)$ is equal to the total number of right-half plane poles of $Z_S(s)$ and $Y_L(s)$. Based on the GNC, the stability of the PCC voltage can be assessed.

Although widely studied for stability assessment and progressed in several ways, the GNC-based method remains based on a source-side and load-side bipartition of the grid system. Such separation is straightforward in low-voltage dc system but can be extremely difficult in a meshed AC network [75]. Fig. 1.9 shows a meshed network with multiple sources and loads. It can be seen that it is difficult to re-structure such system into a source-side and a load-side, meaning GNC-based analysis is hard to apply in meshed networks like power systems. This is an important factor obstructing the application of impedance models in power systems.

1.3 Motivations and Objectives of this Thesis

The possibility of using impedance models in power system stability analysis has prompted a wide range of research works. However, there are several crucial issues remain unsolved, which limits the application of impedance models.

1.3.1 Networked Impedance Models

The basic form of the impedance model as a single impedance spectrum observed at one bus means that it can not represent the full dynamics of an entire power system comprising many buses. Alongside that difficulty, it is also hard to divide a power system into a source-side and a load-side and without that the GNC-based analysis cannot be applied. As an alternative, recent research has turned to impedance models which can represent the whole network, referred as networked impedance models [47, 76–79]. Individual impedance models are first aligned to a global frame [76] then assembled together to form an impedance matrix in the global $d-q$ frame. There are essentially two categories of networked impedance models referred to here as the nodal-loop models [77–79] and whole-system models [47, 76]. Such models are transfer functions or frequency spectra assembled in matrix form, such that each entry in the matrix is a transfer function or a frequency spectrum expressed in a global synchronous frame. These models will be described in detail in Chapter 2 but for now we note that the nodal-loop model category is further categorised into nodal admittance models Y^{nodal} and loop impedance models Z^{loop} , and the whole-system model category is further categorised into whole-system impedance models Z^{sys} and whole-system admittance models Y^{sys} .

The four types of networked impedance models are defined via different methods. For Y^{nodal} and Z^{loop} , they are defined in a similar fashion as the conventional nodal admittance matrix and loop impedance matrix used in power flow calculation. The Z^{sys} and Y^{sys} types are developed from a closed-loop formation in which each entry contains the dynamics of the whole-system. Although all these models carry common information, i.e., the full dynamics of the system, the inherent relations between them, as well as their unique characteristics and relative merits have not yet been established by previous research. In order to select a suitable model for system analysis from among these mod-

els types, the relationship between nodal-loop model and whole-system model and their underlying association with oscillatory modes should be compared and clarified, so that their relative merits can be established.

For stability analysis of a power system through a networked impedance model, it is important to create a comprehensive view of the entire system not just a view at a single PCC. In state-space models, eigenvalue analysis has been well established as a means to view all system dynamics [19, 24, 25]. The eigenvalues of the state-space matrix have explicit physical meaning in that conjugate complex pairs of eigenvalues represent oscillatory modes of the system. For an eigenvalue of the state-space model $\lambda = \sigma \pm j\omega$, the term $\omega/(2\pi)$ gives the frequency of oscillation in Hz and $1/|\sigma|$ gives the time-constant of the decay of oscillation amplitude. To perform similar analysis in impedance models, the association between impedance models and state-space models needs to be built. It has been observed that the zeros of the determinant of nodal-loop models are equal to state-space eigenvalues [79–81] and the poles common to all elements of a whole-system model are equal the state-space eigenvalues [76]. However, such findings have not yet created a comprehensive and clear explanation of all of the relationships .

1.3.2 Modal Analysis in Impedance Models

A networked impedance model is created in a matrix form in a similar way to a state-space matrix, and appears to have a relationships to state-space. This suggests that seeking further modal analysis of impedance models such as identifying participation factors and eigenvalue sensitivities might be possible. Researchers around the world have made progress on using impedance models for stability analysis [77, 78, 82–92]. So far, two major approaches to impedance-based modal analysis have been proposed: the resonance mode analysis (RMA) method [77, 78, 82–89], and the Nyquist-based participation analysis [90–92]. These two methods are reviewed in detail in Chapter 3. However, the available methods of eigenvalue sensitivity and participation factor assessment for impedance models are less precise and clear than their equivalents in state-space models, for instance being restricted to comparing the magnitude of complex quantities with no meaning attached to the angles, or forming judgements by visual inspection. These indications are useful to an extent but leave the

engineer needing to tune parameters according to judgement and experience. There is no standard and unambiguous procedure for sensitivity and participation analysis, i.e., a whole procedure that can determine the major participants of modes, identify the badly-tuned components, indicated the most effective parameters for tuning inside these components, and eventually offer precise tuning guidance for these parameters.

1.3.3 Errors of Impedance Measurement

Online impedance measurement is a potentially important way of obtaining a black-box impedance model, and a bridge to connect the analytical method with practical implementations. Efforts have been made to develop perturbation injection equipment and suitable waveforms for small-signal injections and these will be introduced in detail in Chapter 5. However, as a measurement process, the identification of an impedance spectrum involves errors which may severely affect the final results.

Two important issues related to measurement errors remain unsolved. The first issue is the choice of signal amplitude and signal to noise ratio (SNR). Background noise and harmonics are known to exist in the signal channel and can strongly affect measurement results and lead to low accuracy. On the one hand, the amplitude of injected signal could set as large as possible for higher SNR, while on the other hand, the amplitude should be as small as possible to minimise its influence on the operation of the system and its stability. The existence of this conflict has been noted by researchers but has usually been solved by a trade-off based on experience or numerous trial-and-error attempts. For example, [59] considers 5% of AC voltage and 10% of AC current as a proper range for small-signal perturbation without discussing the reason behind this. [93] states that signal with 1% to 5% of nominal power is required for satisfactory results based on experience at the author's institution. In [56], a set of measurements under perturbations of 0.5%, 5% and 10% of the steady-state value were performed, showing that the measurement results can be affected by noise if the injections are too small, but a suitable amplitude was not discussed. Researchers have noticed the importance of noise analysis and tried to assess the value of SNR [94], but the value is only provided for adding context and aiding intuitive sense rather than being used to determine the injected amplitude.

The second issue is the validation of measurement results. So far it is not clear how to estimate the error present in an impedance measurement taken from an experiment because of the absence of reference, or true, value. Most research work presents experimental results as Bode plots together with a ‘reference’ plot derived from analytical or simulation results. By observing the dispersion of measurement points on the Bode plot, a rough impression of measurement error can be obtained. However, as is commonly acknowledged, hardware devices will not be strictly the same as their analytical representation because of the presence of nonlinear behaviors such as dead time and therefore the plot derived from a linearised model or simulation cannot be considered as the true value for the hardware. Besides this, the impedance measurement results are originally complex numbers, while Bode plot is acquired from the argument of the complex numbers. Because the gain-plot and phase-plot in a Bode plot involve errors in different units, it is difficult to compare the errors among different plots.

1.3.4 Objectives of this Thesis

This objectives of this thesis can be concluded as below:

- 1) To clarify the association between impedance models and the state-space model, and to establish the relationship among different types of networked impedance models so that the appropriate model can be chosen for analysis.
- 2) To propose a comprehensive theory for root-cause analysis in impedance models, together with a standard and unambiguous procedure for sensitivity and participation analysis, i.e., a whole procedure that can determine the major participants of modes, the badly-tuned components, the most effective parameters inside these components, and eventually offer precise tuning guidance on these parameters.
- 3) To propose a method which can determine the minimum injection amplitude for impedance measurement based on an allowable error. Alongside this, a method is needed to determine what the true value of the impedance of a physical system is so that measures can be judged for accuracy, and indeed, a metric for measurement error needs to be established so that measurement results can be compared with each other. These are considered as objectives of the

measurement portion of the thesis.

These objectives are achieved in the following chapters of this thesis, and the outcomes have been published as two research papers [95, 96].

1.4 Thesis Structure

The main content of the thesis is organised as follows:

Chapter 2 introduces and compares the two categories of networked impedance models and establishes their relative merits. The association between impedance models and the state-space model is also discussed.

Chapter 3 reveals the drawbacks of existing impedance-based modal analysis methods and proposes a comprehensive theory of root-cause analysis in networked impedance models, including eigenvalue sensitivity and participation factor. A three-layer grey-box approach is then invented as a systematic way to facilitate root-cause tracing to different depths.

Chapter 4 verifies the root-cause theory and the grey-box approach through case studies of various scales: a three-node passive network, a modified IEEE 14-bus network and a modified NETS-NYPS 68-bus network.

Chapter 5 investigates the issues identified in impedance measurement and develops a full process for noise analysis which can be the basis of choosing the injection amplitude and of validating measurement results. Hardware experiments are undertaken to verify the process.

Chapter 6 sets out the conclusions of the work, identifies the contributions of this thesis and discusses suggestions for future work.

Chapter 2

Networked Impedance Models and Comparative Study

This chapter will describe the two categories of networked impedance models mentioned in the introduction, namely the nodal-loop models and the whole system models. The relationships between the two categories will be explored as will their relationship to state-space modelling. A comparative study is carried out which offers guidance on how to choose a suitable model for different situations. The main content of this chapter has been published as part of [96] and some sentences and figures from that paper are reused here.

To recap some of the remarks from the introduction, a single impedance spectrum or transfer function observed at one node in a network through load-source separation is insufficient to cover all dynamic characteristics of the system and for that reason networked impedance models have been developed. The impedances of all apparatus, as well as connecting lines, are included in the networked impedance models so that they contain all of the dynamics of the systems. Here the term 'apparatus' is used to refer to IBRs, synchronous generators and also active loads in the system. There are essentially two categories of networked impedance model: the nodal-loop model which is further categorised into Y^{nodal} and Z^{loop} , and the whole-system model which is further categorised into Z^{sys} and Y^{sys} . It is also worth noting that the impedance of each apparatus is established in its local rotating frame, so that frame alignment among all impedances is needed before assembling them together.

2.1 Frame Alignment

Apparatus in three-phase AC systems are normally modeled in a rotating reference frame aligned to the local angle, such as the angle of the physical rotor of a machine or the angle identified by a PLL of an inverter. To assemble together the models of apparatus at different nodes, these locally referenced models need to be aligned to a global frame. The alignment is straightforward in a state-space model because the angle difference between a local frame (node- k) and the selected global frame (node-1) is available directly from the difference in local frequencies which will be states of the state-space model:

$$\dot{\delta}_k = \omega_k - \omega_1, \quad (2.1)$$

where ω_k is the local frame speed and ω_1 is the global frame speed.

In contrast, frame alignment is not straightforward in impedance models because impedance models only express relationships between voltage and current and contain no explicit information on frame angles. It has been reported that errors can be introduced if impedance models at different nodes are assembled together without frame alignment [47], and a set of results illustrating this are shown in Fig. 2.1. It can be clearly seen that the impedance with frame alignment is consistent with the frequency-scan results carried in simulations, while results without alignment can lead to significant errors. The alignment in [47] rests on an assumption that the local phase angles are constant values. This is appropriate for systems with high inertia because the frame dynamics (i.e., rotor swing and frequency perturbation) in such systems are well separated in frequency from the small-signal stability issues because they are of very low-frequency. However, for systems with high penetration of IBRs and low inertia, the local frame dynamics introduced by PLLs cannot be neglected [76].

To solve this issue, a two-step alignment method has been proposed in [76] and is briefly introduced here. Fig. 2.2(a) illustrates the frame alignment process, where impedance models that are built under their own local swing frames, are first aligned to a local steady frame, then aligned from local steady frames to the global steady frame. The local swing frame is the frame in which local impedance models are established, aligned to either a rotor angle or a PLL angle. The local steady frame is defined as a frame aligned to the local steady-state operating point, with a constant speed ω_0 . Based

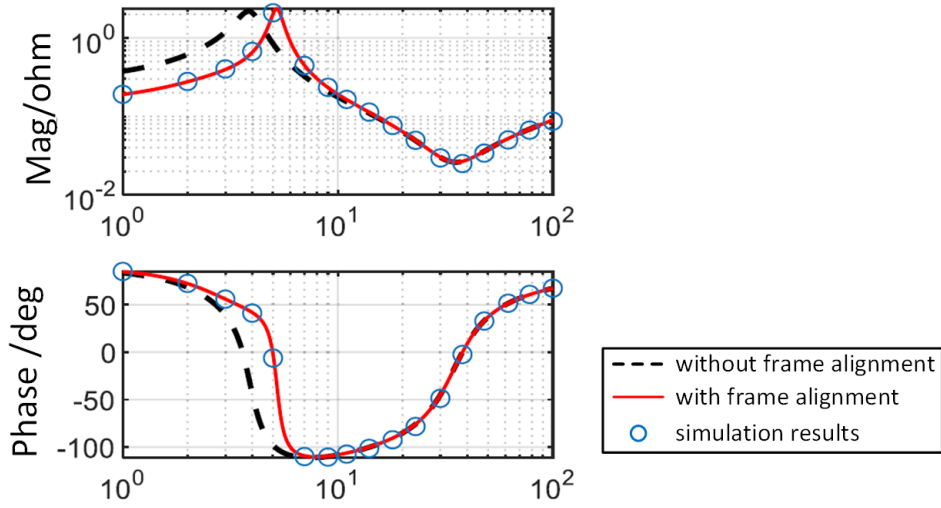


Figure 2.1: The spectrum of impedance at the PCC of a simple interconnected ac power electronics system, showing that the model does not match with simulation results if the frames are not aligned [47]. Copyright © 2020, IEEE.

on such separation, the local-to-global frame transformation can be fulfilled in two steps: (i) from a local swing frame to a local steady frame, i.e., from dynamic to constant, and (ii) from a local steady frame to the global frame, i.e., from constant to constant.

The second step is simple because the transformation is from one steady frame to another steady frame which contains no dynamics and is therefore a fixed angle rotation. By obtaining the angle ξ_k of node- k from power flow analysis, the transformation can be directly derived as

$$Z_{k(D'Q')} = T_{\xi_k} \cdot Z_{k(d'q')} \cdot T_{\xi_k}^{-1}, \quad T_{\xi_k} = \begin{bmatrix} \cos \xi_k & -\sin \xi_k \\ \sin \xi_k & \cos \xi_k \end{bmatrix}, \quad (2.2)$$

where $Z_{k(D'Q')}$ is the impedance model at node- k aligned to the global steady frame, $Z_{k(d'q')}$ is the impedance at the local steady frame, and T_{ξ_k} is the transfer matrix.

The first step, in which a local swing frame is transformed into a local steady frame has been named frame-dynamics-embedding impedance transformation. From a local swing frame to a local steady frame, the voltage transformation is

$$u_{k(d'q')} = T_{\varepsilon_k} \cdot u_{k(dq)}, \quad T_{\varepsilon_k} = \begin{bmatrix} \cos \varepsilon_k & -\sin \varepsilon_k \\ \sin \varepsilon_k & \cos \varepsilon_k \end{bmatrix} \quad (2.3)$$

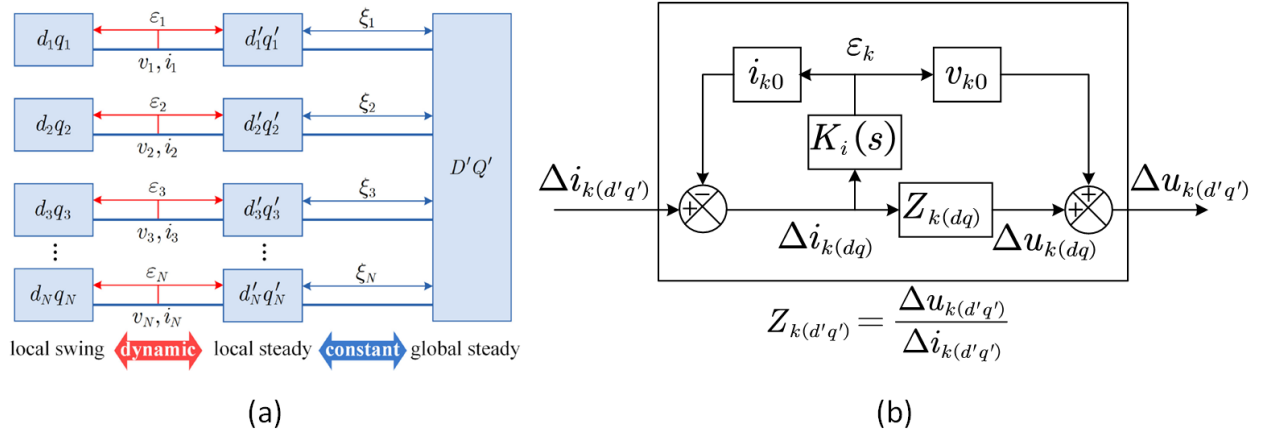


Figure 2.2: (a) Frame alignment in impedance modeling: a local swing frame is first aligned to a local steady frame, with dynamics introduced via dynamic angle ε_k , local steady frame is then aligned to the global steady frame. ε and ξ are angle differences between frames. (b) Signal flow diagram of frame-dynamics-embedding impedance transformation, showing how a local swing frame is transformed into a local steady frame [76]. Copyright © 2021, IEEE.

where $u_{k(d'q')}$ and $u_{k(dq)}$ denote the voltage in steady frame and in swing frame, ε_k is the dynamic angle by which the k -th local swing frame axes leads the k -th steady frame axes. The idea of frame-dynamics-embedding impedance transformation is to perform linearisation on (2.3) to see the effect of frame perturbation, such that

$$\Delta u_{k(d'q')} = \Delta u_{k(dq)} + u_{k0} \cdot \varepsilon, \quad (2.4)$$

in which

$$\Delta u_{k(d'q')} = \begin{bmatrix} \Delta u_{k(d')} \\ \Delta u_{k(q')} \end{bmatrix}, \Delta u_{k(dq)} = \begin{bmatrix} \Delta u_{k(d)} \\ \Delta u_{k(q)} \end{bmatrix}, u_{k0} = \begin{bmatrix} -u_{k0(q)} \\ u_{k0(d)} \end{bmatrix},$$

$u_{k0(d)}$ and $u_{k0(q)}$ are voltages at the steady-state condition in the d - q frame. (2.4) applies the fact that $\varepsilon = 0$ when there is no perturbations, and $\lim_{\varepsilon \rightarrow 0} (\sin \varepsilon) = \varepsilon$. In a case where a frame perturbation ε is introduced by a current perturbation, i.e., Δi_{dq} , the corresponding frame variation will be

$$\varepsilon(s) = K_i(s) \Delta i_{dq}(s), \quad (2.5)$$

where $K_i(s)$ is the transfer function representing the current governed frame dynamics. Combining (2.4) and (2.5), it can be concluded that a current disturbance Δi_{dq} can induce a perturbation (or swing) of the local swing frame by ε , which in turn affects the representation of the current and the

voltage in the steady frame. With such relationship, the signal flow of the frame-dynamics-embedding impedance transformation can be concluded as Fig. 2.2(b), and the impedance in local steady frame can be deduced as

$$Z_{k(d'q')} = \frac{\Delta u_{k(d'q')}}{\Delta i_{k(d'q')}} = (Z_{k(dq)} + u_{k0}K_i) (I + i_{k0}K_i)^{-1}, \quad (2.6)$$

where I is a identity matrix, u_{k0} and i_{k0} are voltage and current in steady-state point:

$$u_{k0} = \begin{bmatrix} -u_{k0(q)} \\ u_{k0(d)} \end{bmatrix}, i_{k0} = \begin{bmatrix} -i_{k0(q)} \\ i_{k0(d)} \end{bmatrix}.$$

The frame alignment of admittance models is conducted in a similar fashion and is explained in [76], where examples are also provided to show the ways of acquiring the term $K_i(s)$.

This frame-alignment method is applied in the case studies of this thesis. For the sake of brevity, all impedance models discussed in the remainder of this thesis have been aligned to the global d - q frame so that they can be assembled together.

2.2 Formulation

2.2.1 Nodal-loop Model

Nodal-loop model is defined in the similar manner to the well-known nodal admittance matrix Y_N and loop impedance matrix Z_L used for power flow calculation. A set of circuit equations can be established from nodal or loop circuit analysis of a network, and assembled into a transfer-function matrix to form a nodal-loop model. There are two formats: a nodal admittance model Y^{nodal} and a loop impedance model Z^{loop} . Here we form Y^{nodal} as an example.

The nodal admittance matrix familiar from power flow studies, Y_N , is a matrix that expresses the admittances of the network lines connected at each node of a network. It is a matrix composed of single-value quantities evaluated at the fundamental frequency of the grid. To extend the scope to

frequency domain analysis, Y_N is first reformed as a matrix of admittances as functions of frequency (transfer functions) as

$$Y_N = \begin{bmatrix} Y_{N11}(s) & Y_{N12}(s) & \cdots & Y_{N1n}(s) \\ Y_{N21}(s) & Y_{N22}(s) & \cdots & Y_{N2n}(s) \\ \vdots & \vdots & \vdots & \vdots \\ Y_{Nn1}(s) & Y_{Nn2}(s) & \cdots & Y_{Nnn}(s) \end{bmatrix}. \quad (2.7)$$

The diagonal entry $Y_{Nkk}(s)$ represents all admittance terminating at node k , whereas the off-diagonal entry $Y_{Nki}(s)$ is the negative of the sum of admittance between node k and node i . Each entry is a 2×2 matrix block in the global synchronous d - q frame, such that

$$Y_{Nki}(s) = - \begin{bmatrix} R_{ki} + sL_{ki} & -\omega_0 L_{ki} \\ \omega_0 L_{ki} & R_{ki} + sL_{ki} \end{bmatrix}^{-1} \quad (2.8)$$

$$Y_{Nkk}(s) = - \sum_{i \neq k} Y_{Nki}(s) + \begin{bmatrix} R_{kk}^{-1} + sC_{kk} & -\omega_0 C_{kk} \\ \omega_0 C_{kk} & R_{kk}^{-1} + sC_{kk} \end{bmatrix},$$

where R_{ki} and L_{ki} are the series-connected resistance and inductances between node k and node i , and R_{kk} and C_{kk} are the shunt-connected resistance and capacitance at node k .

Turning now to the dynamics of apparatus, each apparatus is represented by an admittance model as introduced in Chapter 1.2.2, and these are assembled together into form a diagonal matrix Y_A as

$$Y_A = \begin{bmatrix} Y_{A1}(s) & & & \\ & Y_{A2}(s) & & \\ & & \ddots & \\ & & & Y_{An}(s) \end{bmatrix}, \quad (2.9)$$

where each entry is the admittance of the shunt-connected apparatus (including active loads), and

again a 2×2 matrix block in d - q frame as

$$Y_{Ak}(s) = \begin{bmatrix} Y_{Ak,dd}(s) & Y_{Ak,dq}(s) \\ Y_{Ak,qd}(s) & Y_{Ak,qq}(s) \end{bmatrix}. \quad (2.10)$$

It is also worth noting that this description covers only apparatus that are shunt-connected but series-connected apparatus in branches such as a static series synchronous compensator (SSSC) or the series element of a unified power flow controller (UPFC), could be included by merging them into Y_N .

The formulation of nodal admittance model of the system, Y^{nodal} , proceeds by connecting the admittance of apparatus Y_A with the admittance of the network Y_N , through a process which can be understood from considering a virtual injection. Fig. 2.3(a) shows a network of n nodes represented by Y_N with individual apparatus admittances at each node. At each node there is also a voltage perturbation \tilde{v} applied which creates corresponding changes in nodal currents Δi which flow in the parallel combination of the apparatus admittance and the nodal admittance. The overall response of the system to a perturbation injection is expressed as

$$\Delta i = Y^{\text{nodal}} \cdot \tilde{v}, \quad (2.11)$$

where

$$\begin{aligned} \tilde{v} &= [\tilde{v}_1, \tilde{v}_2, \dots, \tilde{v}_n]^T \\ \Delta i &= [\Delta i_1, \Delta i_2, \dots, \Delta i_n]^T. \end{aligned} \quad (2.12)$$

Apparently the nodal admittance model is the summation of the nodal admittance matrix Y_N and the apparatus admittance matrix Y_A due to the parallel combination, such that

$$Y^{\text{nodal}} = Y_N + Y_A. \quad (2.13)$$

The fact that both Y_N and Y_A respond directly to the perturbation and combine in a simple manner to form Y^{nodal} is in contrast to other models in which a feedback is formed between two elements of the

model. For this reason the nodal admittance model can also be referred to as an open-loop model [47].

In a similar manner, the loop impedance model Z^{loop} expresses how a vector of current perturbations applied to each loop current of the grid creates a vector of corresponding additional voltage drops around the loop, as shown in Fig. 2.3(b),

$$\Delta v = Z^{\text{loop}} \cdot \tilde{i}, \quad (2.14)$$

where

$$\begin{aligned} \tilde{i} &= [\tilde{i}_1, \tilde{i}_2, \dots, \tilde{i}_n]^T \\ \Delta v &= [\Delta v_1, \Delta v_2, \dots, \Delta v_n]^T. \end{aligned} \quad (2.15)$$

Although the loop impedance model is broadly a dual of the nodal admittance model and might be equally useful, it suffers one significant disadvantage that it can be formulated in a variety of ways for a given grid because there are multiple legitimate ways to define a set of loops covering the network. Without a systematic approach to the choice of loop currents, there is not a single unique loop model for a given network and so ambiguity can exist. Consequently, it is difficult to manipulate this model in further analysis. In the remainder of this thesis, only Y^{nodal} form of the nodal-loop model is discussed. It is also worth noting that the small-signal injections in Fig. 2.3 are only shown for understanding but cannot be fulfilled in real because a small-signal voltage source cannot override the shunt-connected apparatus, neither can a small-signal current source override the branch current.

2.2.2 Whole-system Models

As discussed in Chapter 1.2.3, the formation of a model by identification of a source impedance and load admittance was feasible for simple power supply systems but difficult to apply in a meshed network with intermingled sources and loads and so for that reason other formulations have been sought. A useful separation is between, on the one hand, the shunt-connected apparatus appearing at nodes and, on the other hand, the lines and cables of the branches of the network that connect nodes. Thus the system is separated into a nodal admittance matrix Y_N and a apparatus matrix Y_A .

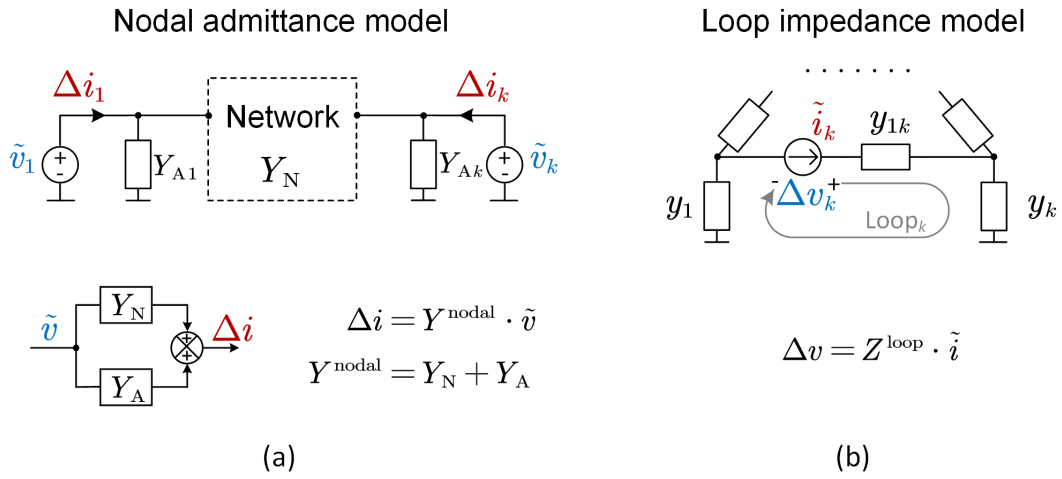


Figure 2.3: Formulation of nodal-loop models: (a) nodal admittance model Y^{nodal} . (b) Loop impedance model Z^{loop} .

These two matrices were already introduced in the nodal-loop models as (2.7) and (2.9) but here will be combined in a different manner. The whole-system impedance model Z^{sys} and the whole-system admittance model Y^{sys} are formed as illustrated in Fig. 2.4. Taking Z^{sys} as an example, the model is formed with a virtual nodal injection of current \tilde{i} whereas for the nodal admittance model the injection was a nodal voltage. The current \tilde{i} causes a change in current through the apparatus and therefore a change in the apparatus voltage Δv , which in turn creates a change of current flowing into the network Δi , which changes the current flow in the apparatus in a feedback fashion. This feedback arrangement is illustrated in Fig. 2.4(a). The response Δv to perturbation \tilde{i} is

$$\Delta v = Z_A (I + Y_N Z_A)^{-1} \cdot \tilde{i}, \quad (2.16)$$

where I is identity matrix and Z_A is the apparatus impedance matrix defined in the same fashion of Y_A but with apparatus impedance as its diagonal elements, i.e.,

$$Z_A = \begin{bmatrix} Z_{A1}(s) & & & \\ & Z_{A2}(s) & & \\ & & \ddots & \\ & & & Z_{An}(s) \end{bmatrix}, \quad (2.17)$$

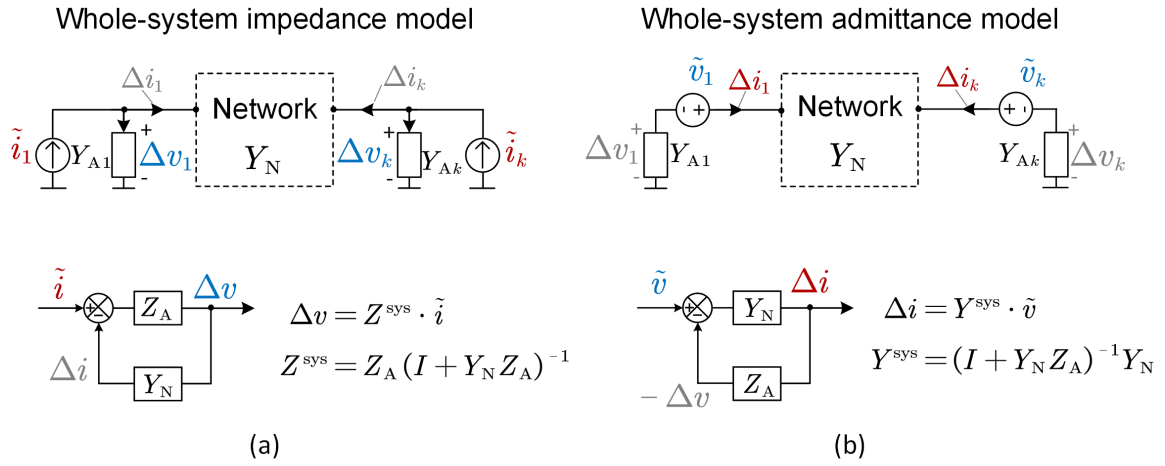


Figure 2.4: Formulation of whole-system models: (a) whole-system impedance model Z^{sys} . (b) whole-system admittance model Y^{sys} .

where $Z_{An} = Y_{An}^{-1}$. Noting that if all nodes are connected with apparatus, Z_A can be directly linked with Y_A via $Z_A = Y_A^{-1}$. However, if some nodes do not have shunt-connected apparatus, i.e., Y_A is not full, Z_A has to be calculated element-wise with those floating nodes treated as open circuits. To maintain the simplicity of theory demonstration, all nodes are considered connecting to a shunt-connected apparatus in the following analysis.

(2.16) gives rise to the definition of Z^{sys} :

$$Z^{\text{sys}} = Z_A (I + Y_N Z_A)^{-1}. \quad (2.18)$$

Similarly, the formulation of the whole-system admittance model is shown in Fig. 2.4(b), using a series injection of voltage and a response in terms of current. The model is defined as

$$Y^{\text{sys}} = (I + Y_N Z_A)^{-1} Y_N. \quad (2.19)$$

Since Z^{sys} and Y^{sys} are formulated from a closed-loop relationship between Y_N and Y_A , in accordance with the open-loop models, whole-system models can also be referred as closed-loop models.

2.2.3 Associations

Fig. 2.3(a) and Fig. 2.4(a) use the same physical arrangement of Y_N and Y_A but in the first case a nodal voltage is applied and a current change observed to define Y^{nodal} and in the second case a nodal current is injected and a nodal voltage change observed to define Z^{sys} , and thus these two models are inverses of each other as defined by

$$Y^{\text{nodal}} = (Z^{\text{sys}})^{-1}. \quad (2.20)$$

This inverse relationship can also be easily proved mathematically from (2.13) and (2.18):

$$(Z^{\text{sys}})^{-1} = (I + Y_N Z_A) Z_A^{-1} = Y_A + Y_N = Y^{\text{nodal}}, \quad (2.21)$$

It is worth noting that Z^{sys} is similar as the nodal-impedance matrix, which is the inverse matrix of Y_N and familiar from conventional power system circuit analysis. It also is worth remarking that there is no evidence of a general relationship between Z^{loop} and Y^{sys} because Z^{loop} is not a unique model because it depends on how the loops are selected.

Also, (2.19) can be used to derive the relation

$$(Y^{\text{sys}})^{-1} = Y_N^{-1} (I + Y_N Z_A) = Y_N^{-1} + Y_A^{-1}, \quad (2.22)$$

However, such a relationship is not particularly useful for system analysis because although the elements of Y_N relate to specific locations in the network, the elements of Y_N^{-1} are formed by combination of all elements Y_N which do not relate to specific locations.

2.2.4 Illustration

A simple three-node system, as shown in Fig. 2.5(a), is employed here to illustrate the formulation of networked impedance models. The admittance of the IBRs are defined as

$$Y_{A1} = \begin{bmatrix} Y_{A1,dd} & Y_{A1,dq} \\ Y_{A1,qd} & Y_{A1,qq} \end{bmatrix}, \quad Y_{A2} = \begin{bmatrix} Y_{A2,dd} & Y_{A2,dq} \\ Y_{A2,qd} & Y_{A2,qq} \end{bmatrix}, \quad Y_{A3} = \begin{bmatrix} Y_{A3,dd} & Y_{A3,dq} \\ Y_{A3,qd} & Y_{A3,qq} \end{bmatrix}, \quad (2.23)$$

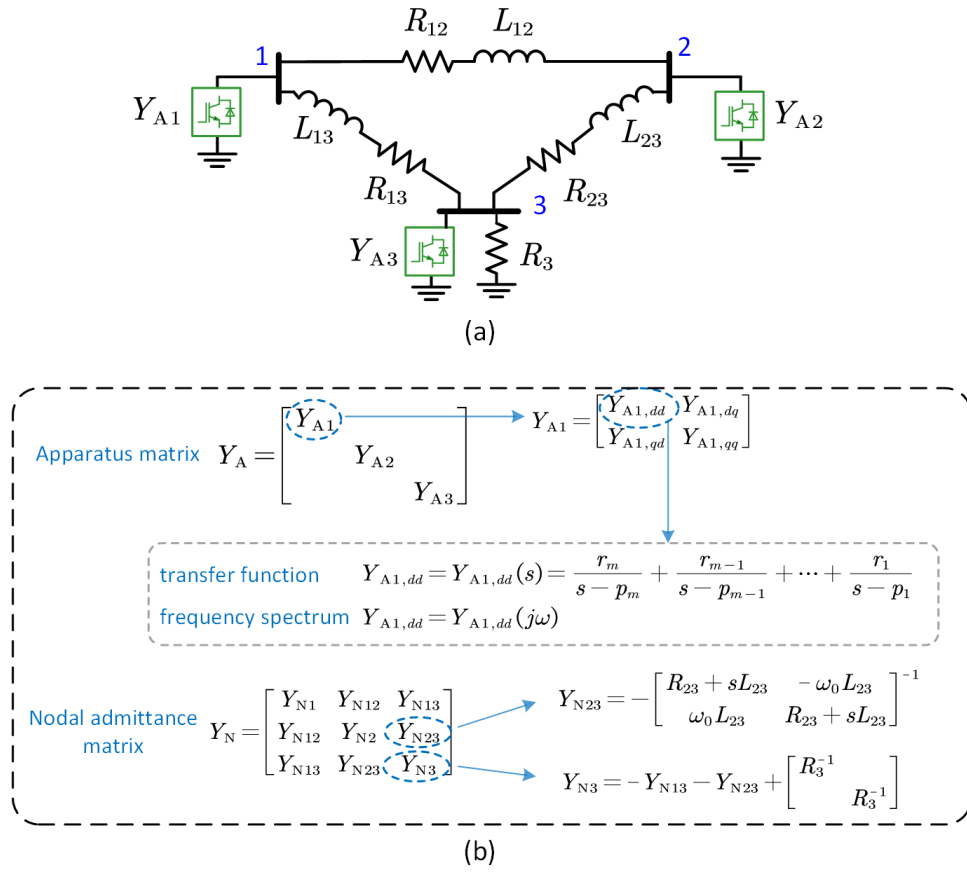


Figure 2.5: (a) A simple three-node system with two IBRs. (b) The formulation of Y_A and Y_N .

where each element inside the apparatus matrix is either a transfer function, e.g.,

$$Y_{A1,dd} = Y_{A1,dd}(s) = \frac{r_m}{s-p_m} + \frac{r_{m-1}}{s-p_{m-1}} + \dots + \frac{r_1}{s-p_1}, \quad (2.24)$$

or a frequency spectrum $Y_{A1,dd} = Y_{A1,dd}(j\omega)$, which can be represented by a Bode plot. The formulations of Y_A and Y_N of this system are illustrated in Fig. 2.5(b), where the elements in Y_N are formed based on (2.8). The apparatus impedance Z_A can also be yielded from Y_A such that

$$Z_A = \begin{bmatrix} Z_{A1} & & \\ & Z_{A2} & \\ & & Z_{A3} \end{bmatrix} = Y_A^{-1} = \begin{bmatrix} Y_{A1}^{-1} & & \\ & Y_{A2}^{-1} & \\ & & Y_{A3}^{-1} \end{bmatrix}. \quad (2.25)$$

Based on the formed Y_A , Z_A and Y_N , the nodal admittance model Y^{nodal} can be acquired using (2.13), and the whole-system impedance model Z^{sys} can be acquired using (2.18).

2.3 Relationship between Networked Impedance and State-Space

To reveal the relationship between networked impedance models and a state-space representation of a power system, the state-space equations of an m order system with n nodes are as follows:

$$\begin{aligned}\dot{x} &= Ax + Bu_{in} \\ y_o &= Cx,\end{aligned}\tag{2.26}$$

where A , B and C are the state matrix, input matrix and the output matrix, x , u_{in} and y_o are the state vector, input vector, and output vector. These state equations are usually very high-order but can be decomposed into a series of first-order (or second-order when the roots are conjugate complex numbers) equivalents via coordinate transformations $z = \Psi x$ and $x = \Phi z$, noting that $\Phi = \Psi^{-1}$, such that the state matrix in the new coordinate z is diagonalised [19], that is,

$$\begin{aligned}\dot{z} &= \Lambda z + \Psi Bu_{in}, \\ y_o &= C\Phi z \\ \Lambda &= \Psi A \Phi = \text{diag}(\lambda_1, \lambda_2, \dots, \lambda_m),\end{aligned}\tag{2.27}$$

where λ_i ($i = 1, 2, \dots, m$) is the i -th eigenvalue of A , and the rows and columns of Ψ and Φ correspond to the left- and right-eigenvectors of A , respectively. z is a vector of modes of the system and determines stability according to the corresponding eigenvalues.

Turning first to whole-system impedance models, taking Z^{sys} as an example, the same virtual injection of current input can be performed in state-space format with the voltage taken as the system's output, which can be described as follows

$$\begin{aligned}u_{in} = \tilde{i} &= [\tilde{i}_1, \tilde{i}_2, \dots, \tilde{i}_n]^T \\ y_o = \Delta v &= [\Delta v_1, \Delta v_2, \dots, \Delta v_n]^T.\end{aligned}\tag{2.28}$$

As a result, Z^{sys} is essentially the transfer function of the state-space model. From the well-known equation for the transfer function of a state-space model [19], the whole-system impedance model

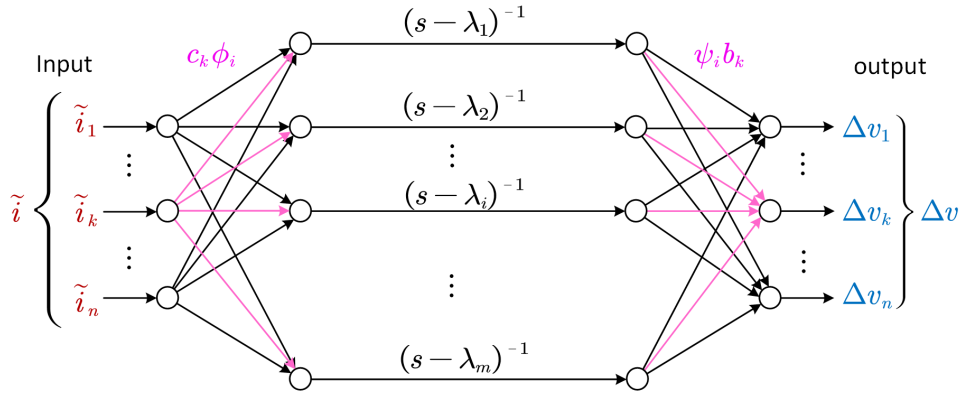


Figure 2.6: Whole-system impedance model derived from state-space representation.

can be expressed as

$$Z^{\text{sys}} = C(sI - A)^{-1}B, \quad (2.29)$$

where I is an identity matrix of order m . For instance, the k -th diagonal element of Z^{sys} is

$$Z_{kk}^{\text{sys}}(s) = \sum_{i=1}^m \frac{c_k \phi_i \psi_i b_k}{s - \lambda_i} = \sum_{i=1}^m \frac{R_{ki}}{s - \lambda_i}, \quad (2.30)$$

where c_k is the k -th row of C , b_k is the k -th column of B , ϕ_i and ψ_i are the right and left eigenvectors of λ_i , R_{ki} is the residue of $Z_{kk}^{\text{sys}}(s)$ corresponding to the pole λ_i . The relationship expressed in (2.30) is illustrated in Fig. 2.6, where $c_k \phi_i$ and $\psi_i b_k$ can be viewed as weight factors of the paths. It can be seen that all elements share the same poles, which are the eigenvalues of the system. The arrows shown in magenta represents the terms relating \tilde{i}_k to Δv_k and yielding Z_{kk}^{sys} .

We now turn to nodal admittance mode Y^{nodal} as an example. Before linking Y^{nodal} with the state-space model, it is important to clarify that for a state-space model of a power system, the input and output should be small-signal perturbations around an equilibrium point, i.e., perturbations that add onto existing steady-state values. In fact, this is a basic principle for small-signal analysis. The virtual injection of current into a node to create Z^{sys} and a series injection of voltage in series with apparatus to form Y^{sys} are injections or perturbations that add to existing nodal currents or apparatus voltage and hence they yield transfer functions of the state-space model. In contrast, the virtual injection of \tilde{v} in Y^{nodal} in parallel with nodal apparatus overrides the existing nodal voltage (the steady-state value), and thus \tilde{v} cannot be a small-signal input of the system. As a result, Y^{nodal} cannot be directly linked to the state-space model via a relationship similar to (2.29).

Nevertheless, from (2.20), it is possible to obtain

$$Z^{\text{sys}}(s) = (Y^{\text{nodal}})^{-1}(s) = \frac{\text{adj}(Y^{\text{nodal}}(s))}{\det(Y^{\text{nodal}}(s))}. \quad (2.31)$$

It is clear from (2.31) that $\det(Y^{\text{nodal}}(s))$ is the denominator polynomial for all elements in Z^{sys} . Because all elements of Z^{sys} share the same poles which are the eigenvalues of the state-space model, a conclusion can be drawn from (2.31) that the state-space eigenvalues are the roots of the equation below:

$$\det(Y^{\text{nodal}}(s)) = 0. \quad (2.32)$$

In other words, the zeros of the determinant of $Y^{\text{nodal}}(s)$ equal state-space eigenvalues. For the sake of brevity, we use λ to represent a single nonspecific eigenvalue of the state-space model, and define $\det(Y^{\text{nodal}}(s)) \triangleq Y_{\text{det}}^{\text{nodal}}(s)$ as a transfer function formed by the determinant, such that

$$Y_{\text{det}}^{\text{nodal}}(\lambda) = 0. \quad (2.33)$$

An important finding from (2.33) is that λ , an eigenvalue of the state-space matrix, is a singularity of Y^{nodal} . Therefore, (2.20) does not hold true at $s = \lambda$. It is also worth noting that the fact of $Y^{\text{nodal}}(\lambda)$ being singular holds true theoretically, but mostly cannot be observed in real. For a real physical system, $Y^{\text{nodal}}(s)$ can be a nonsingular matrix at all frequencies due to the existence of line capacitance such that the shunt impedance could never be infinite. Another explanation is that for an eigenvalue $\lambda = \sigma \pm j\omega$, a real system typically considers the case where $s = j\omega$ with the real-part σ omitted, i.e., $Y_{\text{det}}^{\text{nodal}}(j\omega) \neq 0$ if $\sigma \neq 0$. This also explains the fact that the impedance or admittance spectra are continuous at the oscillatory frequency ω but with a peak at that point, and the closer σ is to zero, the sharper the peak will be.

The relationships described here links nodal-loop models with state-space model and offer a way of assessing system stability from nodal-loop models by observing whether there are right-half-plane (RHP) zeros of the determinant. The proof of (2.33) is based on an understanding of small-signal injection connections between Y^{nodal} and Z^{sys} , and a more straightforward proof can also be found in [97].

2.4 Comparisons

2.4.1 Sensitivity/Participation Analysis

One benefit of using the nodal-loop model is that each entry in the matrix relates directly to a specific component in the network (or an aggregation of components at a node or branch), so offers explicit information on the location of an aspect of the model. For example, for Y^{nodal} , the diagonal entry Y_{ii}^{nodal} represent all admittances terminating at node i , whereas the off-diagonal entry Y_{ki}^{nodal} is the negative of the sum of admittances between node k and node i . By studying eigenvalue sensitivity with respect to entries of Y^{nodal} , the root-cause of an oscillation can be easily located to a specific shunt or series-connected item. Recognising this, the RMA method, briefly mentioned in Chapter 1.3.2, was proposed for Y^{nodal} in a drive to replicate the analysis that can be performed on the state-space matrix A in investigating the sensitivity of the ‘zero’ eigenvalue of Y^{nodal} with respect to an element Y_{ki}^{nodal} [77, 78, 82–89]. The RMA method is fully analysed in Chapter 3.1.1, and the relationship between the RMA method and eigenvalue sensitivity is the topic for investigation in Chapter 3.3.

Sensitivity or participation analysis of whole-system models had not appeared in the literature before the work reported here. In this thesis, a comprehensive theory of eigenvalue sensitivity and participation analysis will be established for whole-system model, which points out that residues of the elements of Z^{sys} and Y^{sys} can be used to derive the impedance or admittance participation factors and eigenvalue sensitivity. A grey-box approach will also be proposed to serve as a powerful tool for root-cause tracing and parameters tuning for large-scale system stability. The details will be introduced in Chapter 3.

2.4.2 Measurability

As mentioned in Chapter 1.2, impedance models can be acquired from measurement so that data-driven approaches can be applied. However, as shown in Fig. 2.3 and pointed out in Chapter 2.3, perturbation of a nodal voltage of Y^{nodal} can be considered as a theoretical step but as a practical exercise is problematic. In practice, nodes will have stiff voltage sources present, hence perturbing

the node voltage with a perturbation in parallel to conduct an online measurement of Y^{nodal} is not feasible. To acquire Y^{nodal} , admittance of each apparatus needs to be measured individually and offline and then the apparatus matrix Y_A can be formed and equation (2.13) can be applied so add Y_A to the previously known Y_N to form Y^{nodal} .

In contrast to the difficulty of measuring Y^{nodal} and Z^{loop} , measuring Z^{sys} and Y^{sys} is feasible. It is natural to connect a current perturbation source in parallel with apparatus, or a voltage perturbation source in series with apparatus, as shown in Fig. 2.4. Such feasibility allows whole-system model to be applied for data-driven methods.

2.4.3 Use with Incomplete Data

It is believed that Z^{sys} and Y^{sys} are more readily used in practice for stability analysis than Y^{nodal} because they can yield some results even with incomplete data. To analyse the oscillatory modes and their participation factors, the application of Y^{nodal} relies on the full-knowledge of the model because modes need to be calculated from its determinant. If some admittances in the system are unknown or unmeasured, even if they are unlikely to cause an instability, the matrix Y^{nodal} becomes incomplete and the expression of $\det(Y^{\text{nodal}}(s))$ cannot be acquired. Consequently, oscillatory modes and the corresponding sensitivity and participation analysis cannot be carried out in Y^{nodal} if the system is only partially known.

However, for Z^{sys} and Y^{sys} , stability analysis is undertaken element-wise because oscillatory modes can be acquired from poles of any element and participation factors can be derived from the residues of that element. If some elements in Z^{sys} or Y^{sys} are unmeasured, modes can still be acquired from other elements, and participation can be compared among all other known elements. This means that the whole-system models are more widely usable.

2.4.4 Full comparison

Fig. 2.7 shows comparisons across several different features of nodal-loop models and whole-system models.

Turning to the features of matrices, it is clear from the formulations that Y^{nodal} is a sparse matrix because nodes are connected to relative few other nodes with lines of the network. Also from (2.13) it is clear that Y^{nodal} is symmetric because Y_A is diagonal and Y_N is symmetric because if node i is connected to node j by a line impedance then j is connected to i by the same impedance. The matrix will be non-symmetric if phase-shifting transformers are present because a phase-shifting transformer at branch (i, j) creates different impact on Y_{Nik} and Y_{Nki} [98]. On the other hand, Z^{sys} and Y^{sys} are non-sparse because matrix-inverse calculations are involved in (2.18) and (2.19), but are symmetric when there are no phase-shifting transformers due to the fact that the inverse of a symmetric matrix is a symmetric matrix.

Turning to elements inside each model, the diagonal elements of Y^{nodal} are the self-admittance of the node, and each is the sum of all admittance terminating at that node, while the off-diagonal elements are mutual admittance between two nodes which are the negative sum of admittance connected between two nodes. This shows that the elements in Y^{nodal} contain explicit locational information so would be helpful for locating the oscillations in sensitivity analysis. In addition, the zeros of the determinant of Y^{nodal} are equivalent to the state-space eigenvalues. For Z^{sys} and Y^{sys} , all elements share the same poles which equal the state-space eigenvalues, so that all elements contain dynamics of the whole-system. A weakness compared with Y^{nodal} is that the elements in whole-system models have no specific physical meaning as they are formed via closed-loop combination of two matrices.

For root-cause analysis, the RMA method has been developed for Y^{nodal} where the sensitivity of the zero eigenvalue of $Y^{\text{nodal}}(\lambda)$ is studied. For whole-system models, the development of a root-cause analysis method is an objective of this thesis.

In contrast to the difficulty of measuring Y^{nodal} and Z^{loop} online with parallel voltage or series current perturbations, measuring Z^{sys} and Y^{sys} online with parallel current or series voltage perturbations is feasible.

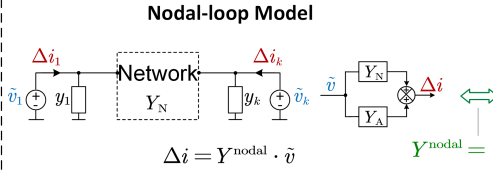
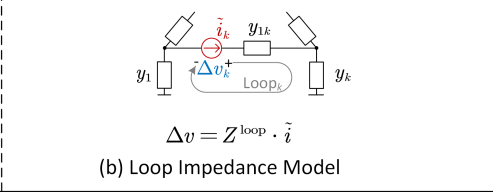
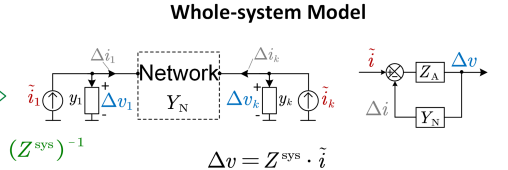
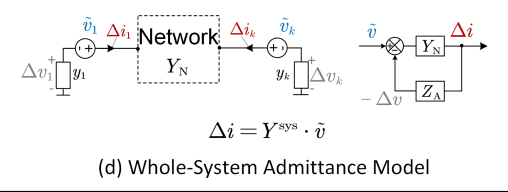
<p>Understanding from voltage /current injections</p> <p>small-signal injections: $\tilde{v} = [\tilde{v}_1, \dots, \tilde{v}_n]^T$ $\tilde{i} = [\tilde{i}_1, \dots, \tilde{i}_n]^T$</p> <p>small-signal outputs: $\Delta v = [\Delta v_1, \dots, \Delta v_n]^T$ $\Delta i = [\Delta i_1, \dots, \Delta i_n]^T$</p>	<p>Nodal-loop Model</p>  <p>(a) Nodal Admittance Model</p>  <p>(b) Loop Impedance Model</p>	<p>Whole-system Model</p>  <p>(c) Whole-System Impedance Model</p>  <p>(d) Whole-System Admittance Model</p>
<p>Formulation</p> $Y_A = \text{diag}(Y_{A1}, Y_{A2}, \dots, Y_{An})$ $Z_A = Y_A^{-1}$	<ul style="list-style-type: none"> • open-loop $Y^{\text{nodal}} = Y_N + Y_A$ Z^{loop} is dependent on how loops are selected 	<ul style="list-style-type: none"> • closed-loop $Z^{\text{sys}} = Z_A (I + Y_N Z_A)^{-1}$ $Y^{\text{sys}} = (I + Y_N Z_A)^{-1} Y_N$
<p>Matrix Features</p>	<ul style="list-style-type: none"> • Sparse • Symmetric (if there are no phase-shifting transformers) 	<ul style="list-style-type: none"> • Non-sparse • Symmetric (if there are no phase-shifting transformers)
<p>Element Features</p>	<ul style="list-style-type: none"> • Diagonal: self-admittance/impedance of the node/loop • Off-diagonal: mutual admittance/impedance of the node/loop 	<ul style="list-style-type: none"> • All elements share the same poles • Elements have no specific physc meaning • All elements contain dynamics of the whole-system
<p>Relationship with State-space</p>	<ul style="list-style-type: none"> • Zeros of the determinant equal state-space eigenvalue λ 	<ul style="list-style-type: none"> • Poles of all elements equal state-space eigenvalue λ
<p>Root-cause method</p>	<ul style="list-style-type: none"> • RMA method based on critical admittance-eigenvalue sensitivity: the sensitivity of zero eigenvalue of Y^{nodal} 	<ul style="list-style-type: none"> • An objective of this thesis: Impedance/admittance participation factors and sensitivity factors based on residues of elements.
<p>Online Measurability</p>	<ul style="list-style-type: none"> • Not feasible 	<ul style="list-style-type: none"> • Feasible
<p>Usability</p>	<ul style="list-style-type: none"> • Not usable if model is only partially known 	<ul style="list-style-type: none"> • Usable if model is only partially known

Figure 2.7: Comparisons of networked impedance models.

Despite that Y^{nodal} cannot be applied for modal analysis if the model is only partially known, Z^{sys} and Y^{sys} can be used for modal analysis even if some of the matrix elements are unmeasured.

Comparing across all models in Fig. 2.7, one can conclude that for systematic analysis, nodal analysis is preferred because there is an exclusive definition for a given power system, which is not the case for loop analysis because loops can be selected in several different ways. Considering this, Z^{loop} will not be discussed further. For the further examinations, the models Y^{nodal} , Z^{sys} and Y^{sys} will be the main focus.

2.5 Summary

This chapter analyses the two types of networked impedance models and performs a comparative study. The formulations and associations of the two types of networked impedance models, namely, nodal-loop models and whole-system models, are introduced and fully analysed, with a simple three-node system provided for illustration. The relationship between the networked impedance model and the state-space model is also clarified, revealing the potential of the networked impedance models for stability assessment similarly as the conventional state-space model. A comparative study is further performed to compare the two types of networked impedance models in different aspects so that their relative merits are established. The contents of this chapter serve as the basis of impedance-based stability analysis in power systems.

Chapter 3

Root-cause Analysis in Networked Impedance Models

This chapter focuses on the root-cause analysis in networked impedance models, including eigenvalue sensitivity and participation analysis. A three-layer grey-box approach is then proposed as a systematic way to facilitate root-cause tracing to different depths, i.e. to apparatus and to parameters, according to the available information. The outcomes have been published as two research papers [95, 96], and some sentences and figures are reused.

3.1 Review of Existing Modal Analysis Methods in Impedance Models

After establishing the networked impedance models, researchers devoted considerable effort to replicating the state-space modal analysis in impedance models, i.e., eigenvalue sensitivity and participation factor. So far, two major impedance-based modal analysis approaches have been developed: the RMA method and the Nyquist-based participation analysis. These two methods are reviewed in this section.

3.1.1 The Resonance mode analysis Method

A Development

Xu's group [82–84] first developed a method to perform eigenvalue sensitivity analysis in nodal admittance matrix, and named it resonance mode analysis (RMA). The RMA method was initially used to investigate the sensitivity of the smallest eigenvalue of $Y_N(j\omega_r)$, where Y_N is the conventional nodal admittance matrix as defined in (2.7) and ω_r refers to a resonant frequency in the system. This smallest eigenvalue has been referred to as the critical mode, the critical resonance mode, or the critical eigenvalue. Because such an 'eigenvalue' is an eigenvalue of $Y_N(j\omega_r)$, a careful distinction between it and a state-space eigenvalue λ is drawn in this thesis, and the term 'critical admittance-eigenvalue' is chosen to refer to it. In this thesis, we use λ to represent the eigenvalues of state-space matrix A , referred to simply as eigenvalues, and use γ to represent the critical admittance-eigenvalues. Based on the definition from Xu's group,

$$\gamma = \min \{|\text{eig}(Y_N(j\omega_r))|\}. \quad (3.1)$$

Two important conclusions are derived from the RMA method:

- 1) The critical eigenvalue of $Y_N(j\omega_r)$ is the main cause of the observed resonance phenomenon with frequency of ω_r .
- 2) A critical admittance-eigenvalue sensitivity matrix S_γ can be directly calculated from the outer product of the left and right critical eigenvectors of $Y_N(j\omega_r)$, in which the entry in the i -th row and the k -th column, $S_{\gamma,ik}$, is the sensitivity of γ with respect to the (k, i) element of Y_N , as shown below:

$$\begin{aligned} S_\lambda &= u_\gamma \otimes w_\gamma = u_\gamma w_\gamma^\top \\ S_{\gamma,ik} &= \frac{\partial \gamma}{\partial Y_{Nki}}, \end{aligned} \quad (3.2)$$

where u_γ and w_γ are the left and right critical eigenvectors of $Y_N(j\omega_r)$ corresponding to γ .

By analysing the sensitivity of γ with respect to the impedance of components, the RMA method is shown to be effective in locating potential root-causes of system oscillations. An alternative concept, based on RMA, of modal frequency sensitivity was proposed in [85]. Modal frequency analysis gives an insight into the degree of a components' influence on the resonance frequency. However, the resonance frequency of one mode may be the same or similar to that of other modes, i.e., modes with same imaginary parts but different real parts and so the advantage of original RMA to analyse specific modes is lost. To avoid such an issue, [86] extended the critical admittance-eigenvalue sensitivity matrix to complex form, which is a combination of impedance sensitivity and frequency sensitivity and provides fuller view to the root-cause of oscillations.

Hereto, the RMA method and its variants can be considered as initial versions, because they neglect the dynamic characteristics of all generators or IBRs and only consider the passive components in the system. Nevertheless, the invention of the RMA method is a starting point for using impedance models for sensitivity analysis and root-cause tracing of oscillations, creating a widespread impact on further studies.

Recent research has advanced RMA to a new stage where dynamics of active sources are also included [77, 78, 87–89]. In [87], the RMA method is applied on a wind farm consists of 150 wind turbines, where the harmonic model of each wind turbine (an double-feed induction generator) is established so that it can be included in the nodal admittance matrix together with power cables and transformers. The RMA method is further carried out in the newly assembled nodal admittance matrix to assess the degree of involvement of each node in different resonance modes. This work brought the dynamics of IBRs into the nodal admittance matrix so offers more precise knowledge towards the root-cause analysis than the initial versions of RMA, yet the focus is only on the harmonic frequencies (integer multiples of the fundamental frequency) with other frequencies omitted. Further studies extended the nodal-admittance matrix Y_N to a transfer function matrix, i.e., nodal admittance model Y^{nodal} and loop impedance model Z^{loop} discussed in the previous subsection, rather than numerical matrices, thus covers a certain frequency range. In [77], a bus participation factor is calculated and analysed in a wind farm based on Y^{nodal} , where buses with a larger participation factor are identified as amplifying disturbances (around the frequency of the resonance mode) more than the other buses. In [78], the theory of RMA is formally extended to frequency-domain with each apparatus included, such that the

dynamic characteristics of the whole-system are all included in Y^{nodal} . As discussed in Chapter 2.3, $\det(Y^{\text{nodal}}(\lambda)) = 0$, i.e., there must be at least one eigenvalue of $Y^{\text{nodal}}(\lambda)$ equal to zero, which is the corrected version of critical admittance-eigenvalue concept and stands in contrast with (3.1), i.e.,:

$$\gamma \in \text{eig}(Y^{\text{nodal}}(\lambda)), \gamma = 0. \quad (3.3)$$

Still, the core of the updated theory follows the RMA method: a sensitivity matrix is calculated from the outer product of the left and right critical eigenvectors of $Y^{\text{nodal}}(\lambda)$. [78] also put forward an important idea that if $\frac{\partial y}{\partial \rho}$ is further known, where y is the admittance of an apparatus and ρ is a parameter of it, manufactures would be able to know which parameter would be the most effective one to affect the mode. Such advantage is helpful for system tuning. It is worth noting that since the study has now been brought into frequency-domain, some recent research also refers to RMA as frequency-domain modal analysis (FMA). [88] further defines the concepts of modal observability and modal controllability, which are derived from the left and right eigenvectors of $Y^{\text{nodal}}(\lambda)$ respectively, aiming to find the best observing location and best tuning location for an oscillatory mode. However, as calculated in [88], the modal observability and modal controllability are numerically equal, i.e., they are equivalent as the critical admittance-eigenvalue sensitivity value which is the product of the two. In [89], the RMA method is further applied to a hybrid AC/DC grid, in which oscillations are confined in some local areas without propagating to the entire system with the help of AC/DC converters acting as barriers.

In conclusion, the RMA method has been proved to be effective for root-cause tracing, and has created a wide impact on topic of power system stability.

B Underlying Principle

Because the frequency-domain RMA method is proposed recently, several underlying principles have not been explicitly clarified in previous research and some proofs may have flaws. To this end, here, detailed analysis and discussions are given to illustrate the underlying principles of the RMA method.

First, it is important to notice the difference between a critical admittance-eigenvalue, which is the

‘eigenvalue’ studied in the RMA method, and an ‘eigenvalue’ of the state-space. A state-space eigenvalue λ is an eigenvalue of state transition matrix A with value of

$$\lambda \in \text{eig}(A), \lambda = \sigma \pm j\omega. \quad (3.4)$$

For system stability analysis, λ is recognised as an oscillatory mode, where the real-part σ is considered as the damping of the mode because $1/|\sigma|$ gives the time-constant of the decay of oscillation amplitude, and the imaginary part ω is the natural frequency of the mode with the unit of rad/s . This has been well studied in [19]. Typically, for a system which is stabilised at the operating point (with no eigenvalues in the RHP), the modes of most concern are those conjugate complex pairs with small absolute values of their real-part, which are described as modes with low damping and which to induce oscillations during transient periods such as step change in a power injection. Considering this, the sensitivity of mode λ with respect to components and parameters is of great value for analysing the root-cause of the oscillation.

In contrast, for the RMA method, the focus is not on mode λ , but on the critical admittance-eigenvalue γ , which is the zero-eigenvalue of $Y^{\text{nodal}}(\lambda)$, as given in (3.3).

For a better illustration, a property about eigenvalue is introduced here:

Property 3.1 *Let Y be a $n \times n$ matrix, the product of the n eigenvalues of Y is the same as the determinant of Y .*

First it is certain that a zero-valued critical admittance-eigenvalue γ exists because λ is a zero of the determinant of Y^{nodal} , i.e., $\det(Y^{\text{nodal}}(\lambda)) = 0$. According to property 3.1, it is clear that there is at least one eigenvalue of $Y^{\text{nodal}}(\lambda)$ that equals zero. Here a very important premise is introduced:

Premise 3.1 *λ is assumed to be a non-repeated eigenvalue of A .*

Under this premise, as proved in A.1, the number of zero-valued eigenvalues of $Y^{\text{nodal}}(\lambda)$ does not exceed one. Therefore, there is one and only one γ corresponding to each λ . Such a premise was implicitly relied upon in the literature, e.g., [77, 78, 89] but not specifically mentioned.

It has been stated in the literature [77, 78] that γ is the main factor determining the characteristics of the mode being examined, but the proof of this finding has some flaws. Previous research proves it by using the idea of modal current injection at the modal frequency [77, 78]. The proof relies on a calculation of the inverse of the diagonalised matrix of $Y^{\text{nodal}}(\lambda)$, where the term γ^{-1} dominates modal current because $\gamma^{-1} = \infty$. However, as mentioned below (2.33), Y^{nodal} is a singular matrix at $s = \lambda$ and therefore its inverse matrix does not exist, neither does the inverse of its diagonalised matrix, a fact overlooked in the previous proofs. This fact was noticed in [77] but dealt with by stating that γ is close to but not exactly zero because of round-off errors of floating-point computations, but this is not a convincing argument. To avoid this difficulty, we prove the effect of γ using a new method based on small-signal perturbation, as shown in Appendix A.2. The proof shows that for a variation of a physical parameter $\Delta\rho$ in the system, the corresponding variation $|\Delta\gamma|$ is proportional to the variation of the mode $|\Delta\lambda|$, i.e.,

$$|\Delta\gamma| \propto |\Delta\lambda|, \text{ for } \rho = \rho + \Delta\rho \quad (3.5)$$

Consequently, the sensitivity $\frac{\partial\gamma}{\partial Y_{ki}^{\text{nodal}}}$ also reflects the sensitivity of the mode with respect to Y_{ki}^{nodal} .

Based on the above findings, it can also be inferred that the sensitivity of γ with respect to an element of the nodal admittance $\frac{\partial\gamma}{\partial Y_{ki}^{\text{nodal}}}$ is proportional to the sensitivity of oscillatory mode λ with respect to Y_{ki}^{nodal} , such that

$$\left| \frac{\partial\gamma}{\partial Y_{ki}^{\text{nodal}}} \right| \propto \left| \frac{\partial\lambda}{\partial Y_{ki}^{\text{nodal}}} \right|, \text{ at } s = \lambda. \quad (3.6)$$

The relationship in (3.6) is important because the term Y_{ki}^{nodal} relates to a line or apparatus at a specific location and λ refers to the oscillatory mode, so that $\frac{\partial\lambda}{\partial Y_{ki}^{\text{nodal}}}$ can help to trace the location of the cause of poorly damped or unstable modes in the system. Even though the value of $\frac{\partial\lambda}{\partial Y_{ki}^{\text{nodal}}}$ is not made available, the value of $\frac{\partial\gamma}{\partial Y_{ki}^{\text{nodal}}}$ can be easily calculated because γ is an eigenvalue of $Y^{\text{nodal}}(\lambda)$. By using the same method of eigenvalue sensitivity described in [19], a critical admittance-eigenvalue sensitivity matrix is then defined as S_γ , in which the entry in the i -th row and the k -th column, $S_{\gamma,ik}$,

is the sensitivity of γ with respect to the (k, i) element of $Y^{\text{nodal}}(\lambda)$, as shown below:

$$\begin{aligned} S_\gamma &= u_\gamma w_\gamma^\top \\ S_{\gamma,ik} &= \frac{\partial \gamma}{\partial Y_{ki}^{\text{nodal}}}, \end{aligned} \quad (3.7)$$

where w_γ and u_γ are the left and right eigenvectors of $Y^{\text{nodal}}(\lambda)$ corresponding to γ , and are normalised as $w_\gamma^\top u_\gamma = 1$. This finding is encouraging because it has the same format as the sensitivity analysis in a state-space model: the outer product of left and right vectors. By comparing $\frac{\partial \gamma}{\partial Y_{ki}^{\text{nodal}}}$, system operators can determine which components dominate in γ , and this gives general indication of the root-cause of the oscillatory mode λ .

Nevertheless, several obvious drawbacks can be noticed for the RMA method as below:

- 1) Unlike λ which represents an oscillatory mode in the system, γ does not have clear physical meaning. The underlying association between γ and λ is also ambiguous. As a result, the sensitivity of γ cannot reflect a component's separate influence on damping σ and frequency ω .
- 2) The critical admittance-eigenvalue sensitivity can only provide some imprecise indication of the root-cause of oscillations. It is reported that buses with large sensitivity values do not necessarily mean that the oscillations can be effectively mitigated by adjusting components at those buses [83].
- 3) The sensitivity values in S_γ are complex but it has not been established how to interpret the real and imaginary parts, and previous studies resort to comparing the absolute values. It is also not clear how to compare the sensitivity in a three-phase system, where the sensitivity values are 2×2 matrix blocks in the d - q frame and not a single value.
- 4) Y^{nodal} or Z^{loop} cannot be measured online, hence the RMA method can not be applied as a measurement-based, data-driven method for stability assessment.

To address the above obstacles, the most straightforward way is to create a method to find the value of

$\frac{\partial \lambda}{\partial Y_{ki}^{\text{nodal}}}$, to develop a method to produce a single (complex valued) indication in place of a 2×2 matrix

block in d - q frame, and to identify clear meanings of the real and imaginary parts of the complex number.

3.1.2 Nyquist-based Participation Analysis for the Whole System

Because of the drawbacks of the RMA method, some very recent studies have turned back to Nyquist stability analysis to seek solutions for participation factors in impedance models [90–92].

In [90, 91], $L(s)$, a return-ratio matrix, or so-called minor loop gain, of the whole network is first defined as

$$L(s) = Y_N(s)Z_A(s). \quad (3.8)$$

Such process is to extend the application of Nyquist criteria to the whole network rather than at a PCC only. From (2.18), it is clear that $L(s)$ is actually the loop transfer function of the system while $Z^{\text{sys}}(s)$ is the closed-loop transfer function. Eigenvalues of $L(s)$ are then calculated, referred as characteristic loci [90], critical minor loop gain [91], or eigenloci [92]. In this thesis, we simply call them eigenloci (or eigenlocus for singular), and use $\iota(s)$ to refer to a non-specific eigenlocus, i.e.,

$$\iota(s) \in \text{eig}(L(s)). \quad (3.9)$$

For a network with n buses, the number of the eigenloci is n . i.e.,

$$\iota(s) \in \{\iota_1(s), \iota_2(s), \dots, \iota_n(s)\}. \quad (3.10)$$

For stability analysis, each of the eigenloci needs to be assessed individually, and the system is stable only if all $\iota(s)$ satisfy the single-input and single-output (SISO) Nyquist criteria [91], which has been introduced in Chapter 1.2.3. Fig. 3.1 [90] illustrates the eigenloci of an eight-node system where eight eigenloci are presented. Although not specifically mentioned, it is inferred that only results on d - d axis are presented here. It can be seen that ι_1 and ι_2 encircle $(-1, 0j)$, indicating that the system is unstable [90].

Nyquist-based participation factors are calculated from the left and right eigenvectors of $L(s)$ to

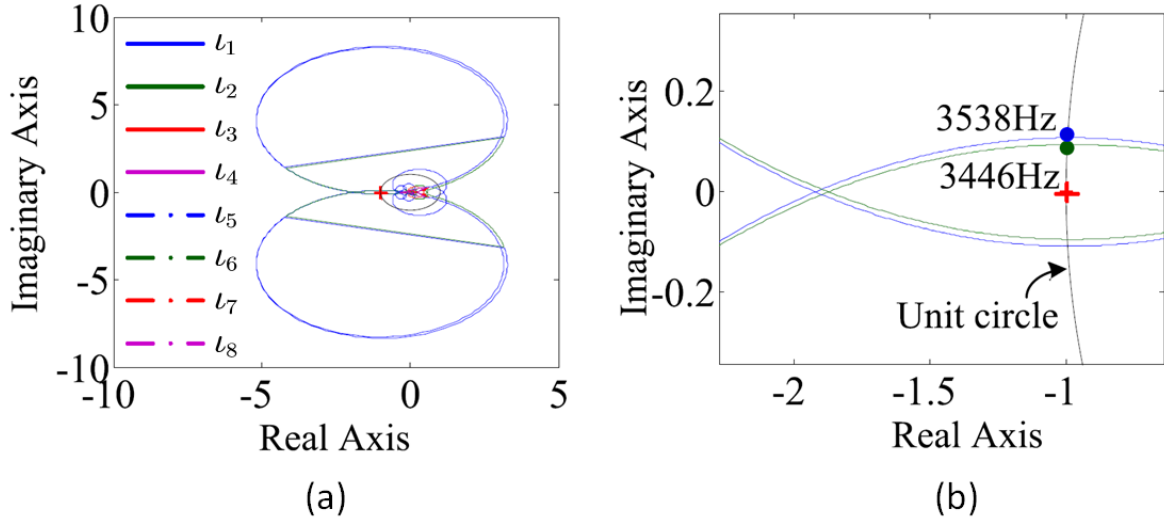


Figure 3.1: Eigenloci of $L(s)$ in an eight-node system: (a) full view, (b) zoomed-in view. l_1 and l_2 encircle $(-1, 0j)$ so that the system is unstable [90]. Copyright © 2021, IEEE.

identify the critical apparatus shaping the eigenloci. For example, the Nyquist-based participation of the apparatus at the k -th node to $l_i(s)$ is

$$p_{i,k} = w_{i,k} u_{i,k}, \quad (3.11)$$

where $w_{i,k}$ and $u_{i,k}$ are the k -th element of the left and right eigenvectors of $L(s)$ corresponding to $l_i(s)$. The so-defined participation factor is derived in a similar method as the participation factor in state-space, i.e., the physical meaning supporting this conclusion is

$$p_{i,k} = \frac{\partial l_i}{\partial L_{kk}} = \frac{\partial l_i}{\partial (Y_N Z_A)_{kk}}. \quad (3.12)$$

(3.12) can be proved by using the eigenvalue perturbation method, which has been demonstrated in [19] so is not repeated here. Because Z_A is a diagonal matrix, $(Y_N Z_A)_{kk} = Y_{Nkk} Z_{Ak}$. If the network nodal admittance matrix Y_N is considered unperturbed, it is easy to have

$$p_{i,k} = \frac{1}{Y_{Nkk}} \cdot \frac{\partial l_i}{\partial Z_{Ak}}, \quad (3.13)$$

where Z_{Ak} refers to the impedance of the apparatus connected at node- k , such that the value $\frac{\partial l_i}{\partial Z_{Ak}}$ can indicate the participation of the k -th apparatus to the i -th eigenlocus. Here, it is important to notice that the factor derived from (3.11) need to multiply by a coefficient Y_{Nkk} to get a correct measure

of the participation of an apparatus to an eigenlocus $\frac{\partial \iota_i}{\partial Z_{Ak}}$, but this coefficient is omitted by previous research. As a result, the participation factors derived in previous research may not correctly indicate the dominating apparatus of an eigenlocus.

To analyse the so-defined Nyquist-based participation factors, one or several critical eigenloci need to be picked out for further comparisons. Here, ‘critical’ refers to the eigenloci which is most close to $(-1, 0)$ for stability systems, or which encircle $(-1, 0)$ for unstable system, and $L(s)$ is considered to have no RHP poles. It is also worth mentioning that the participation factor calculated from (3.11) is essentially a transfer function and needs to be turned into numerical values for comparisons. In [90], the participation factors are compared at the ‘unstable frequencies’ without discussing the reason behind this choice. The definition of the ‘unstable frequencies’ is also not clear, but can be inferred as the frequency of the oscillations observed from time-domain simulations. In [91], the factors are compared at the cross-over frequency of the gain, which can be understood as estimating the influence of a component on the phase-margin of $\iota(s)$, which is more comprehensive. However, as pointed by [92], in some cases, the apparatus with the largest Nyquist-based participation factor at the cross-over frequency turns out to be less important for stability. This indicates that by only comparing the results at the cross-over frequency, incorrect conclusion could be drawn. The reason behind such finding is not discussed in [92] but might be caused by omitting the aforementioned coefficient Y_{Nkk} .

[92] further extends the above participation factor comparisons to a frequency range comparison, i.e., frequency-domain participation analysis. In this method, a critical eigenloci of the system is first identified, and the critical frequency and the critical frequency range that tends to influence the encirclement of the Nyquist curve around $(-1, 0)$ are found. The participation analysis is then carried out on Bode plots by comparing the magnitude of each participation factors in the frequency range. It is shown that the results of such analysis can correctly indicate which port or subsystem influences the stability the most significantly. However, unlike numerical values which are straightforward for comparisons, comparing Bode plots in a certain frequency range involves human judgements which requires more efforts and can be affected by individual subjective judgements.

Although opening up a new perspective on participation analysis, the participation factor developed in Nyquist diagrams may encounter several difficulties:

- 1) Unlike the state-space or the RMA method which studied the participation of components in an oscillatory mode, the Nyquist-based participation factors study the participation of components in an eigenlocus $\iota(s)$. Because an eigenlocus is not directly linked with time-domain oscillations, the Nyquist-based participation factor is difficult to understand from a physical perspective.
- 2) The Nyquist-based participation factors are essentially transfer functions not scalar values. Although methods have been proposed to compare them at instability frequencies, the cross-over frequency or in a certain frequency range, the physical meaning behind them is not yet fully understood.
- 3) Each eigenlocus of $L(s)$ carries information of all oscillatory modes. The Nyquist-based participation factors focus on the 'critical eigenloci', but omit others. In a case where several eigenloci are together close to $(-1,0)$, the participation of a component in an oscillation will be represented by several transfer functions together. No such case has been discussed and it is not clear how to merge these results into a single measure for further comparison.
- 4) The comparisons of the Nyquist-based participation factors are all undertaken on magnitude alone with the phase information, which is potentially meaningful, omitted.

In general, the Nyquist-based participation analysis offers some convenience for participation analysis because the return-ratio matrix $L(j\omega)$ can be acquired and applied based on measurement results without curve fitting. However, the relationship between the eigenvalue of the return-ratio matrix and the physical oscillatory modes has not been established, nor has a systematic method of comparing the Nyquist-based participation factors been established.

3.1.3 Key Research Gaps and Work Described in this Chapter

A conclusion from the review of literature set out above is that each method for root-cause analysis of small-signal instability possesses certain merits and none is a perfect solution for system with high-level of IBRs. In particular, the available methods of eigenvalue sensitivity and participation factor

assessment for impedance models are less precise and clear than their equivalents in state-space models, for instance being restricted to comparing the magnitude of complex quantities with no meaning attached to the angles, or forming judgements by visual inspection, and from these indications having to tune parameters according to experience. There is no method providing a standard and unambiguous procedure for sensitivity and participation analysis, i.e., a whole procedure that can determine the major participants of modes, the badly-tuned components, the most effective parameters inside these components, and eventually offer precise tuning guidance on these parameters.

To fill this important gap between the methods available in state-space models and the methods in impedance models, a comprehensive theory for eigenvalue sensitivity and participation factor in impedance models was sought and will be described in what follows. A two step process, connected by a chain-rule, is proposed to link impedance models with classic state-space model so as to prove that black-box impedance models have potential to offer as much information as state-space models. The study of eigenvalue sensitivity and participation factors are further carried out in impedance models, which for the first time uses an impedance model to provide sensitivity information relating to a classic state-space eigenvalue rather than a critical admittance-eigenvalue or eigenloci. A systematic way of comparing the sensitivity/participation results is also proposed through a three-layer grey-box view, serving as a powerful tool to extract almost the same information from a black-box impedance model as from a white-box state-space model. Table 3.1 presents a comparison between existing methods of participation analysis and the method established in this thesis. It shows significant advantages for the proposal and these constitute the main contributions of this chapter.

These outcomes have been published as two research papers [95, 96].

Table 3.1: Comparisons of different methods for power system root-cause tracing

Categories and Methods	State-space	Impedance models			
	Classic modal analysis [19,24]	Initial versions of RMA [82–86]	Frequency-domain RMA [77, 78, 87–89]	Nyquist-based participation factor [90–92]	Method in this thesis [95, 96]
Matrix used	A	$Y_N(j\omega_r)$	$Y^{\text{nodal}}(s)$	$L(s)$	$Y^{\text{nodal}}(s)$, $Z^{\text{sys}}(s)$, or $Y^{\text{sys}}(s)$
Eigenvalue studied	λ , eigenvalue of A	minimum eigenvalue of $Y_N(j\omega_r)$	γ , critical admittance-eigenvalue	$\iota(s)$, eigenvalue of $L(s)$	λ , eigenvalue of A
Explicit connections between studied eigenvalue and mode	+	–	–	–	+
Includes dynamics of apparatus	+	–	+	+	+
Applicability to systems with black-box models	–	–	+	+	+
Separate sensitivity of damping and natural frequency	+	–	–	–	+
Determination of dominant buses or apparatus	+	+	+	+	+
Precise parameter tuning guidance for stabilisation	+	–	–	–	+
Online measurement	–	–	–	+	+
d - q frame comparisons	+	–	–	–	+
Systematic analysis procedure	+	–	–	–	+

3.2 Participation Analysis in Impedance Models

As a route to participation factors and eigenvalue sensitivity analysis in impedance model, we can return to the underlying relationship between impedance models and state-space models as set out in Chapter 2.3 and attempt to extract close to the same information from impedance, a black-box model, as from a state-space, a white-box model. This opening up of a black-box model has the potential to be very useful in networks with many pieces of apparatus such as IBR for which only black-box models are available.

3.2.1 Impedance Participation Factor

From the transfer-function expression of a diagonal element in whole-system impedance Z_{kk}^{sys} , as given in (2.30), it is clear that the eigenvalues of the state matrix appear as poles. Meanwhile, the residue corresponding to the i -th eigenvalue λ_i is

$$R_{ki} = c_k \phi_i \psi_i b_k, \quad (3.14)$$

where c_k is the k -th row of state-space output matrix C , b_k is the k -th column of state-space input matrix B . If for a special case where the k -th element in c_k and b_k equal 1 and all other elements equal 0, which means that both B and C are identical matrices, the above equation then simplifies to a product of only the right and left eigenvectors, that is,

$$R_{ki} = \psi_{ik} \phi_{ki} = p_{ki}. \quad (3.15)$$

In this special case, the residue of Z_{kk}^{sys} has become identical to a state participation factor, p_{ki} , as defined in state-space model. This is an important observation which hints that residues being useful for participation analysis. However, (3.15) is based on a strong assumption about B and C which may not hold for common cases. A general residue-participation relationship which yields the impedance participation factor needs to be identified.

In order to clarify the roles of residues in participation analysis in a general form, Lemma 1 is introduced here.

Lemma 1 *For a square transfer function matrix G_ρ depending on parameters ρ , let H_ρ be the inverse transfer function of G_ρ , i.e. $H_\rho = G_\rho^{-1}$, and λ be a non-repeated pole of G_ρ . When the parameters ρ are perturbed infinitesimally by $\Delta\rho$, λ and H_ρ are perturbed by $\Delta\lambda$ and ΔH_ρ correspondingly and we have the following relationship:*

$$\Delta\lambda = \langle -\text{Res}_\lambda^* G_\rho, \Delta H_\rho(\lambda) \rangle \quad (3.16)$$

in which $\langle \cdot, \cdot \rangle$ is the Frobenius inner product of two matrices, $\text{Res}_\lambda G_\rho$ is the residue matrix of G_ρ at

λ (the residue operates element-wise on a matrix), $*$ denotes the conjugate transpose of the residue matrix, and the equation holds in the sense of neglecting high-order infinitesimals.

The proof of the Lemma 1 is given in Appendix A.3, and a brief introduction to the mathematical preliminaries used in this Lemma is included in Appendix B. Lemma 1 proves that in a system where a parameter is perturbed, $\Delta\lambda$ can be calculated via the corresponding residues of whole-system models, and the 2×2 matrix blocks in d - q frame can be integrated into a single complex value according to Frobenius inner product. A simple example to illustrate this Lemma is provided in Appendix C.1.

If we take G_ρ to be the whole-system admittance seen at node k defined in Chapter 2, that is, $G_\rho = Y_{kk}^{\text{sys}}$, the corresponding H_ρ is

$$H_\rho = (Y_{kk}^{\text{sys}})^{-1} = Z_{Ak} + Z_{Gk}, \quad (3.17)$$

where Z_{Ak} is the impedance of the apparatus connected at the k -th node and Z_{Gk} is impedance of the rest of the grid seen from the k -th node. It is obvious that the two impedances are independent. When Z_{Ak} itself is subject to a perturbation, Z_{Gk} will remain unchanged, that is, $\Delta Z_{Gk} = 0$, so we have

$$\Delta H_\rho = \Delta Z_{Ak} + \Delta Z_{Gk} = \Delta Z_{Ak} \quad (3.18)$$

and hence

$$\Delta\lambda = \langle -\text{Res}_\lambda^* Y_{kk}^{\text{sys}}, \Delta Z_{Ak}(\lambda) \rangle. \quad (3.19)$$

Recall that the pole λ of the transfer function Y_{kk}^{sys} is exactly an eigenvalue of the system. Therefore, (3.19) implies that the sensitivity of an eigenvalue to an apparatus impedance is determined by the whole-system admittance seen by that apparatus. Since Y_{kk}^{sys} is a diagonal element of Y^{sys} , and similarly to the state-space formulation, we define the negative values of residue as the *impedance participation factor*

$$p_{\lambda, Z_{Ak}} \triangleq -\text{Res}_\lambda^* Y_{kk}^{\text{sys}} \quad (3.20)$$

such that

$$\Delta\lambda = \langle p_{\lambda, Z_{Ak}}, \Delta Z_{Ak}(\lambda) \rangle. \quad (3.21)$$

Due to impedance-admittance duality, we can similarly define the *admittance participation factor* as the residue of the whole-system impedance

$$p_{\lambda, Y_{Ak}} \triangleq -\text{Res}_{\lambda}^* Z_{kk}^{\text{sys}} \quad (3.22)$$

such that

$$\Delta\lambda = \langle p_{\lambda, Y_{Ak}}, \Delta Y_{Ak}(\lambda) \rangle \quad (3.23)$$

where Y_{Ak} is the admittance of the k -th apparatus and Z_{kk}^{sys} is the whole-system impedance at the k -th node. The impedance and admittance participation factors are theoretically equivalent but each may better serve different applications, depending on which is more readily available, and on the application. In general, on the one hand, the negative of residues of Y_{kk}^{sys} equal the impedance participation factors of the apparatus connected in series with the k -th voltage injection source. On the other hand, the negative of residues of Z_{kk}^{sys} lead to the admittance participation factors of apparatus connected in parallel with the k -th current injection source.

3.2.2 Parameter Participation Factor and the Chain Rule

If the sensitivity of the apparatus impedance to its parameters ρ is known, that is,

$$\Delta Z_{Ak}(\lambda) = \frac{\partial Z_{Ak}(\lambda)}{\partial \rho} \cdot \Delta \rho, \quad (3.24)$$

the *parameter participation factor* is further defined as

$$p_{\lambda, \rho} = \left\langle p_{\lambda, Z_{Ak}}, \frac{\partial Z_{Ak}(\lambda)}{\partial \rho} \right\rangle \quad (3.25)$$

such that

$$\Delta\lambda = p_{\lambda, \rho} \cdot \Delta \rho. \quad (3.26)$$

The value of parameter participation factor is of great importance because it delivers information on how to change the parameters to move λ in a desired direction on the complex plane. Thus the

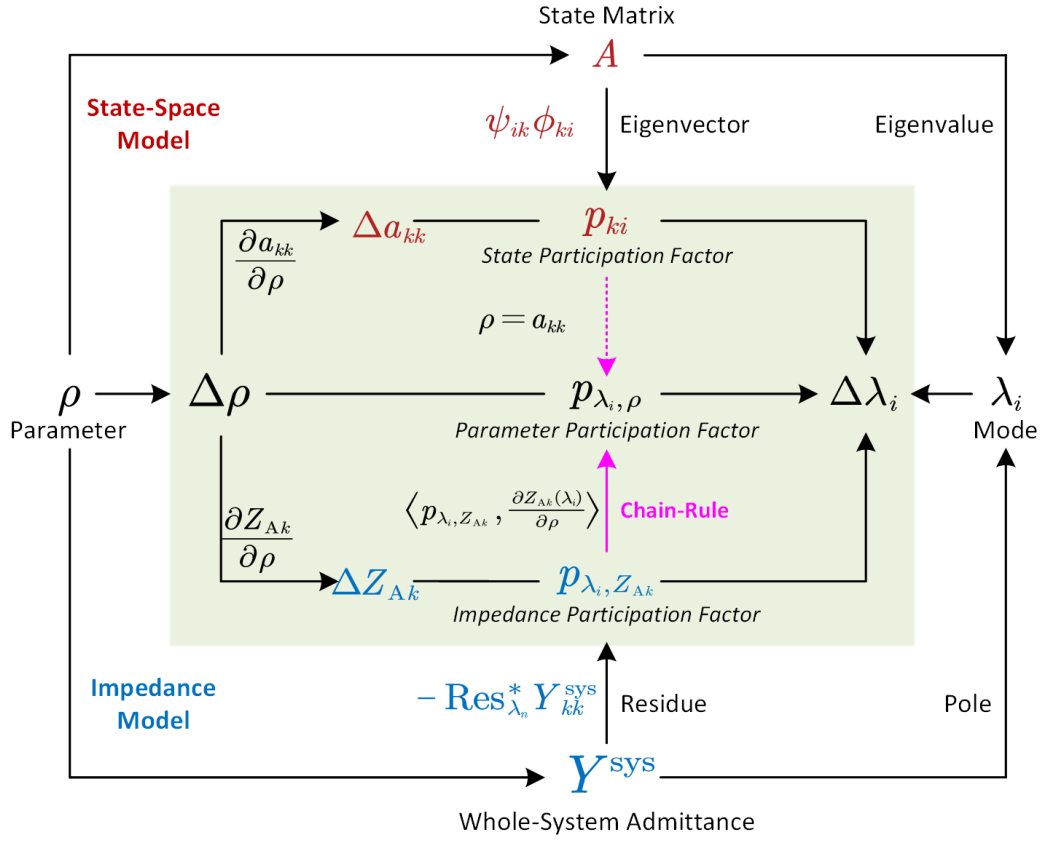


Figure 3.2: The relationship between impedance participation factor and state participation factor and the chain-rule for participation propagation.

parameter participation factor is directly useful in tuning the parameters to stabilise the system.

If, in a special case, the parameter ρ is selected as the k -th diagonal element a_{kk} in the state matrix A , the corresponding parameter participation factor is the state participation factor

$$p_{ki} = p_{\lambda_i, a_{kk}} = \left\langle p_{\lambda_i, Z_{Ak}}, \frac{\partial Z_{Ak}(\lambda_i)}{\partial a_{kk}} \right\rangle. \quad (3.27)$$

Thus we establish the relationship between the different types of participation factors and summarize this relationship in Fig. 3.2. In practice, the state coefficient a_{kk} might be the combination of multiple physical or control parameters and thus is not an independent parameter itself. As a result, a_{kk} is treated as a virtual parameter to establish the linkage between state and parameter participation factors, as marked by the dashed arrow in Fig. 3.2.

Equations (3.25) and (3.27) are described as the chain-rule of participation factors which is of profound importance in participation analysis. The impedance participation factor enables us to evaluate

the participation of an apparatus in system oscillations through only black-box models. On top of this, the chain-rule yields the state and parameter participation factors, further enabling us to look inside the black-box and trace root-causes to specific parameters and states without needing disclosure of the state equations.

3.3 Impedance-based Eigenvalue Sensitivity Theory

Comparing the impedance participation factor discussed above and the study of the previous RMA method reviewed in Chapter (3.1.1), several conclusions can be made. On the one hand, the impedance participation factor shows an advantage of giving the sensitivity of oscillatory mode λ , rather than the sensitivity of γ which lacks physical meaning. Further, through the use of the Frobenius inner product, a 2×2 matrix block in $d-q$ frame can be transformed into a single value which can be readily compared with values of terms. However, the off-diagonal elements of Z^{sys} and Y^{sys} have not been used and so this analysis does not yet extended to the whole network because series-connected apparatus in branches are not included. In contrast, a significant advantage of the previous RMA method is that the sensitivity of γ to elements in Y^{nodal} can be acquired, where individual terms such as Y_{ki}^{nodal} mapped to specific elements in the system including branches and so sensitivity results covering the whole network are available. Besides that advantage, the weaknesses of RMA listed in Chapter (3.1.1) remain and limit its practical application.

Considering the pros and cons of both impedance participation factors and critical admittance-eigenvalue sensitivity, a desire to combine their advantages motivates a search for solution of state-space eigenvalue sensitivity with respect to entries in Y^{nodal} , i.e., the value of $\frac{\partial \lambda}{\partial Y_{ki}^{\text{nodal}}}$.

3.3.1 State-Space Eigenvalue Sensitivity Derived from Impedance Model

To strictly evaluate how impedances of network components affect λ , the eigenvalue sensitivity $\frac{\partial \lambda}{\partial Y_{ki}^{\text{nodal}}}$ should be found. In a similar fashion to S_γ , we define the eigenvalue sensitivity matrix as S_λ , in which

the element in the i -th row k -th column is

$$S_{\lambda,ik} = \frac{\partial \lambda}{\partial Y_{ki}^{\text{nodal}}}. \quad (3.28)$$

Now we determine the value of $\frac{\partial \lambda}{\partial Y_{ki}^{\text{nodal}}}$. From section 2.3 we know that $Y_{\text{det}}^{\text{nodal}}(\lambda) = 0$. Based on this condition, the method of eigenvalue perturbation can be applied and the value of eigenvalue sensitivity matrix can be derived as

$$S_{\lambda} = -\frac{\text{adj}(Y^{\text{nodal}}(\lambda))}{Y_{\text{det}}^{\text{nodal}' }(\lambda)}. \quad (3.29)$$

The detailed proof of eigenvalue sensitivity matrix (3.29) is given in Appendix A.4, where $Y_{\text{det}}^{\text{nodal}' }$ is the derivative of $Y_{\text{det}}^{\text{nodal}}(s)$ at $s = \lambda$ defined in (A.30).

Equation (3.29) gives a direct method to calculate state-space eigenvalue sensitivity with respect to entries in Y^{nodal} . Compared with the sensitivity of critical admittance-eigenvalue S_{γ} , the result of S_{λ} offers more directly useful information about system oscillations because λ is an oscillatory mode of the system.

We now seek to establish the mathematical relationship between S_{λ} and S_{γ} . For a better illustration, three simple properties are introduced as below:

Property 3.2 *Let Y be an $n \times n$ matrix, the rank of Y is the number of non-zero eigenvalues of Y .*

Property 3.3 *Let Y be an $n \times n$ matrix, if $\text{rank}(Y) = n - 1$, then $\text{rank}(\text{adj}(Y)) = 1$. If $\text{rank}(Y) \leq n - 2$, then $\text{rank}(\text{adj}(Y)) = 0$, i.e., $\text{adj}(Y)$ is a zero matrix.*

Property 3.4 *Let Y be an $n \times n$ matrix, $\text{rank}(Y) = 1$ if and only if there exist two column vectors u_s and w_s of dimension n such that $Y = u_s w_s^{\top}$.*

In (3.29), it is clear that the term $Y_{\text{det}}^{\text{nodal}' }(\lambda)$ is a scalar while the term $\text{adj}(Y^{\text{nodal}}(\lambda))$ is a matrix. From section 3.1.1, it is known that λ is considered as a non-repeated eigenvalue and $Y^{\text{nodal}}(\lambda)$ has one and only one zero-valued eigenvalue plus $n - 1$ non-zero eigenvalues. According to property 3.2, the

rank of $Y^{\text{nodal}}(\lambda)$ is $n - 1$. Consequently, according to property 3.3, the rank of its adjunct matrix $\text{adj}(Y^{\text{nodal}}(\lambda))$ is 1. Combined with property 3.4, we have

$$\text{adj}(Y^{\text{nodal}}(\lambda)) = u_s \otimes w_s = u_s w_s^\top, \quad (3.30)$$

where u_s and w_s are two non-zero column-vectors of dimension n . An important finding is that equation (3.30) has the same format as (3.7), i.e., the outer product of two column vectors.

Through the proof in Appendix A.5, it can be shown that

$$\text{adj}(Y^{\text{nodal}}(\lambda)) = u_s w_s^\top = \text{tr}(\text{adj}(Y^{\text{nodal}}(\lambda))) \cdot u_\gamma w_\gamma^\top, \quad (3.31)$$

where u_γ and w_γ are the left and right eigenvectors of $Y^{\text{nodal}}(\lambda)$ corresponding to the critical admittance-eigenvalue γ . Combining (3.7),(3.29) and (3.31) yields

$$\begin{aligned} S_\lambda &= \xi \cdot S_\gamma = \xi u_\gamma w_\gamma^\top \\ \frac{\partial \lambda}{\partial Y_{ki}^{\text{nodal}}} &= \xi \cdot \frac{\partial \gamma}{\partial Y_{ki}^{\text{nodal}}} \end{aligned} \quad (3.32)$$

where ξ is a coefficient with a value of

$$\xi = -\frac{\text{tr}(\text{adj}(Y^{\text{nodal}}(\lambda)))}{Y_{\text{det}}^{\text{nodal}}(\lambda)}. \quad (3.33)$$

Equations (3.32) and (3.33) reveal the form of the relationship between critical admittance-eigenvalue sensitivity $\frac{\partial \gamma}{\partial Y_{ki}^{\text{nodal}}}$ and eigenvalue sensitivity $\frac{\partial \lambda}{\partial Y_{ki}^{\text{nodal}}}$: the two values differ by a coefficient ξ . Since the mode of interest, λ , is usually a conjugate complex pair, it is clear from (3.33) that ξ will accordingly be a conjugate complex pair, which contains directional information. By omitting ξ , the term $\frac{\partial \gamma}{\partial Y_{ki}^{\text{nodal}}}$ studied in the previous literature loses any meaning in terms of its direction in the complex plane and hence cannot reveal a components' influence on the σ and ω parts of λ as separate terms. As a result, components with relatively large magnitude of critical admittance-eigenvalue sensitivity may possibly, but not necessarily, affect the λ -mode. In contrast, the eigenvalue sensitivity $\frac{\partial \lambda}{\partial Y_{ki}^{\text{nodal}}}$ not only preserves the advantage of locational information, but also precisely shows how component

admittance affects the mode in both damping and natural frequency.

3.3.2 Comprehensive Theory for Root-cause Analysis

To compute the value of $\frac{\partial \lambda}{\partial Y_{ki}^{\text{nodal}}}$, it is straightforward to apply (3.29) or (3.32). However, as mentioned before, the elements in Y^{nodal} cannot be measured readily online because small-signal voltage perturbations cannot be injected in parallel with stiff voltage sources. If impedance models are also not available from apparatus vendors, or do not account for operating point variation, then practical application of eigenvalue sensitivity in the nodal admittance model may not be possible. On the other hand, Z^{sys} can be measured online, and the residues of the diagonal-elements in Z^{sys} can lead to the admittance participation factor of shunt-connected components. This observation lead us to explore the relationship between eigenvalue sensitivity and the residues of Z^{sys} .

From equation (A.22) in Appendix A.3, it is clear that

$$\text{Res}_\lambda Z^{\text{sys}} = \frac{\text{adj}(Y^{\text{nodal}}(\lambda))}{Y_{\det}^{\text{nodal}'}(\lambda)}, \quad (3.34)$$

Combining (3.29) and (3.34) yields

$$\begin{aligned} S_\lambda &= -\text{Res}_\lambda Z^{\text{sys}} \\ S_{\lambda,ik} &= \frac{\partial \lambda}{\partial Y_{ki}^{\text{nodal}}} = -\text{Res}_\lambda Z_{ki}^{\text{sys}} \end{aligned} \quad (3.35)$$

The finding in equation (3.35) indicates a practical route for determining the sensitivity, because the spectra of the entries in Z^{sys} can be measured online, and the poles and residues can be identified from the spectra by vector fitting techniques [57]. This method also provides useful flexibility for comparing sensitivities where only some specific elements in S_λ need to be compared. A system operator could choose to partially measure Z^{sys} , that is, the relevant elements of the matrix only, rather than acquiring the full matrix of the networked impedance model. Such flexibility cannot be achieved in equations (3.29) or (3.32).

Based on equation (3.35), eigenvalue sensitivity analysis can be implemented for the whole network

and provide access to the state-space eigenvalue sensitivities with respect to the admittance of any component in the system. An example will be used to illustrate the point, and only single phase is considered for simplicity but the frame will be extended to d - q frame later. Considering an apparatus with admittance of y , its internal parameter ρ is perturbed by a small value $\Delta\rho$ so leading to a perturbation of its admittance Δy . Consequently, such perturbation will add a small change on elements in nodal admittance model, i.e., for each element in Y^{nodal} the perturbation is

$$\Delta Y_{ki}^{\text{nodal}} = \frac{\partial Y_{ki}^{\text{nodal}}}{\partial y} \cdot \Delta y. \quad (3.36)$$

Because a diagonal entry of Y^{nodal} represent all admittances terminating at that node whereas the off-diagonal entry is the negative of the sum of admittances between two nodes, the changes in Y^{nodal} can be divided into two cases: when y is a shunt-connected component or when it is a branch-connected component in the system, such that

$$\Delta Y^{\text{nodal}} \begin{cases} \Delta Y_{kk}^{\text{nodal}} = \Delta y \\ \text{otherelements} = 0 \end{cases}, \text{ shunt-connected } y \text{ at node-}k, \text{ or} \quad (3.37)$$

$$\Delta Y^{\text{nodal}} \begin{cases} \Delta Y_{kk}^{\text{nodal}} = \Delta Y_{ii}^{\text{nodal}} = \Delta y \\ \Delta Y_{ki}^{\text{nodal}} = \Delta Y_{ik}^{\text{nodal}} = -\Delta y \\ \text{other elements} = 0 \end{cases}, \text{ branch-connected } y \text{ at branch-}ki$$

Eventually, a small variation will be added to the oscillatory mode as

$$\Delta\lambda = \sum_{k=1}^n \sum_{i=1}^n \left(\frac{\partial\lambda}{\partial Y_{ki}^{\text{nodal}}} \Delta Y_{ki}^{\text{nodal}} \right) \quad (3.38)$$

Combining with (3.37) yields

$$\Delta\lambda = \begin{cases} \frac{\partial\lambda}{\partial Y_{kk}^{\text{nodal}}} \Delta y, \text{ shunt-connected } y \text{ at node-}k \\ \left(\frac{\partial\lambda}{\partial Y_{kk}^{\text{nodal}}} + \frac{\partial\lambda}{\partial Y_{ii}^{\text{nodal}}} - \frac{\partial\lambda}{\partial Y_{ki}^{\text{nodal}}} - \frac{\partial\lambda}{\partial Y_{ik}^{\text{nodal}}} \right) \Delta y, \text{ branch-connected } y \text{ at branch-}ki \end{cases} \quad (3.39)$$

Combining (3.39) and (3.35) and rearranging the expressions yields to a general expression on the

eigenvalue sensitivity with respect to admittance of a specific component in the system:

$$\frac{\partial \lambda}{\partial y} = \sum_{k,i}^n \left(\frac{\partial \lambda}{\partial Y_{ki}^{\text{nodal}}} \frac{\partial Y_{ki}^{\text{nodal}}}{\partial y} \right) = -\text{tr} \left(\text{Res}_\lambda Z^{\text{sys}} \cdot \frac{\partial Y^{\text{nodal}}}{\partial y} \right). \quad (3.40)$$

For instant,

$$\frac{\partial \lambda}{\partial y} = \begin{cases} -\text{Res}_\lambda Z_{kk}^{\text{sys}} & \text{shunt-connected } y \text{ at node-}k \\ \begin{pmatrix} -\text{Res}_\lambda Z_{kk}^{\text{sys}} - \text{Res}_\lambda Z_{ii}^{\text{sys}} \\ +\text{Res}_\lambda Z_{ki}^{\text{sys}} + \text{Res}_\lambda Z_{ik}^{\text{sys}} \end{pmatrix} & \text{branch-connected } y \text{ as branch-}ki. \end{cases}$$

It can also be seen that when y is a shunt-connected component, the above sensitivity is equivalent to the admittance participation factor defined in (3.22), hence the two definitions can be merged together into S_λ and forms a general approach for root-cause analysis, which also extends eigenvalue sensitivity to d - q frame. For a component with admittance y in the system, we define the *admittance sensitivity factor* as

$$s_{\lambda,y} = -\text{tr} \left(\text{Res}_\lambda Z^{\text{sys}} \cdot \frac{\partial Y^{\text{nodal}}}{\partial y} \right)^*, \quad (3.41)$$

such that

$$\Delta \lambda = \langle s_{\lambda,y}, \Delta y(\lambda) \rangle. \quad (3.42)$$

If the sensitivity of y with respect to a parameter of a component ρ is further known, i.e., $\frac{\partial y}{\partial \rho}$, from the chain rule described in Chapter 3.2.2, we define the *parameter sensitivity factor* as

$$s_{\lambda,\rho} = \left\langle s_{\lambda,y}, \frac{\partial y(\lambda)}{\partial \rho} \right\rangle \quad (3.43)$$

such that

$$\Delta \lambda = s_{\lambda,\rho} \cdot \Delta \rho. \quad (3.44)$$

It is also worth mentioning that the eigenvalue sensitivity approach above is suitable for whole-system impedance model Z^{sys} but not for whole-system admittance model Y^{sys} because the entries of $(Y^{\text{sys}})^{-1}$, as mentioned in equation (2.22), does not preserve locational information. As a result, the application of Y^{sys} is restricted to impedance participation factor analysis and cannot be extended

to a whole-system sensitivity analysis as is possible with Z^{sys} . Nevertheless, Y^{sys} is still quite useful when only voltage injections are available in the system.

Based on principles described above, a comprehensive theory of root-cause analysis in impedance models is set out in Fig. 3.3 The figure offers step-by-step guidance on how to extract participation factors and sensitivity information from impedance models, either using measurement data or using disclosed models. After acquiring the impedance participation factor and parameter participation factor, or alternatively admittance sensitivity factor and parameter sensitivity factor, a systematic analysis approach can be developed to determine the participants in oscillations, the root-cause of the poor-damping, and the most effective parameter to adjust to stabilise the system. This newly developed approach has been named the *the Grey-box Approach* and it will be discussed further in the next section.

3.4 The Grey-box Approach

The grey-box approach contains three layers with different transparencies according to the available prior knowledge, as illustrated in Fig. 3.4. The higher the transparency, the more prior knowledge is needed but along with that comes more useful information for root-cause tracing and trouble-shooting in whole-system stability analysis. As mentioned in (3.41), the participation factors can be merged with eigenvalue sensitivity so that only applications on the eigenvalue sensitivity analysis is shown in Fig. 3.4 and discussed in the following parts of this section. Each layer will be described in detail and the relationships between them will be revealed.

3.4.1 Grey-Box Layer-1

In this first layer, the information that needs to be available is the admittance y of apparatus along with the admittance sensitivity factors derived from impedance-based eigenvalue sensitivity matrix S_λ .

Due to the three-wire, three-phase nature of power systems, y and $s_{\lambda,y}$ are 2×2 matrix blocks in the

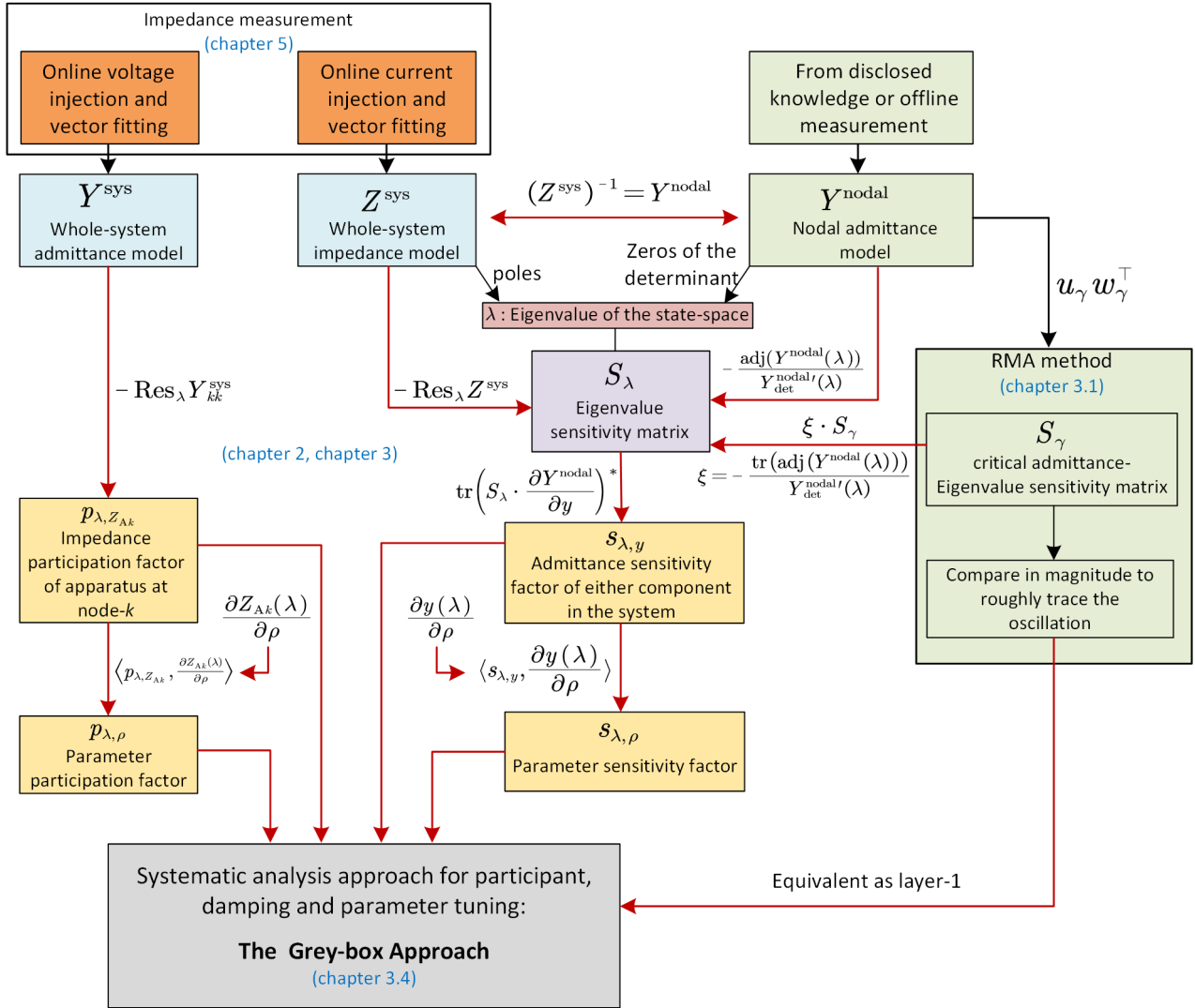


Figure 3.3: Illustration of the theory for root-cause analysis in impedance models. The blocks in golden, purple and grey, as well as all the arrows in red are developed in this thesis. The noise analysis process for impedance measurement (the orange blocks) is also developed in this thesis as given in Chapter 5. The green blocks refer to the RMA method proposed previously and reviewed in Chapter 3.1.1

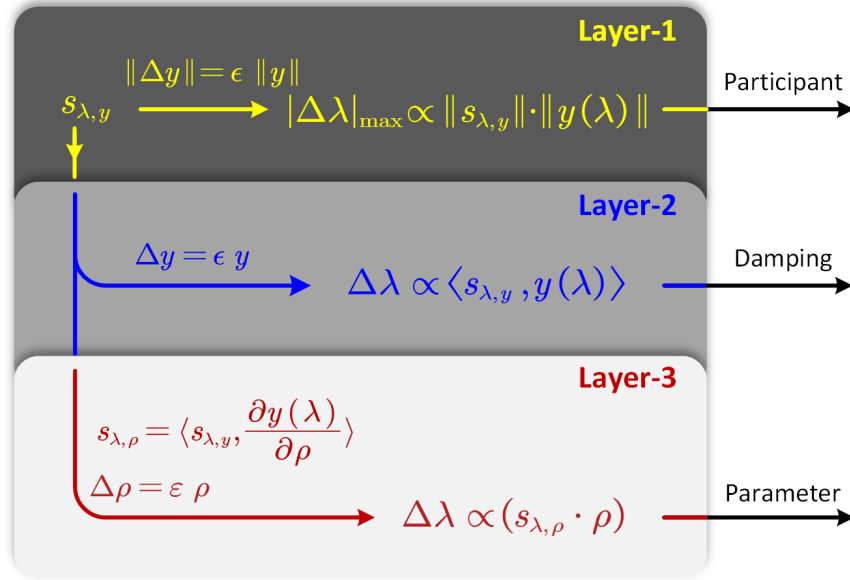


Figure 3.4: Illustration of the three-layer grey-box. In Layer-1, estimates of the potential participants are created based on the upper bound of $\Delta\lambda$ subject to $\|\Delta y\| = \epsilon \|y\|$. In Layer-2, the contribution of a participant to mode damping is estimated based on the real part of $\Delta\lambda$ subject to $\Delta y = \epsilon y$. In Layer-3, the most effective parameter within the participating apparatus is identified, and parameter re-tuning facilitated, via the admittance-parameter sensitivity.

synchronous d - q frame. A scalar index is needed to represent the four elements of $s_{\lambda,y}$ collectively so that $s_{\lambda,y}$ of different components can be compared and the location of the dominant apparatus (for a given mode) can be determined. To this end, we assign a consistent magnitude perturbation to each y and observe the effect on the eigenvalue λ . The perturbation is normalized to $\|y\|$ so that it scales with the corresponding apparatus, that is, $\|\Delta y\| = \epsilon \|y\|$, where ϵ is a small positive constant. According to the Cauchy inequality, we have

$$|\Delta\lambda| = |\langle s_{\lambda,y}, \Delta y(\lambda) \rangle| \leq \|s_{\lambda,y}\| \cdot \|\Delta y(\lambda)\| \quad (3.45)$$

which yields

$$|\Delta\lambda|_{\max} = \|s_{\lambda,y}\| \cdot \|\Delta y(\lambda)\| = \epsilon \|s_{\lambda,y}\| \cdot \|y(\lambda)\|. \quad (3.46)$$

It is clear from (3.46) that $\|s_{\lambda,y}\| \cdot \|y(\lambda)\|$ determines the upper bound of $\Delta\lambda$, $|\Delta\lambda|_{\max}$, which is the maximum possible participation of the corresponding apparatus. Only apparatus with relatively large $|\Delta\lambda|_{\max}$ may possibly, but not necessarily, participate in the λ -mode. Thus, we use $\|s_{\lambda,y}\| \cdot \|Z_{Ak}(\lambda)\|$ as the primary participation index in Layer-1 of the grey-box approach. Layer-1 roughly identifies

potential participants in a mode and does so with black-box models only.

3.4.2 Grey-Box Layer-2

Building on Layer-1, Layer-2 adds a stipulation that the perturbation of apparatus admittance Δy is aligned to the original admittance y , that is, $\Delta y = \epsilon y$, where ϵ is a very small positive real number. This is a reasonable stipulation because it emulates the effect of scaling up or down an apparatus so the resulting impedance shrinks or grows in amplitude but maintains the same angle. The scaling can be done by changing the base power of an apparatus with per-unit parameters, or by connecting or disconnecting a portion of apparatus from a farm of identical apparatus (e.g. a wind farm). Layer-2 does not require extra information to Layer-1 but adds to Layer-1 by the extra stipulation on the orientation of Δy , which yields the direction of $\Delta \lambda$ and thus brings additional knowledge about the node's impact on system damping:

$$\Delta \lambda = \langle s_{\lambda,y}, \Delta y(\lambda) \rangle = \epsilon \langle s_{\lambda,y}, y(\lambda) \rangle. \quad (3.47)$$

From (3.47) we see that $\Delta \lambda$ is determined by $\langle s_{\lambda,y}, y(\lambda) \rangle$ which we use as the new participation index for Layer-2. If the real-part of $\langle s_{\lambda,y}, y(\lambda) \rangle$ is positive, it implies that scaling up the corresponding apparatus connected at the node tends to shift the mode rightwards in the complex plane, and will make the system be more unstable.

3.4.3 Grey-Box Layer-3

The final layer of the grey-box approach aims to look into the participating components in order to identify which physical parameter in the component is the root-cause of instability, and thus provide indication of which parameter should be re-tuned, and how to re-tune it, to stabilize the system.

Layer-3 requires additional information in the form of the partial derivative of a component's admittance to its internal parameters, $\partial y / \partial \rho$, so that a parameter perturbation is propagated to an impedance perturbation and further into an eigenvalue perturbation via the chain-rule (see section 3.2.2). This

additional information can be provided by the apparatus vendor to the SO, or the SO could pass the result of $s_{\lambda,y}$ to the vendor as a reference for tuning. The chain-rule yields the parameter sensitivity factors $s_{\lambda,\rho}$ using (3.43). It is also worth mentioning that each parameter has a unit of its own (such as ohm or hertz) or is dimensionless (such as a gain), so that it is not reasonable to compare $s_{\lambda,\rho}$ of all parameters directly. To this end, perturbations should be of a consistent proportion to the original parameter ρ , i.e. $\Delta\rho = \epsilon\rho$, where ϵ is a small positive constant. Substituting $\Delta\rho$ to (3.44) yields

$$\Delta\lambda = \epsilon(s_{\lambda,\rho} \cdot \rho). \quad (3.48)$$

If the real part of $(s_{\lambda,\rho} \cdot \rho)$ is large and negative, it implies that by increasing this parameter, the mode can be shifted leftwards on the complex plane, i.e., the system would become more stable. By plotting all $(s_{\lambda,\rho} \cdot \rho)$ on the complex plane, clear indication would be provided of how to tune (increase or decrease) the parameters to shift the mode in a desired direction, either to alter the damping or alter the natural frequency. This is a great advantage of the Layer-3 grey-box approach that is not available from other impedance model methods. The required additional information to achieve this benefit, $\partial y/\partial\rho$, discloses little information regarding the internal design details or control algorithm of the apparatus thus still preserves most of the advantages to apparatus vendors of a black-box model.

3.5 Practical Implementation

This section discusses the detailed implementation of the grey-box approach in practical applications. From Fig. 3.4, it can be seen that three sets of data are required by the grey-box approach, namely, y , $s_{\lambda,y}$, and, for Layer-3 only, $\partial y/\partial\rho$.

There are two routes to obtain y , the admittance of a component (apparatus) in the system:

1) Model-based route.

This route is relevant to vendors who have available detailed analytical models that preserve all the states. Differential equations can be derived from such models and can be linearised around an operating point to obtain state-space matrices. The state-space matrices are then transformed

into transfer functions. This route is used for the 14-bus and 68-bus case studies in this thesis. It is also worth noting that, as pointed in Chapter 1.2.2, the admittance of an apparatus may vary according to different operating points. As a result, the underlying relationship between admittance spectrum and operating points needs to be established, or spectra at some critical operating points should be given and spectra at other points can be estimated from the available knowledge [61]. This topic is still being studied.

2) Measurement-Based route.

This route can be fulfilled either by vendors or by system operators. Before connecting the apparatus to the power system, the vendors can connect it to a known system, such as a constant power load or a grid emulator [56]. By adding small-signal voltage perturbations at the PCC and measure the current response, the series-connected admittance of the apparatus y and the known system y_0 can be acquired, i.e., $(y^{-1} + y_0^{-1})^{-1}$, from which y can be restored. After the apparatus connected to the power system, the system operator can add voltage perturbations in series with the apparatus and measure the current response, such that the diagonal element of Y^{sys} can be measured. In the meantime, by measuring the voltage response distributed on the apparatus and taking it as the input, and measuring the current response as the output, the apparatus admittance y can also be acquired. This route avoids the complicated handwritten differential equations and can be fulfilled online regardless of operating points, but the drawback is that the measurement can be sensitive to noise. The issues related to noise are later discussed in Chapter 5.

The value of $s_{\lambda,y}$, which is obtained from (3.40), relies on the knowledge of Z^{sys} and again there are two routes of acquiring it:

1) Assembly route.

This route relies on the knowledge of y , which is discussed right above. After having admittance of all apparatus, the admittance matrix Y_A can be acquired based on the definition given in (2.9), which can further yields Z_A from an inverse calculation. Combining with the nodal admittance matrix Y_N which is usually known by the system operator, Z^{sys} can be assembled using (2.18).

2) Measurement route.

This route is based on the definition of Z^{sys} in (2.16), but to transformed the virtual injections used for understanding into real small-signal injections. Such method can give useful information without knowing any of the details of the system. However, for off-diagonal elements of Z^{sys} , the measurement requires injection at one node and taking the response at the other node. When the two nodes are far from each other, the perturbation signal can be significantly attenuated and buried in the noise. So far, this route can only be applied theoretically, and is considered as future work of this thesis. Nevertheless, the diagonal elements of Z^{sys} , which can be used to assess the participation factors of shunt-connected components, are considered to be measurable because both the injection and the response measurement are performed at the same node.

The value $\partial y / \partial \rho$ is available from vendors. If the symbolic transfer function of the apparatus is established, $\partial y / \partial \rho$ can be calculated in a symbolic manner, after which the value can be acquired by substituting all the parameter values. Such method is applied in the 3-node case study in this thesis. Another method is to add a small perturbation upon the parameter ρ and assess the changes on y , such that

$$\frac{\partial y}{\partial \rho} \approx \frac{y_{\rho+\Delta\rho} - y}{\Delta\rho}, \quad (3.49)$$

where $\Delta\rho$ is a small perturbation and $y_{\rho+\Delta\rho}$ is the admittance under the effect of the perturbation. This method is applied in the 14-bus and 68-bus case studies in this thesis. The value of $\Delta\rho$ can be selected as $\Delta\rho = 10^{-5}(1 + |\rho|)$ following [99] as a trade-off between the relative and absolute definitions of perturbation.

3.6 Summary

This chapter for the first time provides a means to calculate the value of state-space eigenvalue sensitivity and impedance participation factor in impedance models, and establishes a comprehensive theory for root-cause analysis in impedance models. The three-layer grey-box approach is also invented which, for large power systems for which only impedance models of apparatus are available,

provides a systematic method of analysis of small-signal stability, participation analysis and guidance for parameter tuning. The proposed grey-box approach is based on rigorous mathematical analysis with proof of the relationship between the residue of a pole and the impedance participation factor, and elucidation of the chain-rule of sensitivity propagation of internal states and parameters forward to the impedance participation factor. It thus provides a unified participation theory between state-space and impedance models. Discussions on the practical implementation of the grey-box approach is also included in this chapter.

Chapter 4

Case Studies: Applications of the Grey-box

Approach

Three case studies, from a simple circuit to a large-scale composite grid, are examined to demonstrate the validity of the theoretical basis of the proposed impedance-based root-cause analysis, including the effectiveness of the grey-box approach. The case studies have been presented in the author's paper [95, 96] and some figures and sentences are repeated. The system data, the codes used to generate the simulation results, and all numerical results are available at: <https://github.com/Future-Power-Networks/Publications> [100] through an open-source license.

4.1 Three-node Passive Circuit

A single-phase 3-node passive circuit, as shown in Fig. 4.1, is established to demonstrate the advantages of eigenvalue sensitivity analysis in the networked impedance models and to draw a comparison with critical admittance-eigenvalue sensitivity. The nodal admittance model Y^{nodal} is established as

$$Y^{\text{nodal}} = \begin{bmatrix} y_{11}+y_{12}+y_{13} & -y_{12} & -y_{13} \\ -y_{12} & y_{22}+y_{12}+y_{23} & -y_{23} \\ -y_{13} & -y_{23} & y_{33}+y_{23}+y_{13} \end{bmatrix}, \quad (4.1)$$

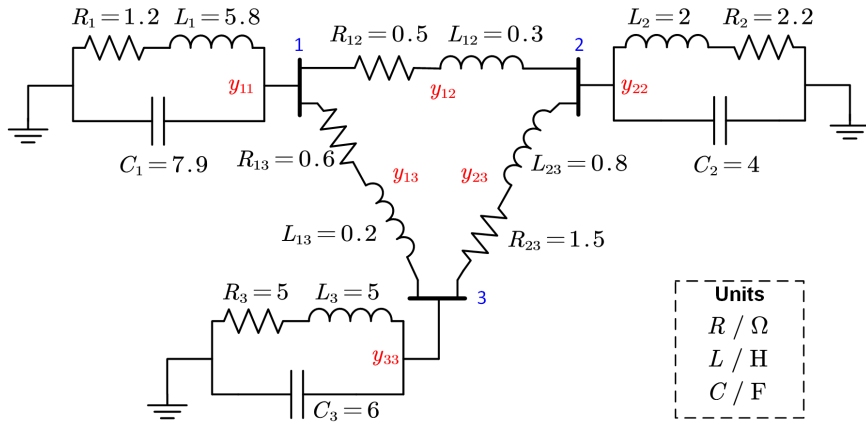


Figure 4.1: 3-node simple passive circuit.

where y_{ik} is an admittance of the components form a branch (composed of R and L or a shunt admittance a at a node in the system (composed of R and L in parallel with C), that is,

$$y_{ik} = \begin{cases} (R_i + sL_i)^{-1} + sC_i & i = k \\ (R_{ik} + sL_{ik})^{-1} & i \neq k \end{cases}. \quad (4.2)$$

By calculating the zeros of Y_{\det}^{sys} , we identify 9 eigenvalues for the whole system of which 6 form complex conjugate pairs and all are in the left half-plane. Since the complex eigenvalues represent oscillatory modes, we choose the three pairs of complex conjugate eigenvalues for further analysis. For each selected eigenvalue, a corresponding coefficient ξ can be calculated from (3.33), which defines the relationship between critical admittance-eigenvalue sensitivity and eigenvalue sensitivity. Because of the repeated information in a conjugate pair, we only consider the values at the upper half-plane, i.e.,

$$\begin{aligned} \lambda_1 &= -0.837 + j0.968 \text{ rad/s}, & \xi_1 &= -0.109 + j0.094 \\ \lambda_2 &= -0.945 + j0.270 \text{ rad/s}, & \xi_2 &= -0.167 + j0.096 \\ \lambda_3 &= -0.130 + j0.045 \text{ rad/s}, & \xi_3 &= -0.082 + j0.192. \end{aligned} \quad (4.3)$$

For each of the three eigenvalues, we identify the two components which have the largest affect on the mode characteristic as noted in the first column of Table 4.1. The third column shows the critical admittance-eigenvalue sensitivity in magnitude form (Layer-1 of the grey-box), $|\frac{\partial \gamma}{\partial y}| |y|$. The

Table 4.1: critical admittance-eigenvalue sensitivity and eigenvalue sensitivity for selected components in the grey-box layer 1, 2

Mode, component	Critical admittance-eigenvalue		State-space eigenvalue		
	$\frac{\partial \gamma}{\partial y}$	$ \frac{\partial \gamma}{\partial y} y $	$s_{\lambda,y}$	$\langle s_{\lambda,y} , y \rangle$	$\langle s_{\lambda,y}, y \rangle$
λ_1, y_{12}	1.747+j0.101	4.576	-0.201-j0.152	0.659	-0.036+j0.658
λ_1, y_2	0.848-j0.044	3.969	-0.089-j0.084	0.571	-0.001-j0.571
λ_2, y_{13}	1.6981-j0.102	4.103	-0.273-j0.179	0.788	-0.597+j0.515
λ_2, y_3	0.679-j0.026	3.802	-0.111-j0.069	0.730	0.548-j0.483
λ_3, y_1	0.256+j0.053	0.232	-0.031-j0.045	0.048	0.008+j0.048
λ_3, y_3	0.442-j0.053	0.270	-0.026-j0.089	0.056	-0.009-j0.056

penultimate column is the eigenvalue sensitivity in magnitude form, $\langle |s_{\lambda,y}|, |y| \rangle$. Comparing these two columns, one can see that there is a fixed scalar relationship between them and they therefore contain the same information and both roughly indicate the participation of the components in the modes. However, examining the vector form of the quantities, $\frac{\partial \gamma}{\partial y}$ has a different ratio between the real-part and imaginary-part of the sensitivity than $s_{\lambda,y}$, in other words, a different angle. This illustrates the conclusions in Chapter 3.3.1 that the critical admittance-eigenvalue sensitivity does not give an indication of how a change in component value will affect damping and frequency of a mode. The result in the final column, $\langle s_{\lambda,y}, y \rangle$ (layer-2 of the grey-box) does give guidance on how to stabilise the system by tuning the admittance by scaling-up or scaling down the the value (aligned to its original direction). For instance, by increasing y_{12} proportionally (scaling up), λ_1 will shift to up and to the left such that both the damping and natural frequency will increase.

Considering (4.2), providing information on $\frac{\partial y}{\partial \rho}$, where ρ is a parameter (R, L, C), allows computation of layer-3 of the grey-box, as illustrated in Table 4.2. Results are shown for some selected parameters which are influential on λ . Parameter sensitivity factors $s_{\lambda,\rho}$ are calculated from (3.43), and a predicted change in eigenvalue $\Delta \lambda_{pr}$ is calculated and shown in third column for a 5% increment of a parameter based on

$$\Delta \lambda_{pr} = s_{\lambda,\rho} \cdot \rho \cdot 5\%. \quad (4.4)$$

For comparison, the eigenvalues of the system are re-computed for a 5% increment in parameter and the actual change in value from the original condition is shown in the fourth column as $\Delta \lambda$. The error

Table 4.2: Parameter sensitivity in the grey-box layer 3 and tuning results under 5% increment

Mode, parameter	$s_{\lambda,\rho} \cdot \rho$	Predicted $\Delta\lambda_{pr}$	Actual $\Delta\lambda$	Error
λ_1, R_{12}	-0.619-j0.598	-0.031-j0.030	-0.030-j0.031	3.63%
λ_1, L_{12}	0.658-j0.059	0.033-j0.003	0.031-j0.004	4.95%
λ_1, C_2	-0.030-j0.625	-0.001-j0.031	-0.002-j0.030	3.47%
λ_2, R_{13}	0.759-j0.851	0.038-j0.043	0.035-j0.038	10.43%
λ_2, R_3	-0.340+j0.053	-0.017+j0.003	-0.017+j0.001	7.64%
λ_2, C_3	0.515-j0.572	0.0260-j0.029	0.024-j0.027	5.67%
λ_3, R_1	-0.105-j0.219	-0.005-j0.011	-0.005-j0.013	18.42%
λ_3, L_1	0.114+j0.114	0.006+j0.006	0.005+j0.005	11.23%
λ_3, C_3	-0.004-j0.076	0.000-j0.004	0.000-j0.004	3.84%

between the predicted and actual values, in the fifth column, were calculated as

$$\text{error} = \frac{|\Delta\lambda_{pr} - \Delta\lambda|}{|\Delta\lambda_{pr}|}. \quad (4.5)$$

It is clear from Table 4.2 that the whole-system sensitivity analysis provides a useful prediction of the changes of eigenvalues by tuning specific parameters. The predictions are not perfect because the impedance model is based on a linearised small-signal model (linearised around the steady-state operating point) and therefore will not be fully accurate for substantial changes of parameter but when the perturbation is small, the error will be small also. It can be seen that under a 5% perturbation, the errors are within 20%, and all changes are in the correct direction. With such predictions available, a system operator can choose the most effective parameters to increase or decrease in a small range, in order to move eigenvalues in the desired direction and adjust either damping or natural frequency or both. If the parameters need to be adjusted over a large range, the grey-box approach would need to be applied iteratively over the path of parameter variations. The case of $\langle |s_{\lambda_3}|, |y_3| \rangle$ illustrates an important further point. The value seen in Table 4.1 is of reasonable magnitude but when looking at the effect of individual parameters in the last line of Table 4.2 we observe that it is not possible to change the damping (real part) of λ_3 by adjusting C_3 , proving the conclusion that Layer-1 can only roughly identify the means to re-tune a mode.

As a further illustration, parameters were swept from 100% to 105% (one at a time with other param-

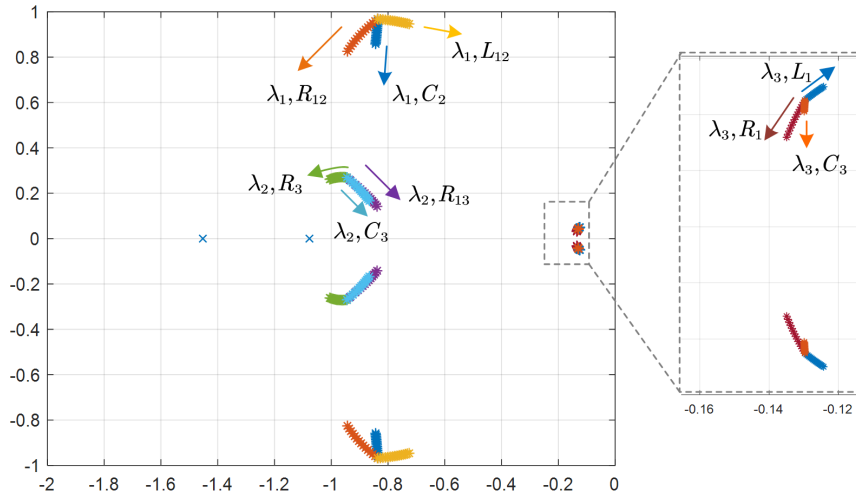


Figure 4.2: Eigenvalue plot of the system when parameters are swept from 100% to 105% respectively.

eters constant) and the eigenvalues calculated at each point, Fig. 4.2. It can be clearly seen that the changes of eigenvalues, both in direction and magnitude, match with results in Table 4.1, proving the correctness of the sensitive analysis.

4.2 Modified IEEE 14-bus System

We now demonstrate the use of sensitivity analysis on a three-phase power system with a mixture of inverters and conventional generators. The case study is based on the IEEE 14-bus network [101], with three additional IBRs (Type-IV wind farms) connected to buses 11, 12, 13, as shown in Fig. 4.3. The detailed parameters and the control of grid-following inverters are shown in Appendix D.1. The vector fitting process is also demonstrated in this case study.

The whole-system impedance spectra of the network, constructed from the admittance of all apparatus and grid impedances, are displayed in the Bode plot in Fig. 4.4. Because this is a three-phase power system modelled in the synchronous d - q frame, the whole-system admittance Z_{kk}^{sys} at each node is a 2×2 matrix. Only one of the four elements in the matrix (the d - d term) is displayed since that is sufficient to illustrate the characteristics of the system. Only nodes with sources (SGs or IBRs) present are plotted because the other nodes are passive. A significant peak is observed at 18.87 Hz at all nodes, meaning that the system has an oscillatory mode of 18.87 Hz. We choose this mode for

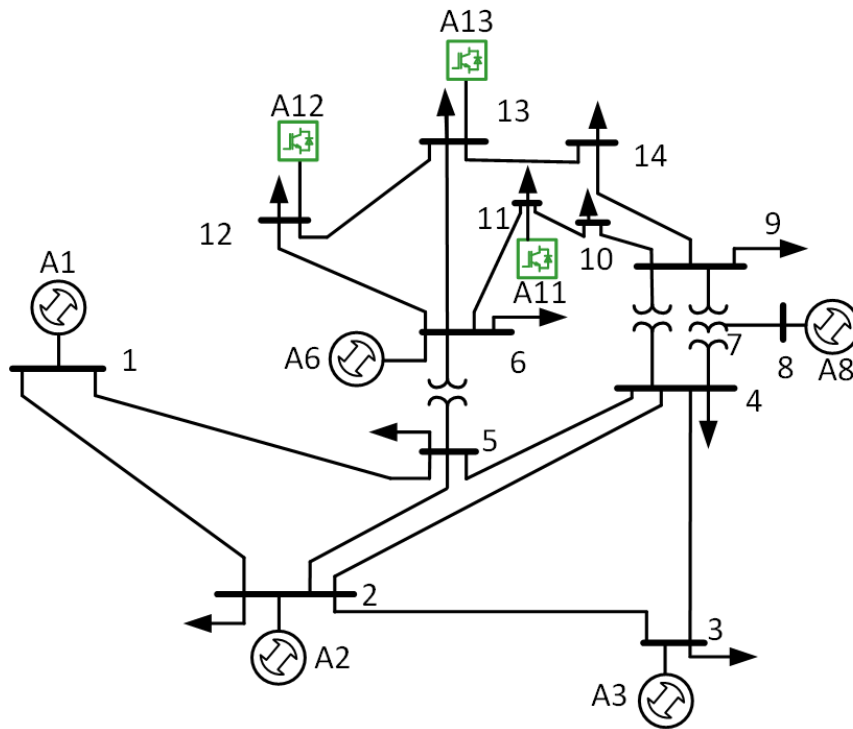


Figure 4.3: Modified IEEE-14 bus system with 3 extra IBRs.

sensitivity analysis.

Fig. 4.5 shows the results from the grey-box approach layer-1 and layer-2. It can be seen that nodes 6, 11, 12, 13, branches 5-6, 6-12, 6-13 stand out in the layer-1 pie chart. This indicates that the oscillation is mainly affected by these components. Breakdown of the sensitivity into real and imaginary parts in layer-2 reveals that node 6 and branch 5-6 have negative real parts and node 11, 12, 13 have positive real parts. This indicates that by increasing (scaling up) the admittance of node 6 and branch 5-6, the mode will shift leftwards in the complex plane, i.e., the damping will increase. On the other hand, by scaling up the apparatus admittance at nodes 11, 12, 13, the oscillation will be further exacerbated through reduced damping. Further to the results in layer-1, layer-2 goes on to indicate that for scaling-up of admittance, node 6 and branch 5-6 provide positive damping of the mode, while node 11, 12, 13 provide negative damping. In practical terms, scaling up of the admittance of a windfarm could be achieved by increasing the number of individual turbines operating.

Fig. 4.6 maps the influences on the 18.87 Hz mode as either increasing or decreasing damping for an impedance scale-up. It can be seen that damping is reduced by A11, A12 and A13, and increased by A6 and branch 5-6. Further, the main influences and participation in the mode is the upper part of the

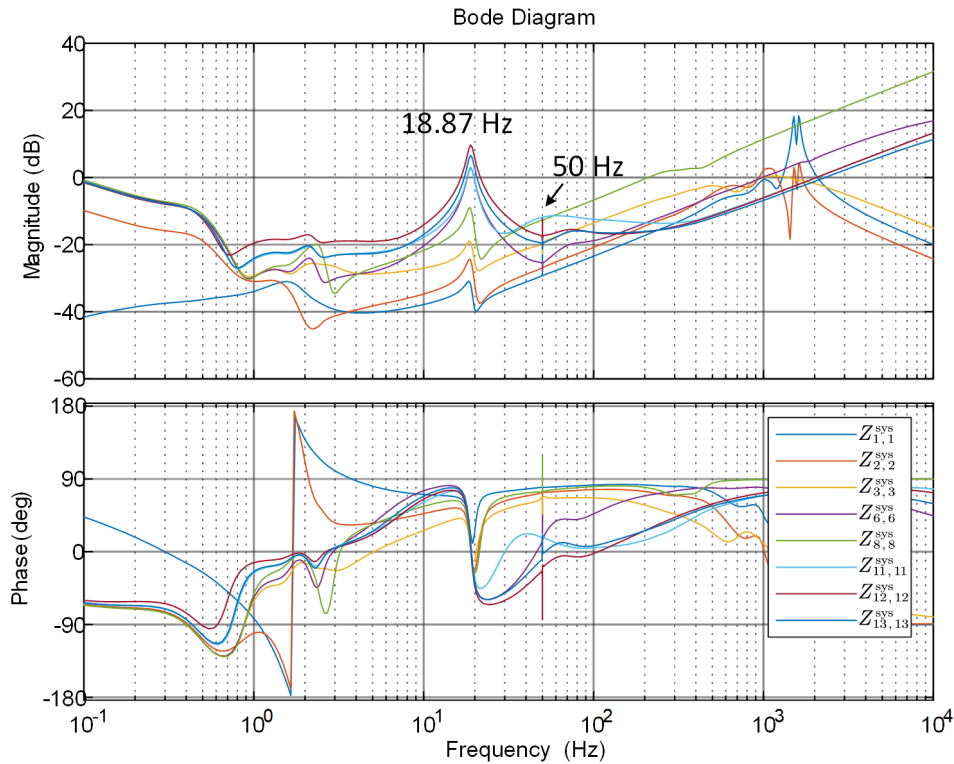


Figure 4.4: Bode diagram of whole system impedance Z_{kk}^{sys} at nodes with sources, presented in $d-d$ axis.

network with branch 5-6 acting as a boundary.

By applying layer-3 of the grey-box, the parameters within A11, A12 and A13 with the greatest influence on the mode can be identified as candidates for tuning. The results are shown in Table 4.3. It can be seen that the current control bandwidths f_i of the three IBRs are most influential and have a large negative value for the real part of the sensitivity. We can conclude that the low damping of the 18.87 Hz mode is mainly caused by the current control bandwidth of A11, A12 and A13 having been set too low. Typically, the current control bandwidth of a grid-following inverter is limited around 500 Hz [102], and cannot be set too high or too low. A high control bandwidth can make the current controller very sensitive to noise and introduces instability, while a low control bandwidth makes the inner current loop interact with outer PLL loop which also leads to instability [103]. Layer-3 has narrowed down the root cause of the oscillation to specific parameters in a way that layers 1 and 2 and critical admittance-eigenvalue sensitivity can not. To stabilise the system, we choose to increase f_i of the three IBRs by 20%, 50% and 28.5% for A11, A12 and A13 respectively which will shift the pole leftwards. Fig. 4.7 (a) shows the Bode plot of $Z_{12,12}^{\text{sys}}$ before and after tuning. It can be seen that

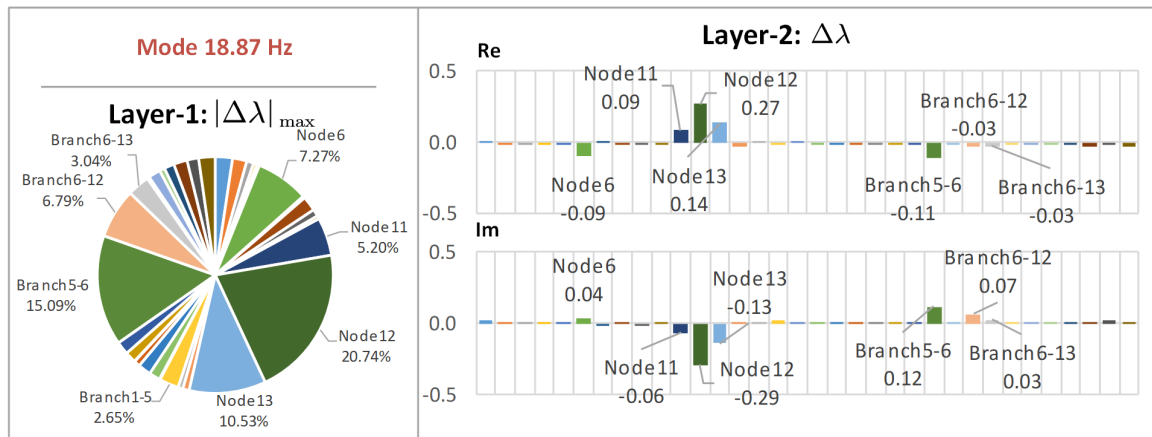


Figure 4.5: Grey-box layer-1 and layer-2 results for 18.87 Hz mode, showing that apparatus at nodes 11, 12 and 13, and the adjacent impedances branches have the highest participations. The layer-2 results are normalized to the sum of absolute values.

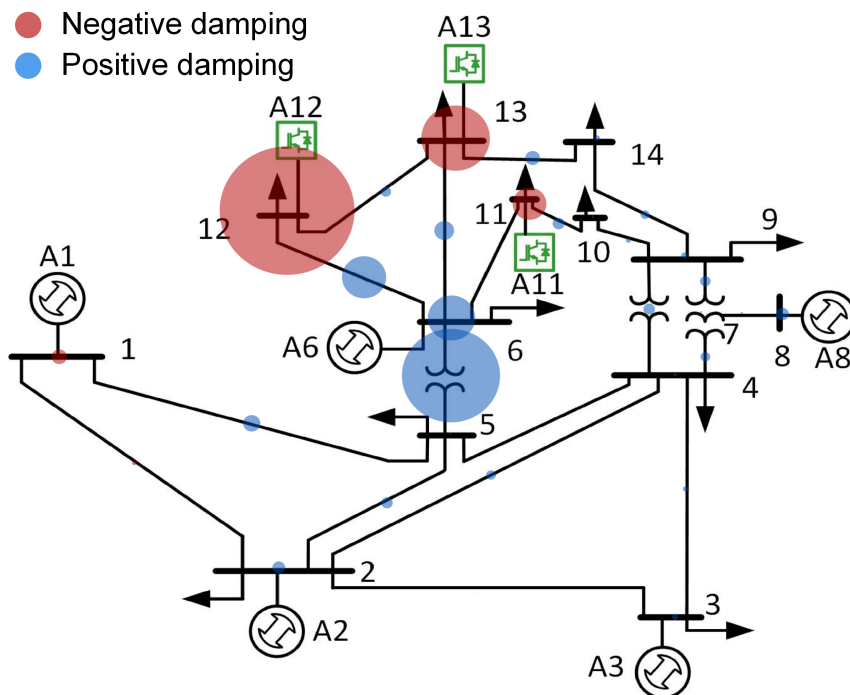


Figure 4.6: Oscillation propagation in the system. The circles represent the sensitivity of 18.87 Hz mode to nodes and branches, indicating the origins and the propagation of the oscillation. The circle radii are proportional to the results in the grey-box layer-1, and the filling color is determined by the sign of the real-part in layer-2.

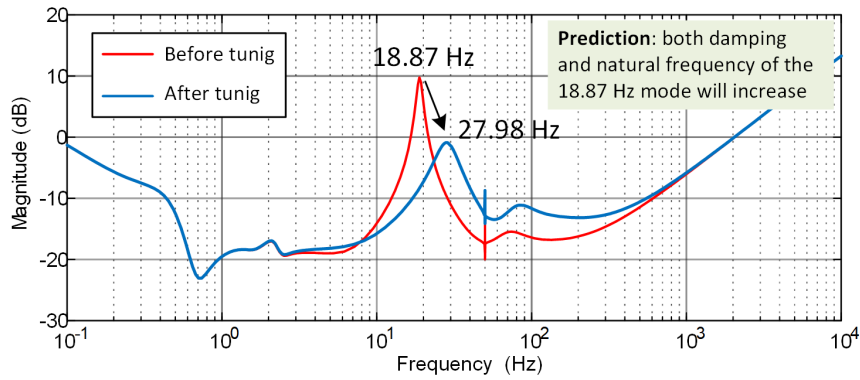
Table 4.3: Grey-box layer-3: significant parameter sensitivity factors in A11, A12 and A13 with respect to 18.87 Hz mode

Apparatus	Parameter ρ	Original value	$s_{\lambda,\rho} \cdot \rho$
A11	X	0.03 pu	-1.014+j1.346
A11	f_i	400 Hz	-1.818+j2.922
A12	f_{vdc}	10 Hz	1.420+j1.465
A12	X	0.03 pu	-3.171+j6.089
A12	f_{pll}	10 Hz	1.511+j1.118
A12	f_i	300 Hz	-5.039+j13.317
A13	X	0.03 pu	-1.946+j2.873
A13	f_i	350 Hz	-3.379+j6.279

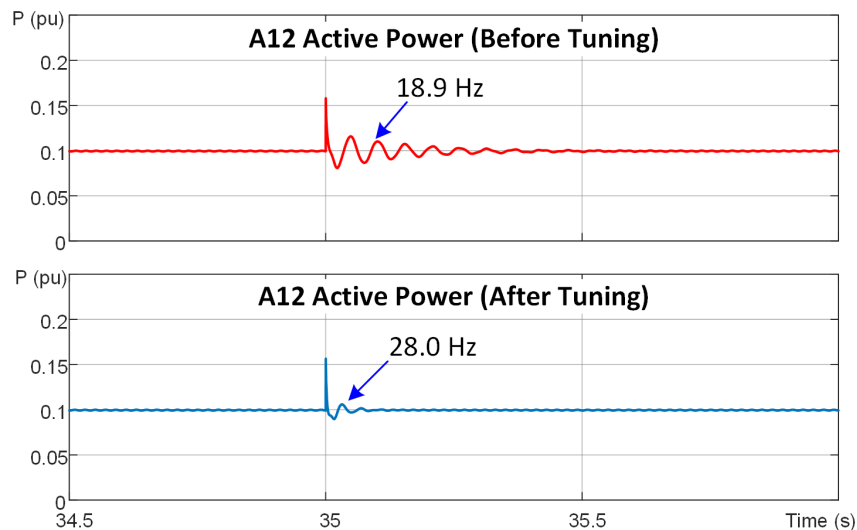
X output reactance
 f_i current control bandwidth
 f_{vdc} dc-link voltage control bandwidth
 f_{pll} phase-lock loop control bandwidth

the resonance peak is notably flattened but also the frequency is increased from 18.87 Hz to 27.98 Hz as expected from the positive imaginary part of the sensitivities. Fig. 4.7 (b) shows the active power output of A12 in a time-domain simulation, in which the load at bus 12 is increased by 100% at $t=35$ s which causes a lightly damped oscillation in power flow at 18.9 Hz. It can be clearly seen that in the re-tuned system, the mode is significantly better damped and the oscillation frequency has changed to 28.0 Hz. To tune the mode to a precise characteristic, the whole-system impedance analysis and grey-box sensitivity can be applied iteratively.

The vector fitting process is also demonstrated here to show the practical application of the grey-box approach. The fitting is based on rational approximation [57] and the codes can be accessed from [100]. Because the main purpose of this part is to demonstrate the fitting process and the accuracy, only spectra of $Z_{12,12}^{sys}$ and $Z_{13,13}^{sys}$ in $d-d$ axis are employed for further analysis because A12 and A13 are the dominants of the oscillatory mode. For each impedance, 81 frequency response data points, from 1 Hz to 1000 Hz, are taken out from the theoretical impedance spectrum for vector fitting, which is consistent with the frequency scanning fulfilled in Chapter 5. The two sets of data are fitted together such that a series of common poles can be acquired. Although the order of the original state-space model is 317, the fitting order can be selected much lower depending on what the shapes of the spectra look like. In this case, the fitting order is selected as 20 based on a series of preliminary tests. Typically, the higher the order is, the lower the fitting error would be, but the longer time the fitting



(a)



(b)

Figure 4.7: Re-tuned system with an increase in current control bandwidth of A11, A12 and A13 by 20%, 50% and 28.5%, respectively: (a) Bode plot of the $d-d$ term of $Z_{12,12}^{\text{sys}}$ showing the mode reshaped as predicted; (b) Time domain simulation: active power of A12 during a 100% demand increase at bus 12 at $t=35$ s, showing significant improvement in system damping after tuning.

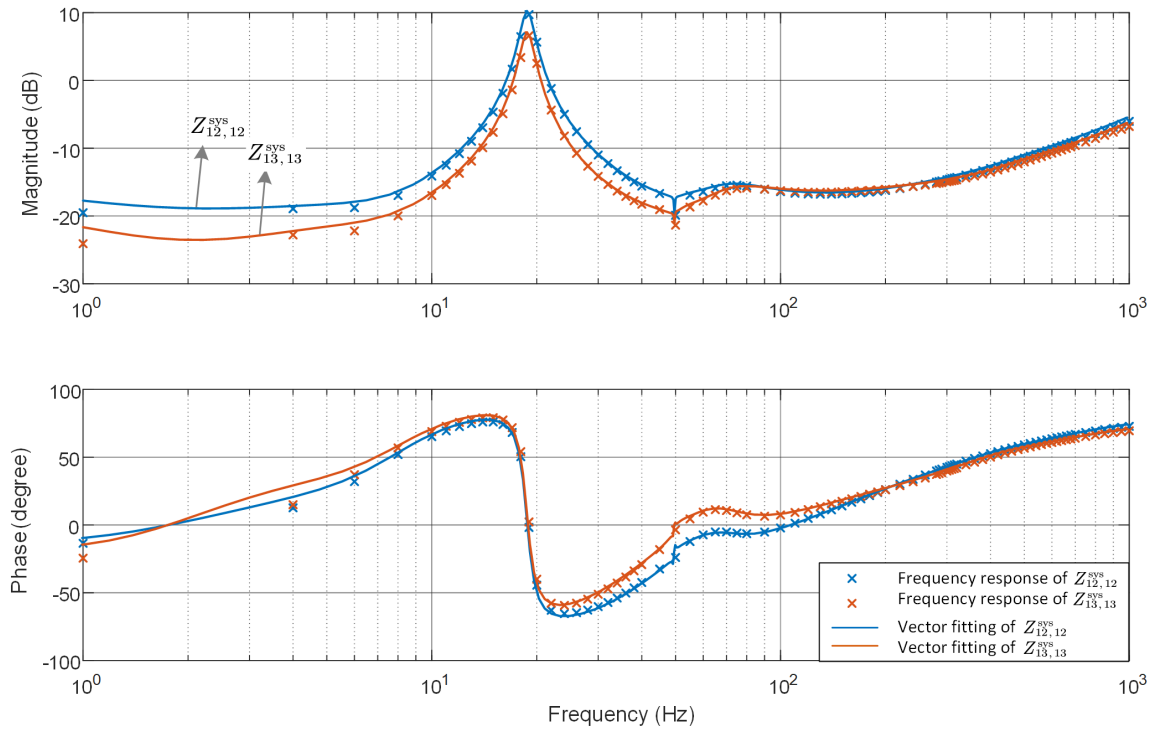


Figure 4.8: Frequency response data points taken from the spectrum of $Z_{12,12}^{\text{sys}}$ and $Z_{13,13}^{\text{sys}}$ in $d-d$ axis and the spectra of 20-order transfer functions from the vector fitting results.

process would take. The result of vector fitting on a set of frequency response data can essentially be a state-space model or a transfer function model, and the two models can be easily converted to each other. Fig. 4.8 shows the frequency response points as well as the fitted spectra of $Z_{12,12}^{\text{sys}}$ and $Z_{13,13}^{\text{sys}}$ from these points. It can be seen that the vector fitting results can provide a good accuracy under a 20-order approximation.

Poles and residues corresponding to the 18.87 Hz oscillatory mode are further estimated from the fitting results, and are compared with the results derived from the original state-space model, as given in Table 4.4. It can be clearly seen that the errors of fitting results are maintained in a very low level, meaning they can be employed for further participation analysis in the grey-box approach with no issues. Since the errors are extremely low, the application of the fitting results in the grey-box approach is assumed to be nearly identical with the theoretical results so is not further demonstrated here. Still, in a real system, noise existed in the system can significantly affect the measured impedance frequency response so would lead to errors when doing vector fitting. Analysing the noise and choosing a suitable small-signal injection amplitude to a given accuracy are considered as the main tasks of Chapter 5.

Table 4.4: Vector fitting results: poles and residues corresponding to 18.87 Hz mode

	State-space results	Vector fitting results	Error
Poles (Hz)	-0.8557+18.8730j	-0.8558+18.8729j	0.0007%
Residue of $Z_{12,12}^{\text{sys}}$	15.9860+2.1687j	16.0088+2.1711j	0.1421%
Residue of $Z_{13,13}^{\text{sys}}$	10.9911+2.2566j	11.0118+2.2493j	0.1956%

4.3 Modified NETS-NYPS 68-bus System

We now demonstrate the grey-box approach through a large-scale power system with IBR present. The chosen system, Fig. 4.9, is based on the NETS-NYPS 68 bus system [104, 105] with six additional IBRs (Type-IV wind farms) connected to buses 17, 26, 28, 29, 58, 59. The SG at bus 15 is replaced with a grid-forming inverter. Each wind farm is an aggregate with a scaled rating representing many individual IBR. To make the system prone to oscillation, the frequency droop gain of A15 is deliberately de-tuned high, and the current control bandwidths of A28 and A29 are de-tuned by -40% and -56% respectively. All SGs use the same parameters as [104], meaning that A11 is poorly damped and the least stable generator in the system [105]. Parameters of the newly added IBRs are given in appendix D.2.

The previous two case studies performed analysis on Z^{sys} but, for illustration purposes, this case study selects Y^{sys} , the whole-system admittance model measured from voltage injections, for impedance participation factor analysis. Normally the the choice of model would be dictated by what is available.

The whole-system admittance of the network, constructed from the impedance of all apparatus and admittance of all of the network lines, is displayed in the Bode plot in Fig. 4.10. At each node, the whole-system admittance \hat{Y}_{kk} is a 2×2 matrix in the synchronous dq frame, but only one of the four elements in the matrix is displayed since that is sufficient to illustrate the characteristics of the system. Only the nodes with sources (SGs or IBRs) present are plotted because the other nodes are passive. Several resonant peaks appear in the Bode plot, each representing an oscillation mode in the system. The mode at 60 Hz arises from the flux dynamics of windings and lines, and is a standard feature [19]. The modes around 1-2 Hz are rotor swing modes of the SGs, and the mode at high frequency is caused by the LCL filter of the grid-forming inverter. Three modes, annotated 1 to 3 in Fig. 4.10, are selected for further analysis, and we use the grey-box approach to trace the root-cause of these modes and find

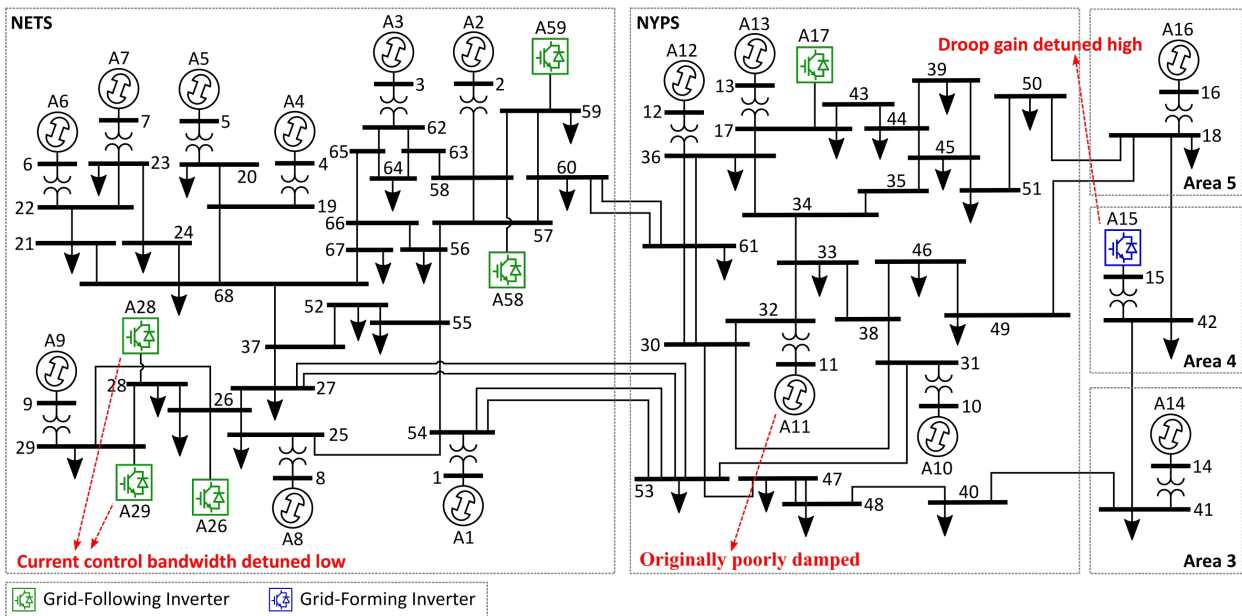


Figure 4.9: Modified NETS-NYPS 68 bus system, with 6 extra grid-following inverters, and a grid-forming inverter replacing the synchronous machine at bus 15.

ways to damp the modes.

Fig. 4.11 shows the results of applying grey-box Layer-1 (on the left) and Layer-2 (on the right). For mode-1 (5.6 Hz), A11 stands out in the Layer-1 pie chart. Further, the breakdown into real and imaginary components in Layer-2 shows that A11 affects both the damping and natural frequency of mode-1 while the adjacent apparatus A10 and A12 also influence the damping of this mode. The negative real-part in Layer-2 indicates that scaling up the power rating of A15 (which is equivalent to decreasing its impedance) tends to destabilise the system. Similar analysis of mode-2 shows that A15 is dominant in this mode, affecting both the damping and natural frequency. Mode-3 is more complicated: Layer-1 reveals that there are multiple participants (A9, A28, and A29), and the Layer-2 decomposition shows that the SG (A9) and the IBR (A28, A29) have opposite signs for the change $\Delta\lambda$. For A9, scaling up of power rating would improve stability whereas for A28 and A29 scaling up of the power rating decreases stability and indicates that mode-3 is an IBR-induced oscillation. Further, comparing A28 and A29, we see that A29 has a larger participation in this mode, which is attributable to the fact that A29 was de-tuned further than A28. The exact cause of the destabilisation is not revealed until Layer-3 of the grey-box which can point to particular components and control parameters. Nonetheless, Layer-1 and Layer-2 grey-boxes reveal rich information about the root-causes of modes 1, 2 and 3 without significant prior knowledge.

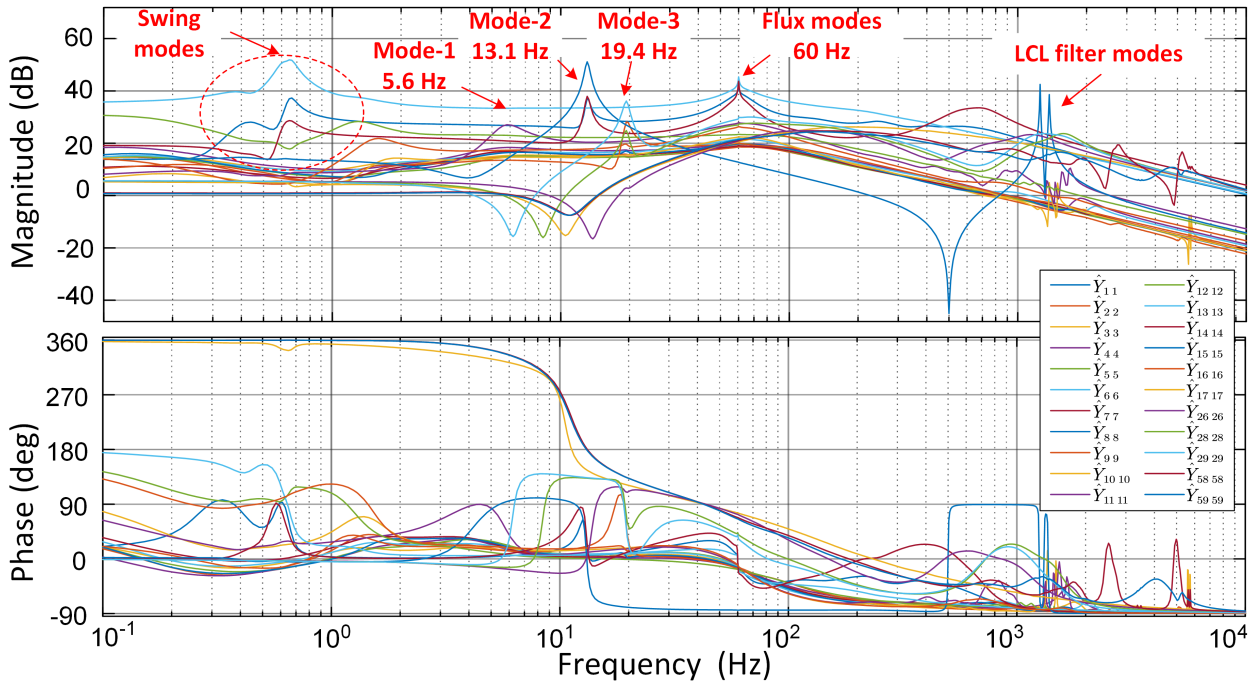


Figure 4.10: Bode diagram of whole system admittance \hat{Y}_{kk} at nodes with sources, presented in $d-d$ axis.

After locating the participating apparatus and identifying their roles in system stability, the final step is to use the grey-box Layer-3 to re-tune the parameters in A11, A15, A28 and A29 to improve the stability of the three modes. Based on the chain-rule, the parameter participation factors for mode-1, mode-2 and mode-3 against the internal parameters of A11, A15, A28 and A29 are calculated and illustrated in Fig. 4.12. The results used to draw Fig. 4.12 are shown in Table 4.5. It can be seen that mode-1 is sensitive to the physical parameters of A11 such as the sub-transient reactance and the inertia but also to control parameters in the automatic voltage regulator (AVR). In practice, it is easier to tune the control parameters, hence we can choose to increase the AVR feedback gain $K_{F(11)}$ to damp mode-1. For mode-2, both the dc-link control and the droop control of the grid-forming inverter have impacts on the damping but the mode is also sensitive to the LCL filter capacitor and inductor. Decreasing the frequency droop gain $K_{D(15)}$ shifts the mode leftwards and stabilises the system. This reflects the fact that $K_{D(15)}$ had been de-tuned high. For mode-3, parameters in A28 and A29 participate in a similar way to each other with those in A29 having a larger impact. This reflects the fact that A29 had been de-tuned further than A28. Looking inside each inverter, it can be seen that increasing the current control bandwidth f_i helps to stabilise the mode, but increasing the PLL bandwidth f_{PLL} tends to destabilise the mode. We can remark, therefore, that this mode

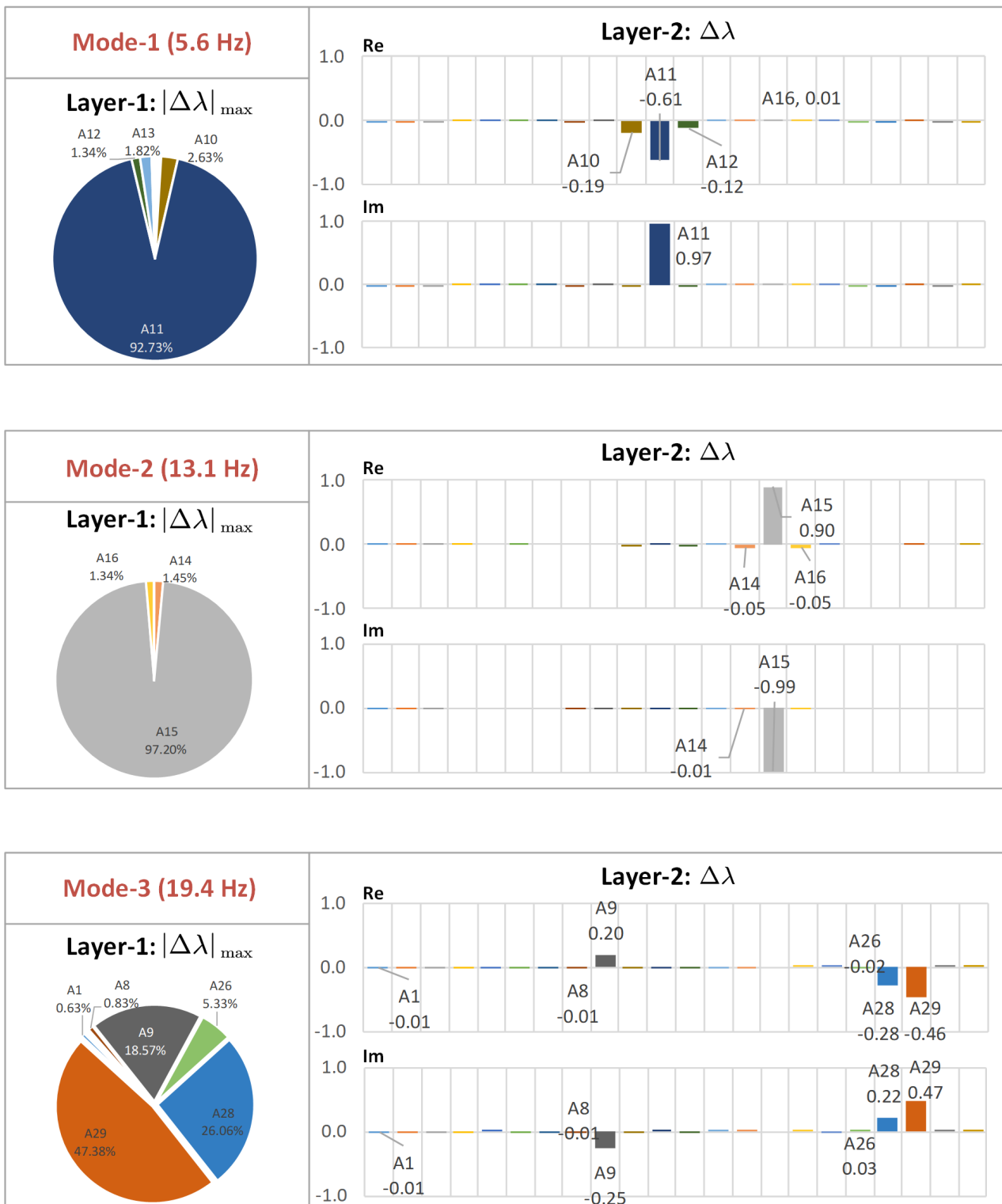


Figure 4.11: Participation analysis of the three under-damped modes using Layer-1 and Layer-2 of the grey-box, where the results in Layer-2 is normalized to the sum of absolute values.

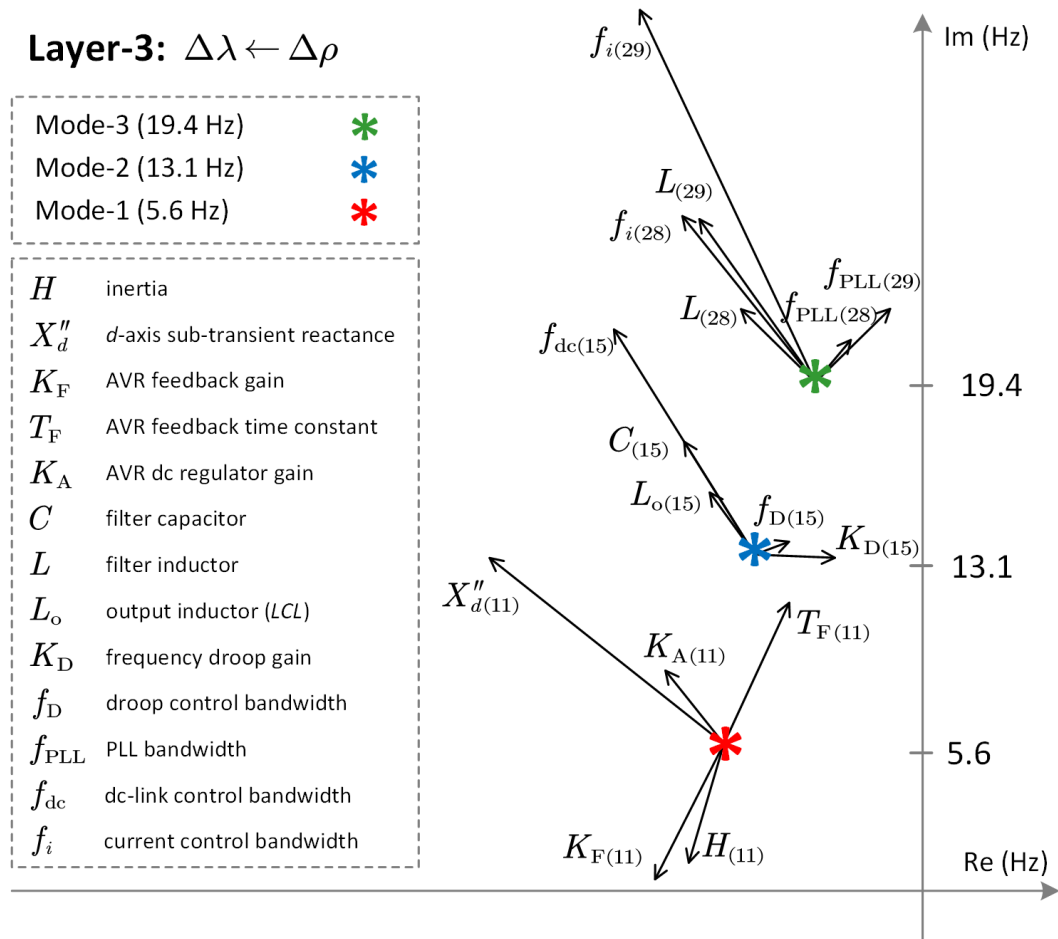


Figure 4.12: Grey-box Layer-3 analysis for the three under-damped modes. The parameter participation factors are represented as vectors around the associated modes showing the amplitude and direction of the eigenvalue variation subject to parameter perturbations. The parameter perturbations are proportional to the original value of parameters. The number in the parentheses in the subscript of each parameter indicates the number of the apparatus being analysed.

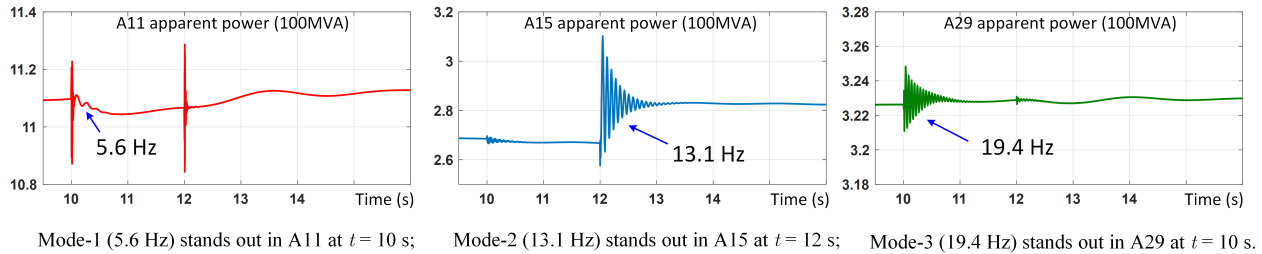
results from coupling between inner-loop (current control) and outer-loop (PLL) in a relatively weak grid. Such coupling effect can be explained as the interaction between the equivalent capacitance of inner-loop in d - q frame and the equivalent negative impedance of the outer-loop in q -axis [53, 103]. In this case, we choose to increase $f_{i(28)}$ and $f_{i(29)}$ to stabilise mode-3. For all the three modes, Layer-3 provides guidance on how to change control parameters to stabilise the system without the demand for changing the hardware.

It is worth noting that many of the parameters are directly associated with states. For example, the parameter participation factor of K_D is identical to the corresponding state participation factor of the droop control state. Thus Layer-3 provides similar interpretability to the classic state participation analysis.

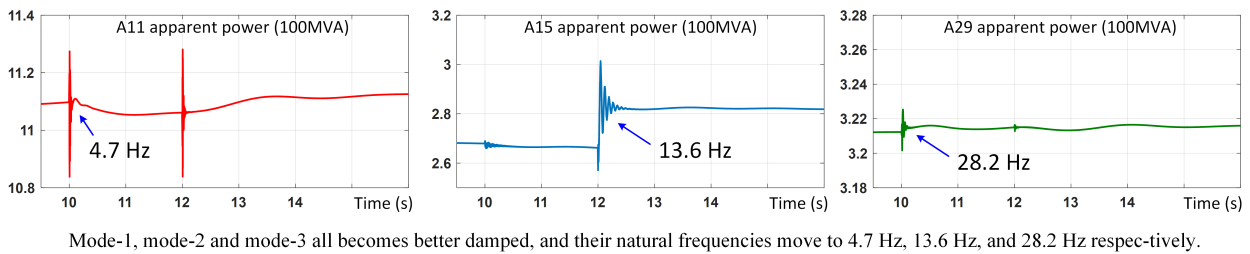
Table 4.5: Significant parameter participation factors for the three selected modes

Mode	Apparatus	Parameter	$p_{\lambda,\rho} \cdot \rho$
Mode-1 5.6 Hz	A11	H	-0.18-j1.88
	A11	X_d''	-3.45+j1.37
	A11	T_F	0.43+j0.97
	A11	K_F	-0.45-j0.96
	A11	K_A	-0.37+j0.59
Mode-2 13.1 Hz	A15	K_D	2.18-j0.56
	A15	F_D	0.91+j0.83
	A15	F_{dc}	-3.73+j19.60
	A15	C	-1.89+j9.82
	A15	L_o	-1.20+j5.46
Mode-3 19.4 Hz	A28	f_{PLL}	1.12+j1.33
	A28	f_i	-3.96+j5.60
	A28	L	-2.26+j2.48
	A29	f_{PLL}	2.27+j2.43
	A29	f_i	-5.25+j12.57
A29	L	-3.46+j5.49	

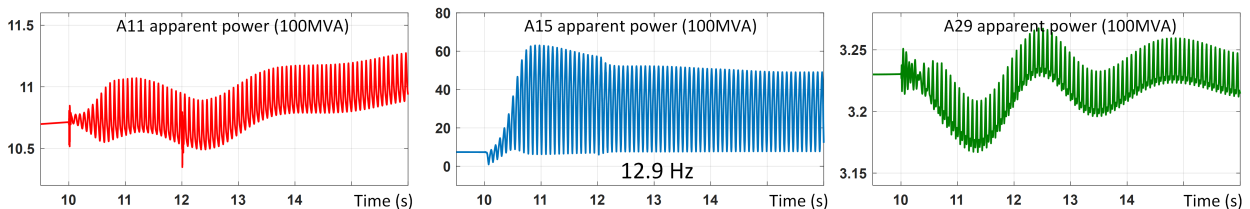
To verify the predictions of the three layers of grey-box analysis, time-domain simulation of this case-study was conducted with the apparent power output of A11, A15 and A29 recorded and displayed in Fig. 4.13. Two step-changes were introduced to the system to create transient behavior: the load at bus-61 was disconnected at $t = 10$ s, and a 5% increase in the load at bus-42 was applied at $t = 12$ s. Detailed description and discussion of the results are included in the caption and annotations. Natural frequencies can be measured from the time-domain oscillations and they are found to agree with the resonant peaks in the frequency domain spectra in Fig. 4.10. Different modes are excited in different apparatus, which agrees with the prediction of grey-box Layer-1 and Layer-2. The parameters of the participating apparatus were tuned in the directions indicated by grey-box Layer-3 and the damping of the modes is seen improved. The parameters were also adjusted against the grey-box indications and the damping is seen to worsen. The grey-box-based participation analysis has correctly located the root-cause of oscillations and indicated appropriate choices for achieving stabilisation. Eigenvalue plots before and after tuning are provided in Fig. 4.14, where it can be clearly seen that mode-1,2,3 are all shifted leftwards on the complex plane as predicted, with their damping improved, when tuned in accordance with the layer-3 indications. This proves that the grey-box approach can correctly show the tuning direction of parameters and help to stabilise the system.



(a) De-tuned system.



(b) Tuned following the grey-box results..



(c) Tuned against the grey-box results.

Figure 4.13: Apparent power output of A11, A15 and A29 during two transients: load-61 disconnected at $t = 10$ s, and load-42 increased 5% at $t = 12$ s. (a) De-tuned system with obvious oscillations during transient process; (b) Re-tuned by increase of $K_{F(11)}$ by 100%, decrease of $K_{D(15)}$ by 60%, and increase of $f_{i(28)}$ and $f_{i(29)}$ each by 50%, giving significant improvement in system stability; (c) Counter-tuned by increase of $K_{D(15)}$ by 50% leading to instability.

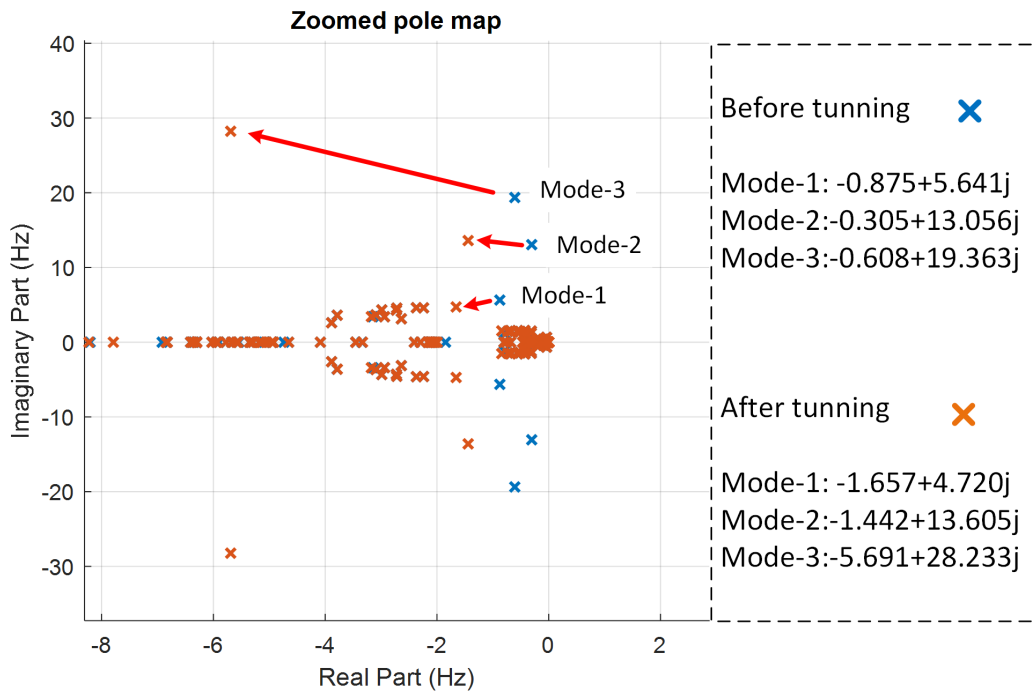


Figure 4.14: Eigenvalue plot of the 68-bus system before and after tuning the parameters, showing that mode-1,2,3 are shifted leftwards as predicted.

4.4 Summary

In this chapter, the comprehensive theory for root-cause analysis in impedance models and the grey-box approach are validated through three case studies: a three-node passive network, a modified IEEE 14-bus network and a modified NETS-NYPS 68-bus network. The theory and the grey-box approach have been proved to be effective in all case studies and oscillatory modes are successfully tuned to the desired direction. All the codes to generate the results were written in Matlab and are published in open-source form [100].

Chapter 5

Impedance Measurement and Noise Analysis

When considering implementing the proposed participation and sensitivity analysis in a power system, a major consideration is whether whole-system impedance or whole-system admittance can, in practical reality, be measured online. As discussed later in Chapter 5.1, such a measurement relies on small-signal voltage or current injections in the system. Challenges still remain in noise analysis and results validations of impedance measurement. This chapter takes a first look at the challenges of impedance measurement, and develops a full process of noise analysis which can help to determine an appropriate injection amplitude and validate the results. Considerations of stochastic processes and statistics are applied from which the minimum amplitude can be determined for injection that guarantees a certain maximum relative error (12% in the examples used) in the measured impedance. To demonstrate the newly developed process in a straightforward way, the process is introduced step by step via an experimental case. The same method could be applied readily in other cases.

5.1 Review of Impedance Measurement Techniques

Online impedance measurement is a potentially important way of obtaining a black-box impedance model, and a bridge to connect the analytical method with practical implementations. Efforts have been made to develop perturbation injection equipment configurations and suitable waveforms for

small-signal signal injections. In this section, an introduction to various methods of impedance measurement will be given, and some outstanding issues will be discussed.

5.1.1 Injection Topology

Impedance measurement is generally based on a series of small-signal injections of different frequencies. It is theoretically possible to use ambient data of the system to identify impedance, such as from the natural harmonics in the system [106–108], and system transients [109–111]. However, such methods rely on a specific configured environment, e.g., a step-response introduced by connecting a specific load to the network, and are mostly applied in offline systems. For real-time assessment in a large-scale system, measurement without active injections is highly dependent on system events and the signal-to-noise ratio of the measurement, thus has not been successfully applied. In contrast, deliberate and controlled waveforms, i.e., small-signal injection, provides better flexibility and accuracy, and is the mainstream technique for impedance measurement.

To inject small-signal perturbations into a grid system, it is important to choose a proper topology. Existing technologies include measurement in the abc frame [112], the $d-q$ frame [113] and the sequence frame [94], among which the $d-q$ frame impedance is widely used for stability analysis. This thesis focuses on only measurement in the $d-q$ frame. Four common injection topologies are illustrated in Fig. 5.1.

A straightforward method, as shown in Fig. 5.1(a), is to use a shunt-connected current source at the k -th node to inject small-signal current \tilde{i}_k and measure the variations in the voltage Δv_k . Such a source is independent and would be synchronised to the three phase network via PLL [113, 114]. From the injected current \tilde{i}_k and output signal Δv_k , the impedance can be acquired as

$$(Z_{Ak}^{-1} + Z_{Gk}^{-1})^{-1} \cdot \tilde{i}_k = \Delta v_k, \quad (5.1)$$

where Z_{Ak} is the impedance of the inverter at the k -th node, and Z_{Gk} is grid impedance seen from the k -th PCC. From the topology, it is clear that the measured result is the parallel-impedance of Z_{Ak} and Z_{Gk} . If further measurements of the small-signal current flowing into the inverter and into the

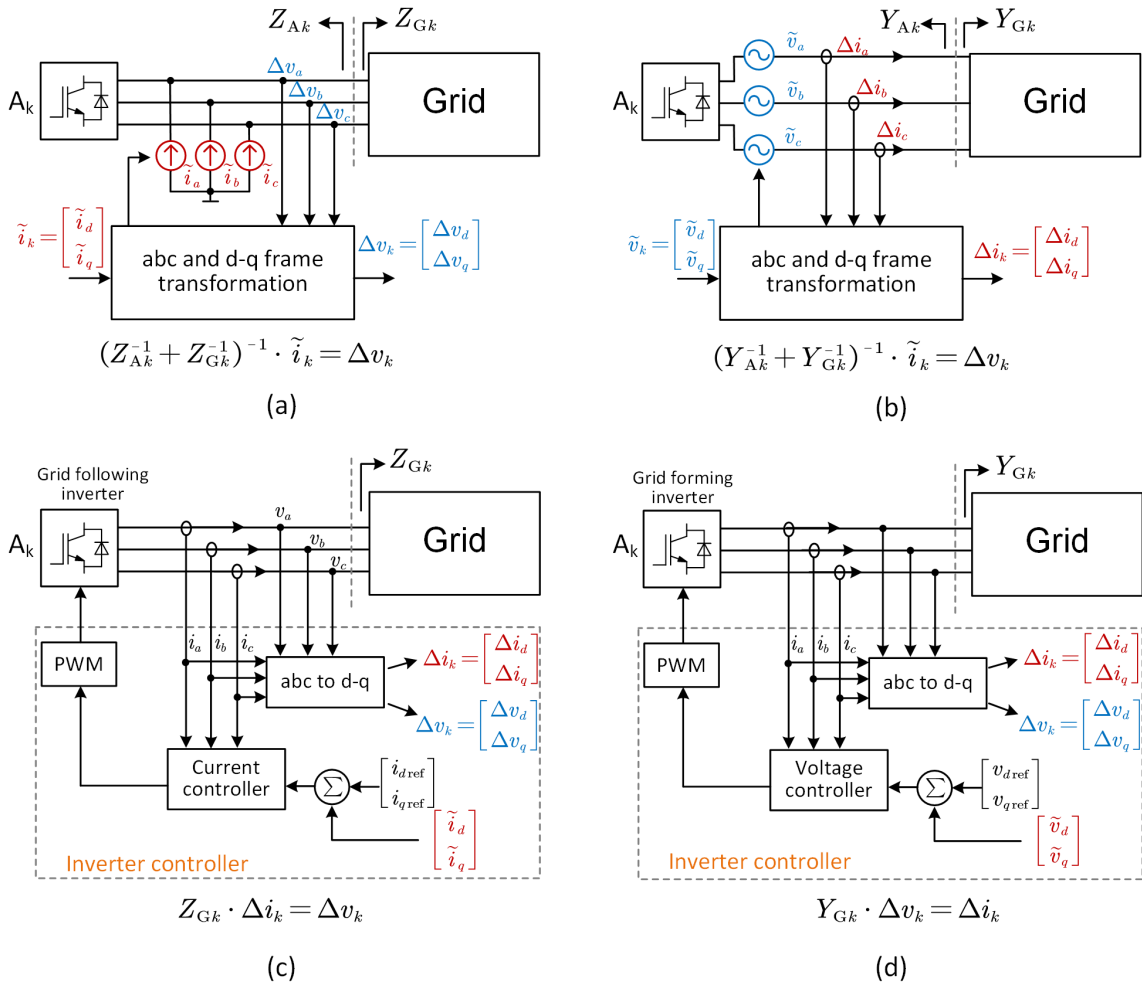


Figure 5.1: Small-signal injection topologies for impedance or admittance measurement: (a) independent current injection source. (b) Independent voltage injection source. (c) Noninvasive current injection from grid-following inverter. (d) Noninvasive voltage injection from grid-forming inverter.

grid are made, as in [45, 113], then Z_{A_k} and Z_{G_k} can be acquired separately. Similarly, as shown in Fig. 5.1(b), an independent series-connected voltage source can be employed to inject small-signal voltage perturbation \tilde{v}_k and measure the current flowing through this source Δi_k [61, 115, 116], such that

$$(Y_{A_k}^{-1} + Y_{G_k}^{-1})^{-1} \cdot \tilde{v}_k = \Delta v_k, \quad (5.2)$$

where Y_{A_k} is the admittance of the inverter at the k -th node and Y_{G_k} is grid admittance seen from the k -th PCC. The measured result is the series-admittance of Y_{A_k} and Y_{G_k} . It is worth noting that the injecting voltage source needs to be isolated perhaps by using transformers to connect it in series with the inverter [116].

In addition to independent injection sources which require extra devices, techniques using existing

inverters to measure impedance or admittance have been developed. In such techniques, small-signal perturbations are injected in the control loop of existing inverters so that perturbations can be generated at inverters' output ports. Because no extra sources are used, such a method is sometimes described as a noninvasive injection method but it does still involve injection of a perturbation. Fig. 5.1(c) shows the way of using grid-following inverter as the injection source [58, 59, 94]. The perturbation is added on the current reference in the control loop, while current perturbation Δi_k and voltage perturbation Δv_k are measured and the grid impedance can be identified as

$$Z_{Gk} \cdot \Delta i_k = \Delta v_k. \quad (5.3)$$

Similarly, as shown in Fig. 5.1(d), perturbations can be added on the voltage reference of a grid-forming inverter [117] and the grid admittance can be identified as

$$Y_{Gk} \cdot \Delta v_k = \Delta i_k. \quad (5.4)$$

Looking across different topologies, one can remark that an independent injection source may provide better data as it would be designed and instrumented specifically for small-signal injection. Its power rating could potentially be very small compared with the inverters in the system, and its bandwidth can be designed to be high in order to cover a wide-range of frequency.

Use of existing IBRs for small-signal injections could save cost and be considered non-invasive in not needing installation work to be carried out on site other than perhaps software enhancement. However, the bandwidth of IBR control loop is typically designed to be low (around 500 Hz for current control loop and 100 Hz for voltage control loop). As a result, perturbations above the bandwidth will be significantly attenuated so cannot be measured accurately. Besides, it is also worth noting that noninvasive injection method can only measure impedance of the grid, or devices connected at the output of the inverter, but not of the inverter undertaking the injection. Such impedance measurements could also benefit the control of the inverter through use of adaptive control [118], but is limited in terms of improving system stability because the impedances of both the inverter and the grid are needed for stability analysis.

Considering the weakness of using existing IBRs for small-signal injections, independent injection sources are preferred for high accuracy and wide frequency range measurement.

5.1.2 Injection Waveform

There are a variety of ways of choosing the injected waveforms. Narrowband injection and wideband injections are two major categories of injection waveforms for impedance measurement.

Narrowband injection is a well-studied method for impedance measurement, which is essentially a series of sine waves at different frequencies, and is usually referred as a frequency sweep, sine sweep, or frequency scanning. Such a method has been widely applied in DC systems [119–121] and has been extended to three-phase AC systems [45, 55, 122–127]. Generally, narrowband injection is considered as the most accurate method. The amplitude of each sinewave term and the number of cycles injected for each frequency can be configured in a variety of ways, such that the injected energy can be regulated in a very flexible way. However, one major drawback is that the total measurement time is considerable, especially when low-frequency points are measured such as 1 Hz. Still, the experience of the tests in this thesis indicated that with a careful choice of injected frequencies, duration of each injection, and interval between each groups of sine waves, the total sweep time for of around 30 s was enough to scan 1-1000 Hz. This was judged to be an acceptable for online impedance measurement in power systems.

In contrast, wideband injection is based on a high-frequency content signal to excite a wide range of frequencies of interest. Such methods have been widely-studied and are often based on injecting a pseudorandom binary sequence (PRBS) [58, 59, 94, 117, 128, 129], a chirp signal [93, 130], pulses [131, 132] or step changes [109, 110, 133]. Because a variety of frequencies can be excited and identified at the same time, a wideband method can significantly accelerate measurement process compared to narrowband and thus is suitable for online measurement and real-time monitoring. However, large magnitude perturbations are normally involved for wideband injections because some frequencies may not be excited distinctly without a large magnitude of input. The large perturbations may produce a nonlinear response from the system, undermining the basis of linear analysis and

affecting system stability [58, 93]. Another issue is that the signals of different frequencies may not be orthogonal in a non-linear system and can affect each other when performing the Fourier transformation, so that the accuracy of wideband injections are considered less accurate than narrowband injection.

The debate on the most suitable waveforms is still on going. It was decided to contribute to the debate with a focus on measurement noise and its influence on accuracy and the required injection amplitude. Frequency sweep was selected for the study because of its high accuracy and simplicity.

5.1.3 Work Described in this Chapter

As with any measurement process, the process of impedance identification involves errors which may severely affect the final results. Two unsolved issues related to measurement error have been introduced in Chapter 1.3.3.

This chapter aims to address the issues by developing a method which can determine the minimum necessary injection amplitude based on an allowable error needs to be developed. Alongside this, a method is needed to determine what the true value of the impedance of a physical systems is so that measurements can be judged for accuracy and, indeed, a metric for measurement error needs to be established so that measurement results can be compared with each other.

5.2 Online Measurement Test Bench

Because the focus is on measurement error, which is a problem caused by hardware devices, simulation software is not capable of resolving the issues since the non-linear behaviours of inverters and noise in the system cannot be emulated perfectly in software. As a result, a hardware test bench is required for further analysis. Based on the discussions in Chapter 5.1, one can see that to build a hardware test bench in a laboratory for impedance or admittance measurement, there are several difficulties to be overcome. First, an independent injection source is needed. Such an injection source is desired to have high bandwidth (to cover a wide frequency range), high accuracy (to inject the

requested perturbations accurately), and a certain power capability (to source the power needed for small-signal injections). Besides this, in order to validate fully the feasibility of online measurement in power systems, a system of sufficient scale is desired, which is difficult to achieve in most research laboratories. To overcome the above theses limitations, a power hardware-in-the-loop (PHIL) system is adopted which will be introduced in the following subsection before turning to the testing process.

5.2.1 Introduction of PHIL technique

PHIL is an extension of the hardware-in-the-loop (HIL) technique, and is a hybrid system that contains both real-time simulations (software) and device under test (DUT, hardware). Compared with HIL in which the signals exchanged between software and hardware are low-voltage, low-current signals, PHIL is also capable of exchanging significant power required by the DUT. The basic configuration of a PHIL system is shown in Fig. 5.2 [134]. The target system is split into a software part running in real-time simulator, and a hardware part as a DUT. Within the hardware section, a controlled voltage source generates the same voltage as u_1 in the software. This is paired with a controlled current source in the software section which draws the same current i_1 as the DUT. In practice, a power interface is needed, which can read the simulated voltage value u_1 and generate the same voltage physically u_1'' , meanwhile it samples the physical current i_1 and feeds the value back to the simulation. Such an interface is named a power interface (PI) and the device to perform this interface is known as a power amplifier (PA). With the help of the PHIL technique, devices with power input or output such as IBR can be tested in an appropriate environment by simulating in real-time a power system with the real IBR connected to one node of that system. Such configuration can help with the analysis of IBR's interaction with the system.

There are several types of PA and PI, which are discussed in detail in [134], and those details are not repeated here. In this experiment, a switched-mode PA and ideal transformer model of voltage type PI are employed. Because the PA is configured as a voltage type, it is only able to inject voltage signals into the system and as a consequence it is whole-system admittance Y^{sys} that is measured in the experiment.

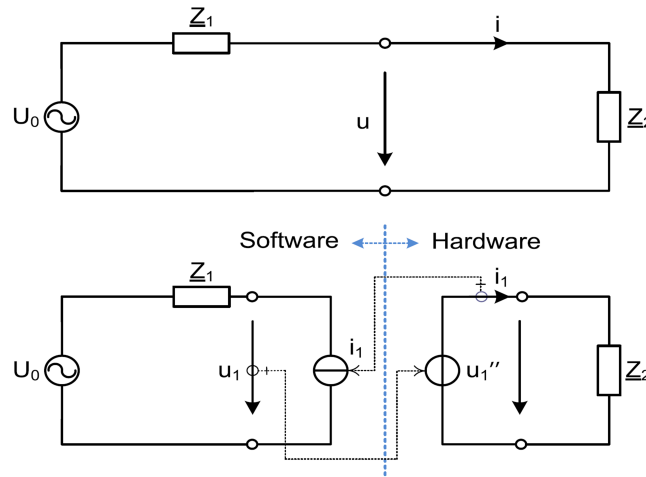


Figure 5.2: Basic configuration of PHIL system [134]. Copyright © 2016, IEEE.

5.2.2 Experiment Test Bench

Because the main focus of this chapter is to demonstrate the process of impedance measurement and the methodology of noise analysis, a simple system with one IBR connected to infinite bus is employed. Fig. 5.3(a) shows the single-line diagram of the tested system. The infinite bus voltage is 200 V_{rms}, the line is 0.18 H, the load is 3000 W and -1000 Var, and the inverter feeds 1200 W and 400 Var to the grid. An voltage injection is placed in series with the IBR so that whole-system admittance Y^{sys} can be measured, that is,

$$\Delta i = Y^{\text{sys}} \cdot \tilde{v}. \quad (5.5)$$

This system contains only one node (the infinite bus is ideal so is merged into the network matrix Y_N) so the system admittance matrix is only 2×2 :

$$Y^{\text{sys}} = \begin{bmatrix} Y_{dd}^{\text{sys}} & Y_{dq}^{\text{sys}} \\ Y_{qd}^{\text{sys}} & Y_{qq}^{\text{sys}} \end{bmatrix}, \tilde{v} = \begin{bmatrix} \tilde{v}_d \\ \tilde{v}_q \end{bmatrix}, \Delta i = \begin{bmatrix} \tilde{i}_d \\ \tilde{i}_q \end{bmatrix}. \quad (5.6)$$

Fig. 5.3(b) shows how the test system is configured in the PHIL system, where the left-part is the software part that runs in the real-time simulator and the right-part is a real grid-following inverter. The voltage v_o and current i_o consist of both the steady value and small-signal perturbation, and are

sampled by the PA. The admittance measurement is designed as follows:

- Frequency sweep is selected as the measurement method, which is the more accurate impedance measurement method as noted in Chapter 5.1.2. The sweep covers from 1 Hz to 1 kHz in recognition of the limitations of the equipment (bandwidth of the injection source is 10 kHz, as will be introduced later).
- Each frequency point comprises 7 cycles of injected signal, of which the first two cycles are considered as pilot cycles with no measurement taken during that period. This is to ensure that the measured current response contains no transient period. In addition, the injection is also preceded by 2 cycles of with no injection to allow the system to settle from any previous injection. Each round of sweep consists of 81 frequency points and takes around 30 seconds.
- Although the measurement is carried out on both d and q axis, the analysis is only performed on the d - d axis, i.e., Y_{dd}^{sys} . The same analysis can be extended to any of the axes. For the sake of brevity, Y^{sys} is used in the following discussion to represent Y_{dd}^{sys} .

Fig. 5.4 shows the experimental platform in for the configuration discussed. On the left-part of the figure, is the power amplifier which is an OP1400 from the company Opal-RT and it houses two OP8100 PAs which are the devices to generate voltage and exchange power with DUT. The bandwidth of the PA extends to 10 kHz, and the total harmonic distortion (THD) for the range 0-1 kHz is maintained below 0.5%, which guarantees a nearly ideal small-signal injections. The maximum output line-to-neutral voltage is 240 Vrms and in this experiment the output is 200 Vrms. The real-time simulator used is a OP5707, which is a high-end FPGA-based simulator with 16 Intel Xeon cores. The simulation runs with a time-step of $50 \mu\text{s}$, which is an update rate of, 20 kHz. This is also the current and voltage sample rate. The data exchange between software and hardware is fulfilled via fiber optic communication between OP5707 and OP8100.

In the right-part of the figure, the grid-following inverter, also known as DUT, is a three-phase inverter manufactured by Triphase (a company acquired by National Instrument in 2018) with a rated power of 10 kVA. The inverter is controlled via a Triphase real-time target (RTT), which is based on

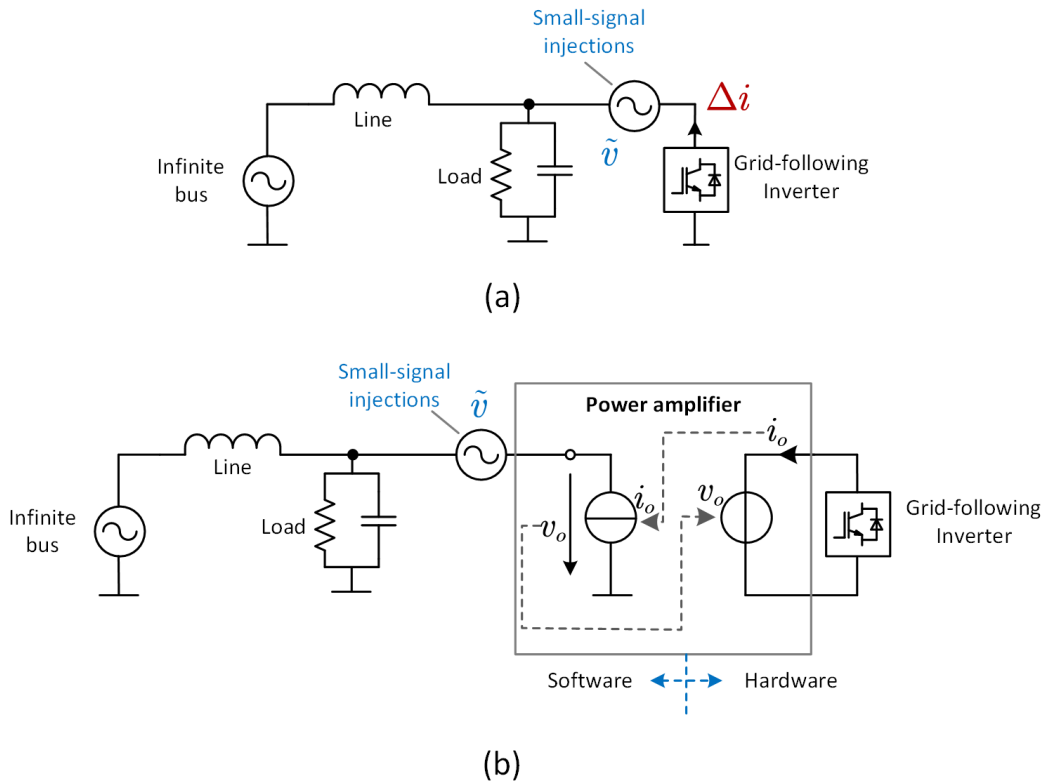


Figure 5.3: Single-line diagram of the three-phase experiment: (a) illustration of the aiming tested system. (b) Configuration of the tested system in PHIL platform.

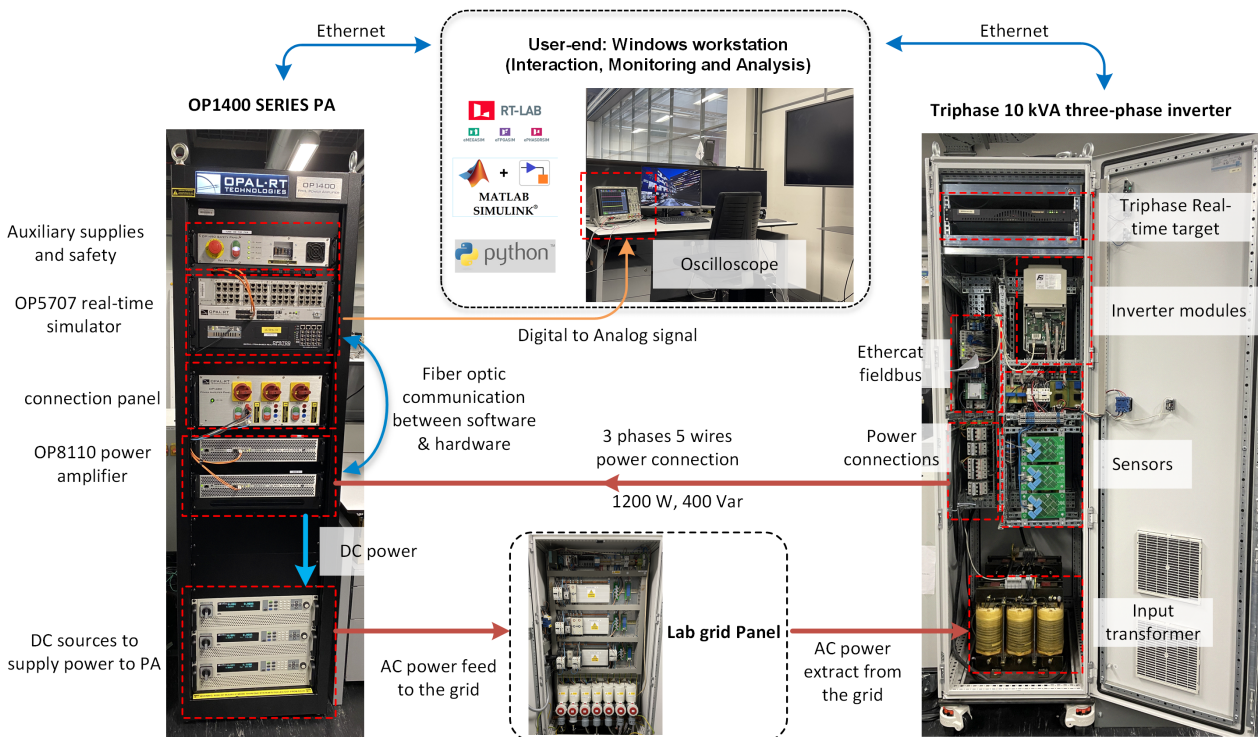


Figure 5.4: Experiment platform for the system.

rapid control prototyping (RCP) technique, allowing users to develop control algorithms in Matlab Simulink. The schematic of the inverter is provided in appendix D.3.

Looking now at the bottom of Fig. 5.4 it can be seen that the DC power sources supply the PA and the Triphase inverter (DUT) are connected to the lab grid panel. Thus, power absorbed by one is fed back to the point where the other drew its power and, subject to power conversion losses, power is circulated around a loop.

At the top of the figure, a Windows-system workstation is shown, which is connected to the OP1400 and the inverter via an Ethernet connection. This workstation has several items of software including RT-Lab, Matlab, Simulink and Python, through which the workstation can fulfill tasks including user interaction, monitoring, data acquisition and analysis. An oscilloscope is also employed to monitor real-time waveforms generated from OP5707's digital-to-analog converter (DAC) port.

5.3 Noise Analysis for Measurement

When measuring the impedance or admittance at a PCC, the noise observed comes from sources in the grid-side, sources in the inverter-side, and the background noise from both sides. The signal injection source and the sampling circuit may also contribute noise but such noise is typically small when the injecting source is well designed, as is the case for the power amplifier employed in this experiment. Importantly, features of noise are determined by the design of an individual case and it can not be assumed that there is a single set of noise features that could cover all situations. As a result, a methodology to analyze the noise for individual cases is needed. In this section, a method to analyze the noise and its impact on measurement results will be proposed, and experimental results will be presented to verify the proposed method.

To begin with, three premises are introduced which will be used in the following sections:

Premise 5.1 *The system is considered to be time-invariant during the impedance measurement period since the measurement period is around 30 s, which is short compared with variations of operating point of a grid system.*

Premise 5.2 *The noise is additive noise. This is because the injecting source is an independent source, and considered as ideal.*

Premise 5.3 *During a 30 s measurement period, the noise is considered to be a wide-sense stationary (WSS) stochastic process. This is because when the system is time-invariant, the noise mainly consists of background noise, which is typically white Gaussian noise (WGN), and harmonics in the system which are sinewaves with random phases, which are all wide-sense stationary stochastic processes.*

The definition of WSS is introduced in B.4, and proof of the third premise is given in A.6.

5.3.1 Discussion of measurement error

As mentioned in Chapter 5.1.3, the error in the measurement result should be discussed in terms of the complex plane. Since the result is a frequency spectrum $Y^{\text{sys}}(j\omega)$, it is difficult to select a metric to represent the error of the whole curve. Consequently, the error should be analyzed at each frequency point instead of the whole spectrum. The goal is to confine the relative error at each frequency to be within a certain range.

Consider a frequency point f_c , the injected voltage on the d axis is

$$\tilde{v}(t) = V_c \cos(2\pi f_c t), \quad (5.7)$$

where the injected amplitude is V_c and phase is 0. The measured small-signal output is a current which can be expressed as

$$\Delta i_c(t) = I_{c0} \cos(2\pi f_c t + \theta_{c0}) + n(t), \quad (5.8)$$

where I_{c0} is the true amplitude of output current, θ_{c0} is the true phase, and $n(t)$ refers to the noise which is a stochastic process and is additive noise as set out in premise 5.2. To acquire the amplitude and phase of current from the time-domain signal, signal demodulation is needed which is based on

the Fourier transform:

$$\begin{aligned} I_{c\text{-Re}} &= \frac{2}{k_c T_c} \int_0^{k_c T} \Delta i_c(t) \cdot \cos(2\pi f_c t) dt \\ I_{c\text{-Im}} &= \frac{2}{k_c T_c} \int_0^{k_c T} \Delta i_c(t) \cdot \sin(2\pi f_c t) dt, \end{aligned} \quad (5.9)$$

where k_c is number of the injected cycles of perturbation, and $T_c = 1/f_c$, $I_{c\text{-Re}}$ and $I_{c\text{-Im}}$ are the real and imaginary-part of I_c , i.e., $I_c = I_{c\text{-Re}} + jI_{c\text{-Im}}$. The above equation is written in continuous form but can be easily transferred into discrete form. Substituting (5.8) into (5.9) yields

$$\begin{aligned} I_{c\text{-Re}} &= I_{c0\text{-Re}} + N_{c\text{-Re}} \\ I_{c\text{-Im}} &= I_{c0\text{-Im}} + N_{c\text{-Im}}, \end{aligned} \quad (5.10)$$

where $I_{c0\text{-Re}}$ and $I_{c0\text{-Im}}$ are the true real and imaginary-part of current output, and $N_{c\text{-Re}}$ and $N_{c\text{-Im}}$ are the errors caused by the noise where

$$\begin{aligned} N_{c\text{-Re}} &= \frac{2}{k_c T_c} \int_0^{k_c T} n(t) \cdot \cos(2\pi f_c t) dt \\ N_{c\text{-Im}} &= \frac{2}{k_c T_c} \int_0^{k_c T} n(t) \cdot \sin(2\pi f_c t) dt. \end{aligned} \quad (5.11)$$

Based on the above, the true admittance at f_c is

$$Y_{\text{true}}^{sys} = \frac{I_{c0\text{-Re}}}{V_c} + j \frac{I_{c0\text{-Im}}}{V_c}, \quad (5.12)$$

while the measured admittance at f_c is

$$Y_{\text{meas}}^{sys} = \left(\frac{I_{c0\text{-Re}}}{V_c} + \frac{N_{c\text{-Re}}}{V_c} \right) + j \left(\frac{I_{c0\text{-Im}}}{V_c} + \frac{N_{c\text{-Im}}}{V_c} \right). \quad (5.13)$$

The relative error η at frequency f_c is then defined as the distance between true value and measured value divided by the true value. Combining (5.8), (5.12) and (5.13) yields

$$\eta(f_c) = \frac{|Y_{\text{meas}}^{sys} - Y_{\text{true}}^{sys}|}{|Y_{\text{true}}^{sys}|} = \frac{\sqrt{N_{c\text{-Re}}^2 + N_{c\text{-Im}}^2}}{|I_{c0}|}. \quad (5.14)$$

Here we define the term $\sqrt{N_{c-\text{Re}}^2 + N_{c-\text{Im}}^2}$ as the noise impact on frequency point f_c since it is the absolute error caused by the noise. Equation (5.14) forms the basis of the proposed noise analysis method, as introduced in the next subsection.

In reality, the true value of the small-signal current output can never be known, i.e., $I_{c0-\text{Re}}$ and $I_{c0-\text{Im}}$ cannot be known. As a result, it is difficult to assess the errors in the experiment. However, from the proof of premise 5.3 in appendix (A.6), it is known that the noise is WSS process composed of WGN and harmonics, and the expected value of the is zero. Under such premise, it can be easily known that

$$E(N_{c-\text{Re}}) = E(N_{c-\text{Im}}) = 0. \quad (5.15)$$

This condition holds true in most cases of impedance measurement. Combining (5.15) and (5.10) yields

$$\begin{aligned} E(I_{c-\text{Re}}) &= E(I_{c0-\text{Re}}) + E(N_{c-\text{Re}}) = I_{c0-\text{Re}} \\ E(I_{c-\text{Im}}) &= E(I_{c0-\text{Im}}) + E(N_{c-\text{Im}}) = I_{c0-\text{Im}}. \end{aligned} \quad (5.16)$$

Equation (5.16) shows that the expected value of measurement result is equal to the true value of current signal. According to the law of large numbers (appendix B.5), when there is a large number of repetitions of the same test, the expected value will be very close to the average value of tests. Combined with (5.16), the true value of small-signal current at frequency of f_c can be derived as

$$\begin{aligned} I_{c0-\text{Re}} &= \lim_{N_T \rightarrow \infty} \sum_{i=1}^{N_T} \frac{I_{c-\text{Re}-i}}{N_T} \\ I_{c0-\text{Im}} &= \lim_{N_T \rightarrow \infty} \sum_{i=1}^{N_T} \frac{I_{c-\text{Im}-i}}{N_T} \\ I_{c0} &= I_{c0-\text{Re}} + jI_{c0-\text{Im}}, \end{aligned} \quad (5.17)$$

where the subscript i refers to the i -th test and N_T is the total number of tests. Equation (5.17) shows a way to acquire the true value and to verify the error present in experiments.

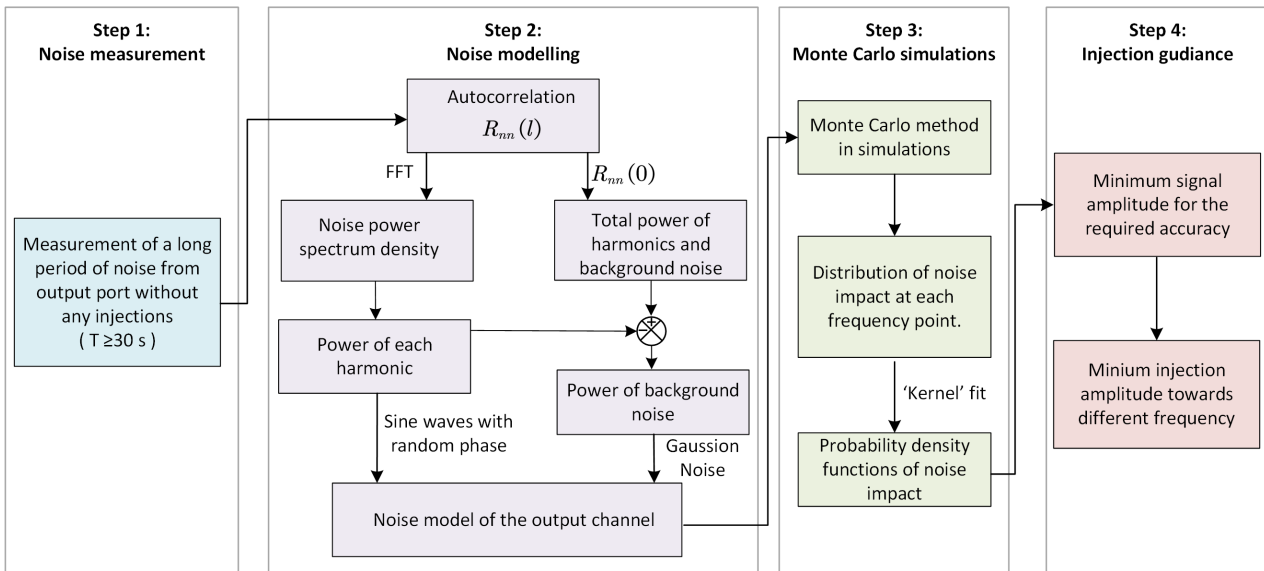


Figure 5.5: Method of noise analysis and injection determination for impedance or admittance measurement.

5.3.2 Methodology

The proposed method of noise analysis and injection determination for impedance or admittance measurement is depicted in Fig. 5.5. The method contains 4 steps. For a better understanding, each step is introduced in turn together with the relevant experimental results.

A Step 1: Noise measurement

To evaluate the noise, the first step is to sample a long period of noise from the output port, i.e., current, without a injection present. Since the frequency sweep period is expected to be 30 s, the sampling period for this step is set as 30 s as well. It is important that the sample rate is the same as the rate used for the subsequent admittance measurement, i.e., 20 kHz in this work, since the noise is specific to the sample rate. Since the noise is a WSS process, the starting time of noise sampling won't affect the results. Fig. 5.6 shows an example measured current from d -axis for 30 seconds, together with a zoomed-in view showing that the noise includes both repetitive harmonic components and random background noise.

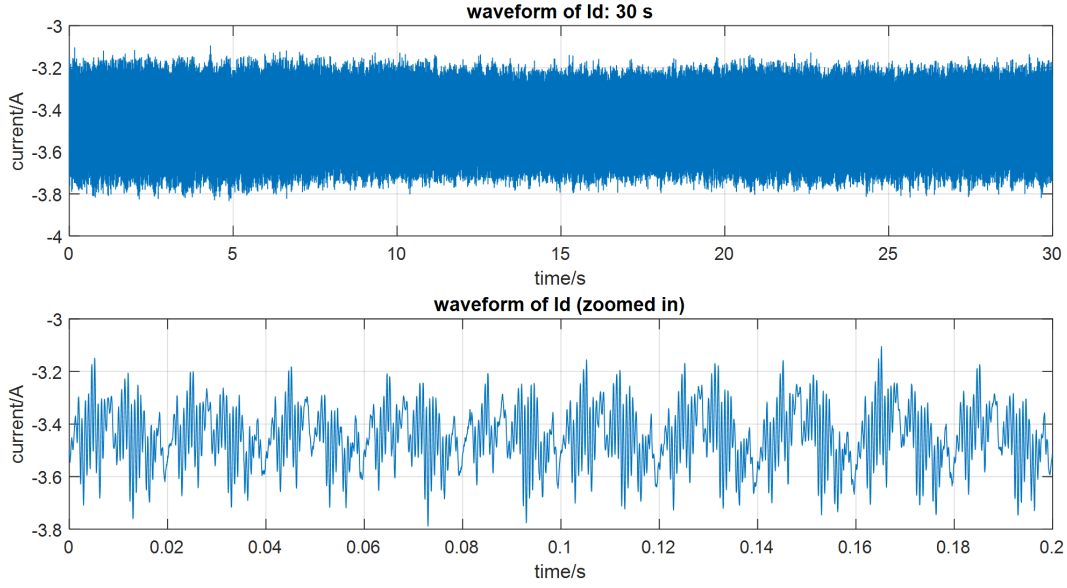


Figure 5.6: Waveform of d -axis current, with sample rate of 20 kHz on two timescales. Abundant noises can be observed.

B Step 2: Noise modelling

Autocorrelation is first applied to the noise since it is a general approach for power analysis of stochastic process. According to the definition introduced in appendix B.6, the autocorrelation of the noise $n(t)$ is

$$R_{nn}(l) = \frac{1}{N_s} \sum_{k=0}^{N_s-1} n(k) n(k-l), \quad (5.18)$$

where l and k are integers that refer to sample points, and N_s is the total number of sample points. Since $n(t)$ is a WSS process, we have

$$R_{nn}(0) = E(n^2(0)), \quad (5.19)$$

meaning that the total power of the noise equals $R_{nn}(0)$, which is a property of autocorrelation. Because this is a WSS process, the Wiener-Khinchin theorem can be applied, from which the power spectral density (PSD) of the noise can be acquired by performing a Fast Fourier transform (FFT) on $R_{nn}(l)$. Wiener-Khinchin theorem is introduced in appendix B.7. Fig. 5.7 shows the results of autocorrelation and PSD. The diamond shape indicates that the correlation value is decreasing along with the increasing value of interval $|k-l|$, which is in accordance with the feature of WSS

process [135]. This also proves that the assumption in premise 5.3 is correct. Also, the value at 0 is 0.01099 meaning that the total power of the noise is about 0.01099 W. The zoomed in autocorrelation plot also reveals the presence of harmonics at various frequencies. From the PSD plot, it is obvious that several peaks stand out in the spectrum, which are harmonics as might be expected from an inverter. Since the noise was observed on a d -axis signal, 50 Hz in this spectrum corresponds to DC in the physical signal and is a DC offset. Similarly, 300 Hz corresponds to the 5-th and 7-th harmonics. The terms above 1 kHz could be caused by excitation of resonances in the inverter's LCL output filter. The PSD indicates the power of each harmonic. Taking 300 Hz as an example, the power density at that point is 0.0411 W/Hz, and the frequency resolution in this case is 1/7.5 Hz. The power of 300 Hz harmonic P_{300} is therefore

$$P_{300} = 0.0411/7.5 = 0.00548 \text{ W}, \quad (5.20)$$

The harmonics appearing in Fig. 5.7 (b) with relative large power are picked out to build a model of the noise.

Using (5.19), the power of WGN, σ^2 , can be calculated as the difference between the total power and the power of the harmonics,

$$\sigma^2 = R_{nn}(0) - \sum_{i=1}^{k_m} P_{fi}, \quad (5.21)$$

where k_m is the number of selected harmonics, P_{fi} is the power of the i -th selected harmonic.

Based on the result of the autocorrelation and the PSD, the noise can be modeled as the sum of WGN and a harmonic series.

$$N_M(t) = G_W(t) + \sum_{i=1}^{k_m} H_i(t), \quad (5.22)$$

where $N_M(t)$ is the modelled noise, $G_W(t)$ is the WGN, and H_i is the i -th selected harmonic. For WGN, at any $t = t_0$,

$$G(t_0) \sim \mathcal{N}(0, \sigma^2). \quad (5.23)$$

The i -th harmonic is modelled as

$$H_i(t) = \sqrt{P_{fi}} \sin(2\pi f_i t + \theta_i), \quad \theta_i \sim U(0, 2\pi) \quad (5.24)$$

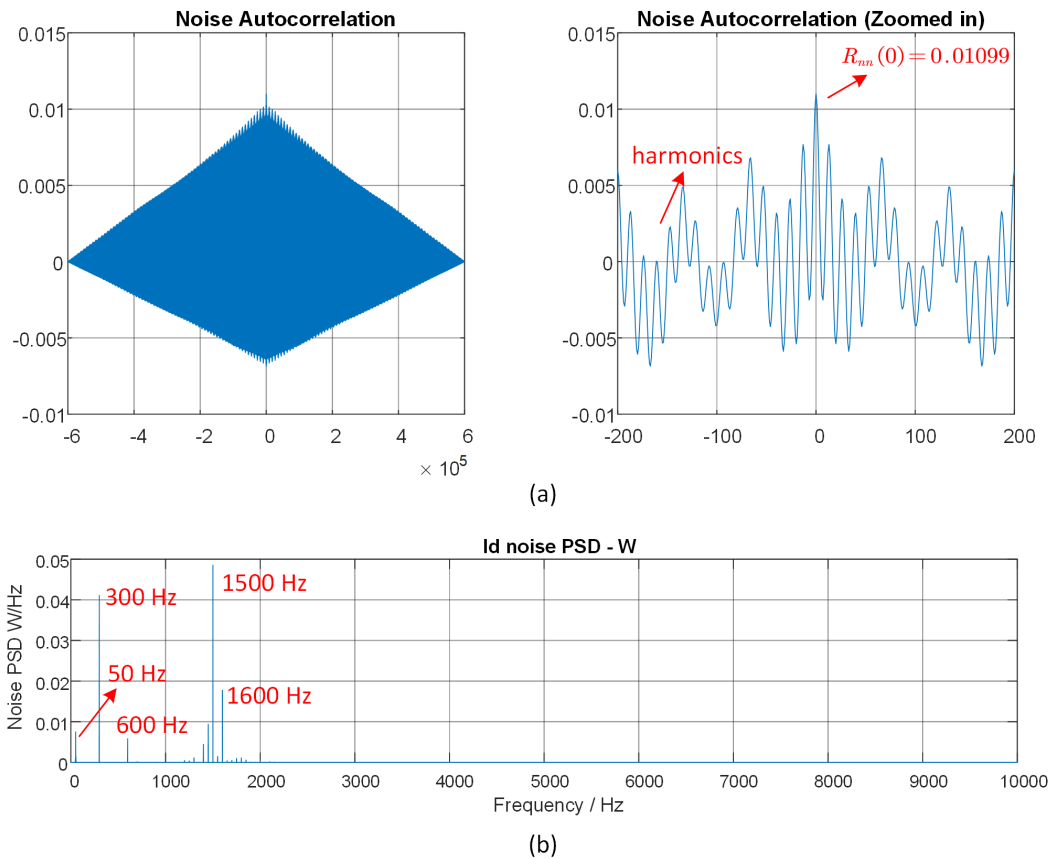


Figure 5.7: (a) Autocorrelation of the noise: the diamond shape is in accordance with the feature of WSS process. The value at 0 is 0.01099, which is the total power of the noise. Harmonics of various frequencies are seen in the autocorrelation. (b) PSD of the noise, showing the power of each harmonic.

Table 5.1: Parameters of modelled noise

frequency	Power/W	Inferred noise source
50 Hz	0.0010006	DC bias involved in d-q transform
300 Hz	0.0054798	5th and 7th harmonics
600Hz	0.0007787	11th and 13th harmonics
1400Hz	0.0005922	LCL filter
1450Hz	0.0012498	LCL filter
1500Hz	0.0064725	LCL filter
1600Hz	0.0023649	LCL filter
WGN	0.002	Background noise

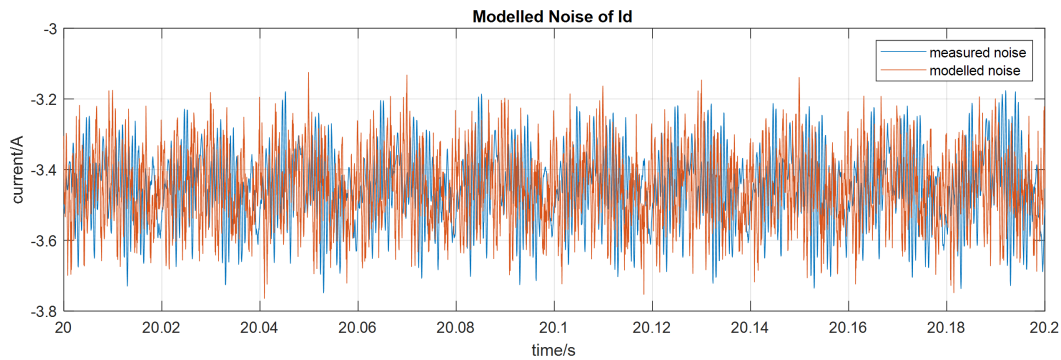


Figure 5.8: Measured noise and the modelled noise, showing that the two are closely similar.

where f_i is the frequency of the selected harmonic, and θ_i is the harmonic phase. It is seen in practice that low-order harmonics (3rd, 5th, 7th etc) tend to have a consistent phase angle with respect to the fundamental of the grid frequency. However, since this chapter aims to demonstrate a general method for noise analysis, for simplicity, the injection source is considered fully independent from the grid. Therefore, from the injection perspective, it is reasonable to assume θ_i is a uniformly randomly distributed phase in $[0, 2\pi]$.

The parameters for the modelled noise for the case studied here are given in Table 5.1, together with the inferred source of each type of noise.

The modelled noise from (5.22) is shown in Fig. 5.8. Compared with the actually measured noise, the modeled noise shows the same amplitude and very similar patterns.

C Step 3: Monte Carlo simulations

The noise model built in step 2 can be utilised to assess the noise impact on different frequency points, i.e., the probability density function (PDF) of $\sqrt{N_{c-\text{Re}}^2 + N_{c-\text{Im}}^2}$ in (5.14) for frequency point f_c . Although the impact of the PDF of the noise at different frequency points can be calculated via the mathematical expression of the noise model, the process may be difficult because the process contains multiple arcsine and integration calculations that take significant computational effort which increases with an increase in the number of harmonics of interest. Alternatively, the Monte Carlo method can be applied as a simple but effective way to analyse the noise by conducting thousands of tests in simulations from which the PDF can be estimated based on histograms of noise impact. An introduction to the Monte Carlo method is given in appendix B.8.

For each of the 81 frequency points in the present study, 2,000 random tests were performed in simulation so that histograms could be plotted. The computation time for Monte Carlo method is around 126 s in a laptop with an Intel(R) Core(TM) i7 2.20 GHz CPU. The histograms of $\sqrt{N_{\text{Re}}^2 + N_{\text{Im}}^2}$ for each frequency point are shown as a 3-D bar chart in Fig. 5.9. Four red ellipses are marked to help identify categories of noise impact in various frequency ranges. Looking at ellipse-1, the low frequency portion of the figure, the noise impacts with the highest probability density are those close to 0 impact, which means that admittance measurement at low frequency is affected very little by the noise. Further along the frequency axis, in ellipse-2, three peaks stand out, which are around 50 Hz, which means that measurement in this region will be affected by noise but the impact is maintained below 0.04 which is relatively a small value. In ellipse-3, which includes frequencies around 300 Hz, several peaks of impact occur, indicating that the noise impact will be significant and therefore a high amplitude of signal injection will be needed. This also means that such noise impact is unavoidable since the probability of noise impact being zero is nearly 0, thus this range is of major concern for the measurement process. At the high end of frequency axis, in ellipse-4, the histogram of noise impact is spread across a wide range but not far from zero, meaning that the noise could have some affect on the result but will not be severe.

Another observation is that the histogram of noise impact at different frequency points are of different shapes. This means that they can not be represented by one single type of distribution such as a normal

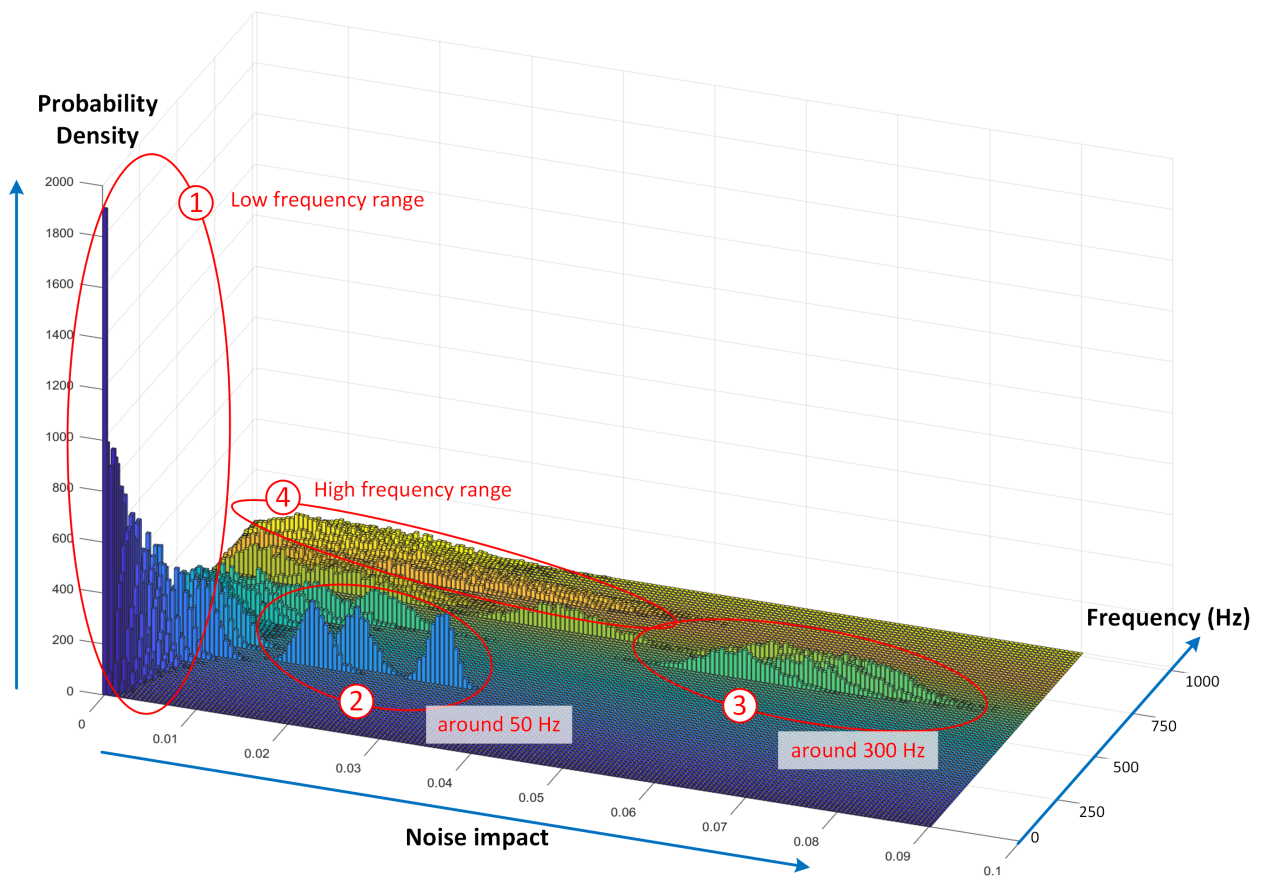


Figure 5.9: Histogram of noise impact on admittance measurements from 1 Hz to 1 kHz.

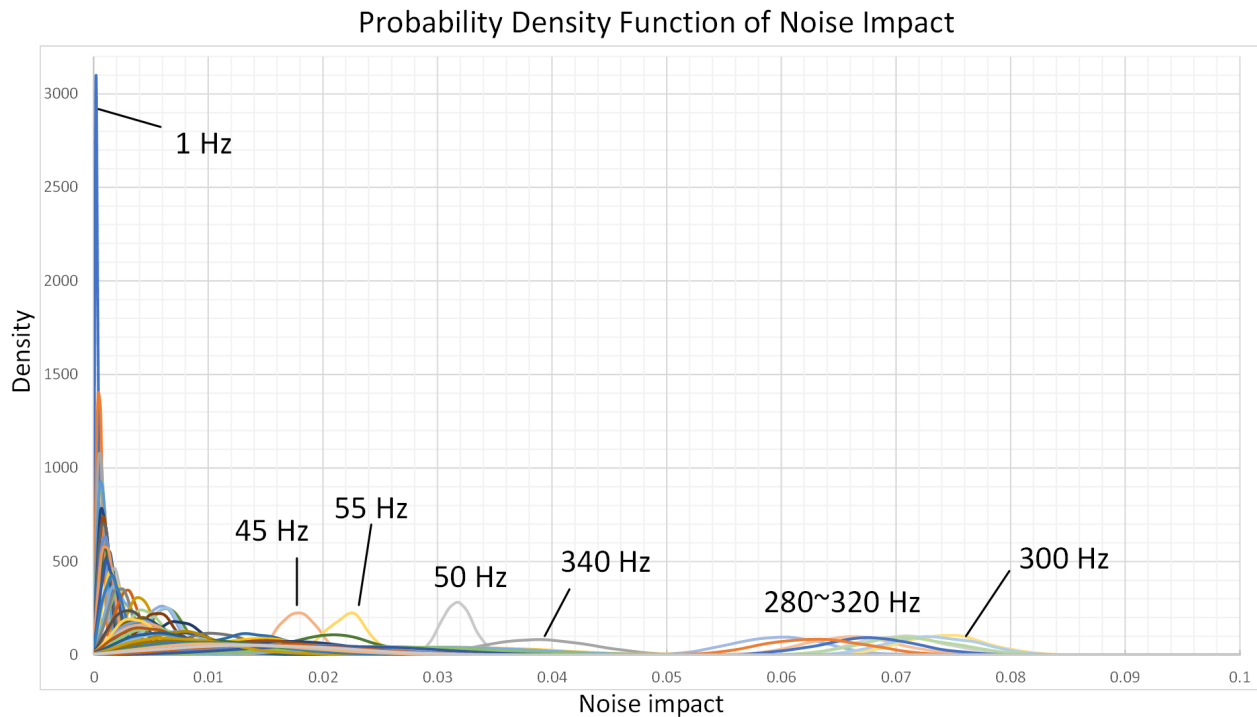


Figure 5.10: PDF of noise impact based on kernel density estimation.

distribution. As a result, kernel density estimation, which is a non-parametric way to estimate the PDF of a random variable, is applied as a generic way to acquire a PDF of noise impact. Fig. 5.10 shows the estimated PDF of noise impact on admittance measurement for the selected 81 frequencies. Where a curve has a large value of probability density, that level of impact is likely at that frequency. Peaks toward the right hand side indicate a large impact on the final measurement results or, looked at the another way, a large injection amplitude is required to obtain reasonable accuracy at these frequency points.

D Step 4: Injection guidance

A 95% probability curve of noise impact value was calculated using the PDF of noise impact and is shown in Fig. 5.11. For each frequency, there is a 95% probability that the absolute error caused by noise is smaller than the corresponding value of the curve. Here the value 95% is chosen as it is a common value in the field of statistics when considering a confidence interval. The curve in Fig. 5.11 can serve as a guide for choosing the amplitude for signal injection. Taking 300 Hz as an example, the absolute error, at 95% probability, is 0.08 or less. If the measurement is required to have a relative

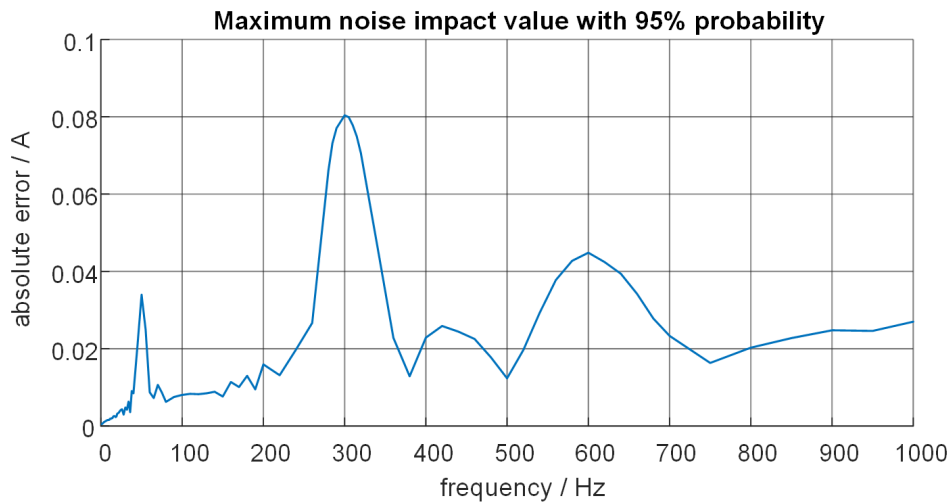


Figure 5.11: Absolute error caused by noise plotted at the 95% confidence level, i.e., there is 95% probability that the error is smaller than the value indicated by this curve.

error lower than 12%, then the current should have an amplitude $\frac{1}{0.12}$ times of the noise impact which yields a required amplitude of $\frac{0.08}{0.12} = 0.67$ A. Based on the required amplitude of the current, the necessary amplitude of voltage injection can be obtained by using knowledge of the expected range of impedance or through circuit simulations, or through undertaking a set of preliminary experiments with gradually increasing amplitude. In the experimental system under study, a voltage injection with an amplitude of 15 V is needed to drive 0.67 A of current, i.e., a 15 V amplitude of voltage injection can achieve the goal on accuracy. It is also worth mentioning that in this experiment, 15 V amplitude of voltage injection on d axis is approximately 4.3% of the steady value of v_d , which is a small fraction of the steady state value.

The four steps described above are a complete process for analysing noise impacts relevant to impedance measurement and lead to determination the minimum injection amplitude required for impedance or admittance measurement of a particular accuracy. It can be seen that through a process of measurements, modelling and analysis, guidance can be formulated which informs a proper choice of injection amplitude for the desired accuracy.

5.4 Measurement Results

Two sets of experimental tests have been performed in order to verify the preceding analysis.

5.4.1 300 Hz admittance measurement

In the first test, the frequency point 300 Hz is measured repeatedly 1,000 times. The waveforms during the measurement is captured as shown in Fig. 5.12. Each of the test comprises 7 cycles of 300 Hz sine wave with 15 V amplitude injected by the power amplifier. Two cycles are pilot cycles during which no measurements are taken and 5 cycles are used for measurement. The time interval between each test is set as a random number. The individual waveforms are described in the caption. The 15 V injected signal is barely visible on the graphs of v_a since it is a small value compared with the steady-state voltage and although not demonstrated here, it is intended to not adversely affect the operation or stability of the wider system.

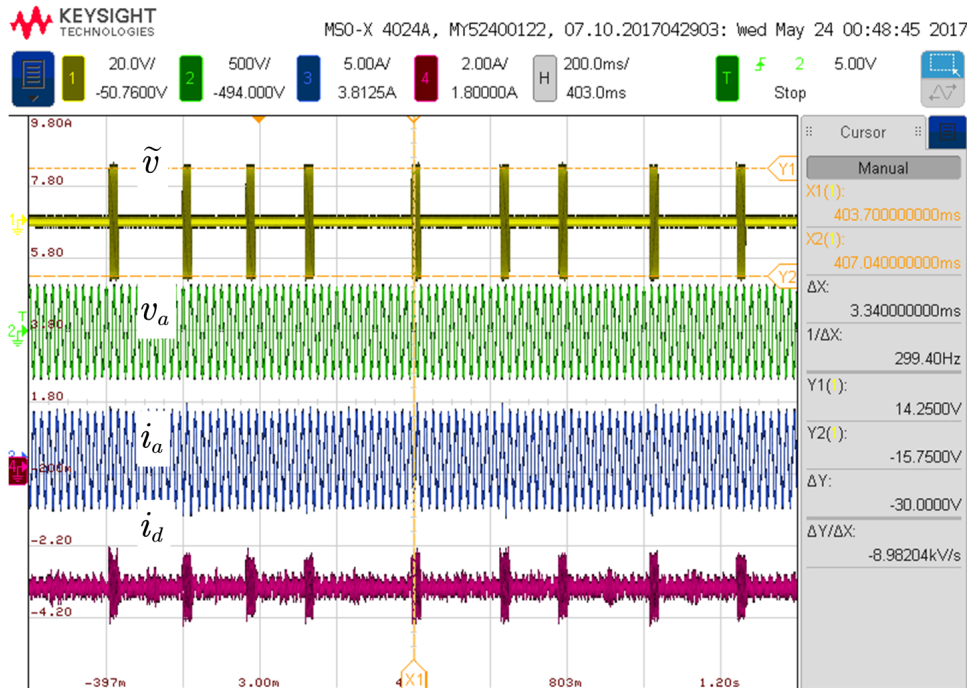
Using equation (5.17), the true value of the current response $I_{c0}(300 \text{ Hz})$ can be estimated by calculating the mean value of the measured results, such that

$$I_{c0}(300 \text{ Hz}) = 0.5250 + j0.5220 \text{ A.} \quad (5.25)$$

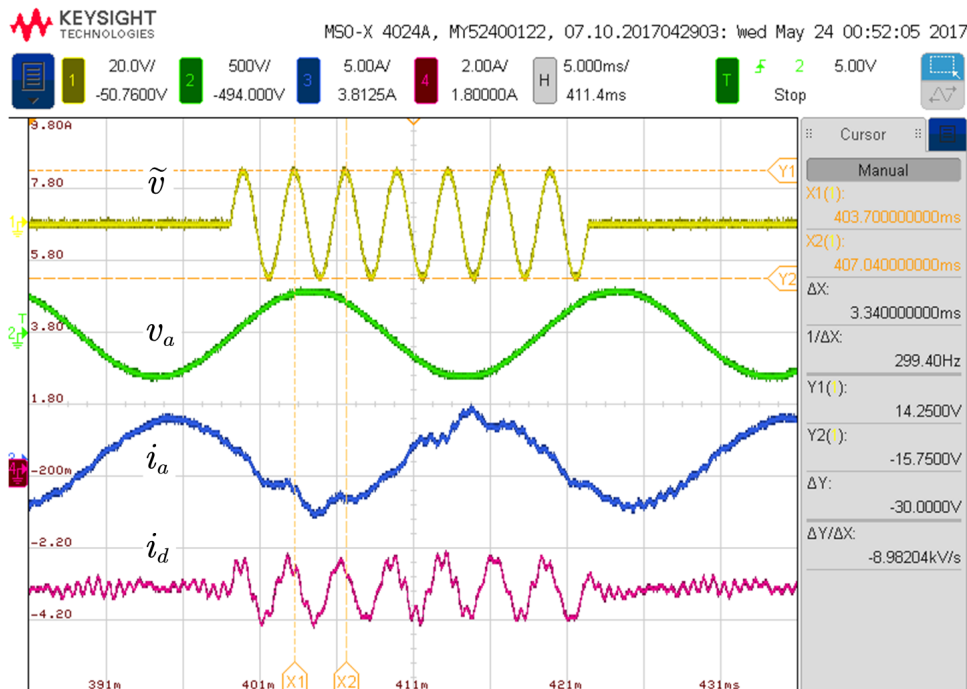
Combining (5.25) and (5.12) yields the true value of the admittance at 300 Hz

$$Y_{\text{true}}^{\text{sys}}(300 \text{ Hz}) = 0.0350 + j0.0348 \text{ S.} \quad (5.26)$$

The relative error of each test can then be calculated from the ratio of absolute error to the true value in (5.14). Fig. 5.13 shows the histogram of the relative errors from 1,000 measurements. It is clear that the error is confined within 12% under 15 V injection, which matches with the intention of the proposed method. It is also worth noting that the minimum relative error among the 1000 tests is around 8% meaning that the error at 300 Hz measurement is unavoidable. This is because the 5-th and 7-th harmonics containing in the system will be sampled and wrongly treated as part of the current response, thus cause an impact on the Fourier transform results. Eliminating such impact is considered as future work of this thesis.



(a)



(b)

Figure 5.12: Repeated tests of 300 Hz injection captured as oscilloscope screenshots. (a) A series of injections with random intervals. The yellow waveform is the injected signal on d axis voltage \tilde{v} , green is the phase-a voltage, blue is the phase-a current, magenta is the d axis current i_d . (b) Zoomed in view, showing that \tilde{v} is not obvious in the overall voltage v_a voltage, but clearly causes a current perturbation in i_a and i_d . The system is also stable during the injections.

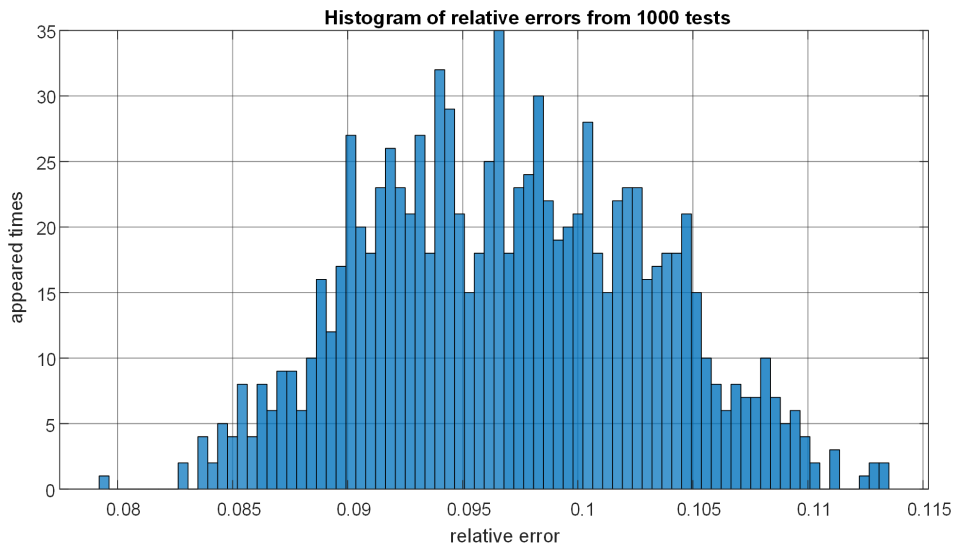


Figure 5.13: Histogram of relative errors from 1000 tests showing that the measurement errors are all confined within 12%.

5.4.2 Frequency sweep for admittance measurement

Using the preceding analysis, frequency sweeps can be executed so that Bode plots of the whole-system admittance Y^{sys} can be acquired. Fig. 5.14 shows the Bode plots acquired from frequency sweeps with various injection amplitudes. In Fig. 5.14(a), it can be seen that under 15 V injection amplitude, the measured result is a smooth curve with very small fluctuations at around 300 Hz. Knowing that 300 Hz is the major frequency point which affects the accuracy of admittance, the good results in this region prove that a 15 V injection amplitude can generate an accurate result. Fig. 5.14(b) shows the measurement result under 10 V injection. It can be seen that the fluctuation at around 300 Hz is more obvious compared with that of 15 V injection, but the measurement in other parts of the frequency range appear accurate. Fig. 5.14(c) shows results under 5 V injection, where significant errors can be observed at 300 Hz, and some fluctuations can also be observed around 50 Hz, such that the results are inaccurate. In Fig. 5.14(d) measurement results under 2 V injection show that the noise impact is severe and admittance can not be measured accurately.

From these experimental results, it can be remarked that the noise analysis method for impedance measurement developed in this chapter is effective for selecting an injection amplitude to obtain results that are not adversely affected by the noise present in the current measurement. Nonetheless, several items of work remain to be undertaken, such as testing on a more complex experimental

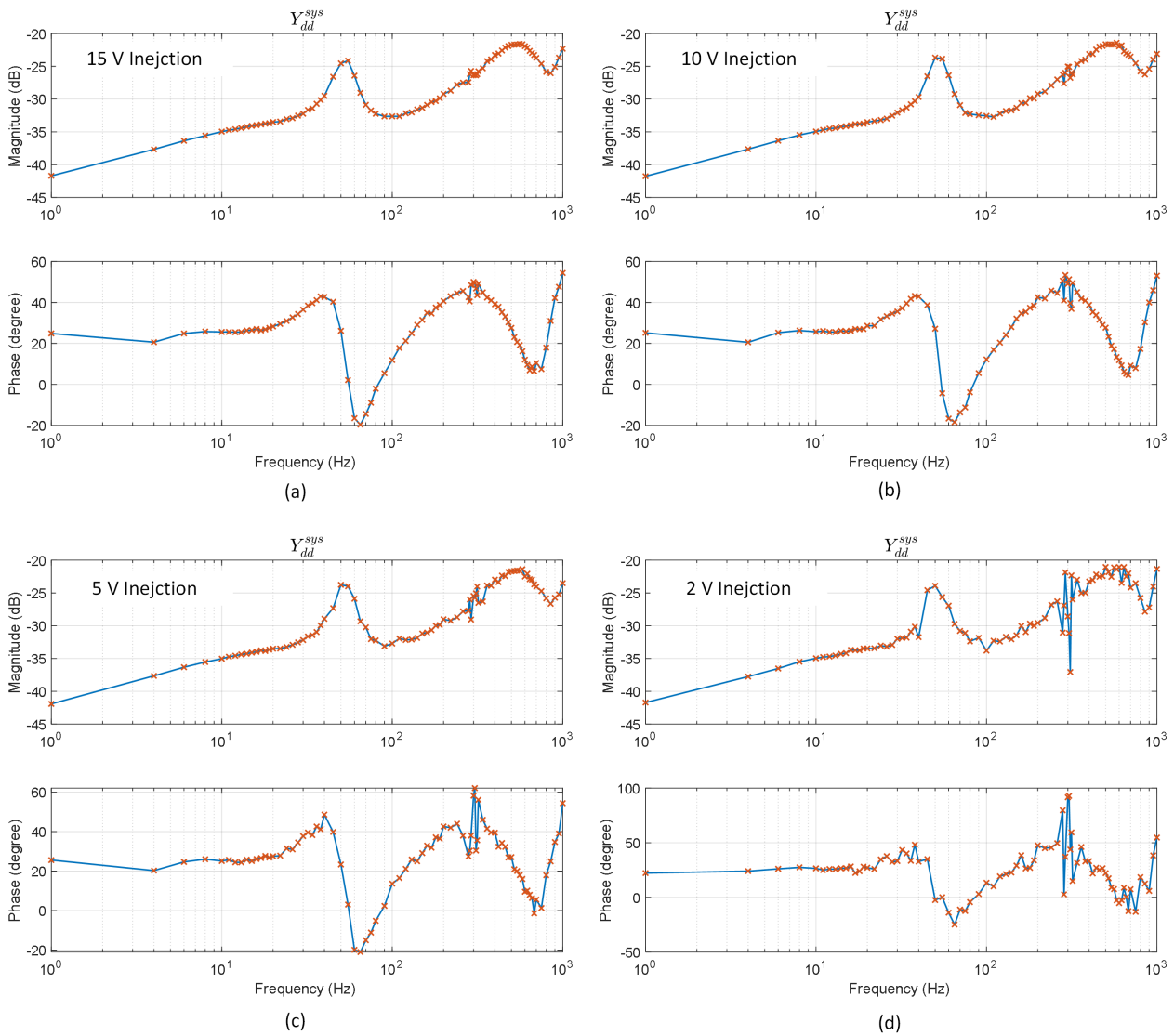


Figure 5.14: Bode plots acquired from frequency sweeps under different injection amplitude: (a) 15 V injection amplitude. (b) 10 V injection amplitude. (c) 5 V injection amplitude. (d) 2 V injection amplitude.

system containing more modes of interest, solving the remaining unavoidable measurement error caused by harmonics, adapting the injected voltage to expected impedance, and implementing vector-fitting taking this forward to the grey-box approach on measured impedance spectra. These items are viewed as future work to be undertaken in this topic.

5.5 Summary

This chapter develops a full noise analysis method which can help to determine the injection amplitude required for impedance measurement to a given accuracy. The process is based on knowledge of stochastic processes and statistics, where the Monte Carlo method is also employed to simplify the process. An impedance measurement test bench based on a PHIL technique is also built where a real hardware inverter can be connected with a real-time simulation of a power system and admittance can be measured through small-signal perturbations injected by a power amplifier.

Chapter 6

Conclusions, Publications, and Future Work

6.1 Conclusions

This thesis has addressed several major issues related to analysis and online measurement of impedance models for power system stability. The focus on impedance models came from recognition the vendors of IBR do not disclose sufficient details of their control systems to allow white-box state-space models to be formed but may disclose input-output models in impedance spectrum form or such models can be measured. The major work in this thesis can be summarised as follows:

- 1) This thesis has formalised the relationship between two forms of networked impedance models of power systems, and the relationship between impedance models and state-space models, so that the relative merits of impedance models can be clearly stated.
- 2) This thesis has, for the first time, provided a means to calculate the value of state-space eigenvalue sensitivity and impedance participation factor in impedance models, and established a comprehensive theory for root-cause analysis in impedance models. For completeness, a method of calculating the missing complex scaling factor that restores directional meaning to the previous RMA method has also been proposed.
- 3) A three-layer grey-box approach has been invented which, for large power systems for which only impedance models of apparatus are available, provides a systematic method of analysis of

small-signal stability, participation analysis and guidance for parameter tuning. The proposed grey-box approach is based on rigorous mathematical analysis with proof of the relationship between the residue of a pole and the impedance participation factor, and elucidation of the chain-rule of sensitivity propagation of internal states and parameters forward to the impedance participation factor. It thus provides a unified participation theory between state-space and impedance models.

- 4) This thesis has addressed issues related to impedance measurement error, and has developed a full noise analysis method which can help to determine the injection amplitude required for impedance measurement to a given accuracy. The process is based on knowledge of stochastic processes and statistics, where the Monte Carlo method is also employed to simplify the process. A method to validate the results and a metric to describe measurement error are also proposed.

In addition to the theoretical work, simulations and experiments have been performed to validate the proposed theories and methods. A three-node passive network, a modified IEEE 14-bus network and a modified NETS-NYPS 68-bus network were built as simulation models to verify the root-cause theory and the grey-box approach. All the codes to generate the results were written in Matlab and are published in open-source form [100], with a wish to benefit other researchers in this area. An impedance measurement test bench based on a PHIL technique was also built where a real hardware inverter can be connected with a real-time simulation of a power system and admittance can be measured through small-signal perturbations injected by a power amplifier.

6.2 List of Publications

Some of the contents in this thesis have been published during the author's PhD study, and are listed below in chronological order.

Journal Papers:

[J1] Y. Zhu, Y. Gu, Y. Li and T. C. Green, "Impedance-based Root-cause Analysis: Comparative

Study of Impedance Models and Calculation of Eigenvalue Sensitivity,” in *IEEE Transactions on Power Systems*, doi: 10.1109/TPWRS.2022.3179143.

[J2] Y. Zhu, Y. Gu, Y. Li, T. C. Green, “Participation Analysis in Impedance Models: The Grey-Box Approach for Power System Stability” in *IEEE Transactions on Power Systems*, vol. 37, no. 1, pp. 343-353, Jan. 2022, doi: 10.1109/TPWRS.2021.3088345.

[J3] Y. Li, Y. Gu, Y. Zhu, A. Junyent Ferre, X. Xiang and T. C. Green, “Impedance Circuit Model of Grid-Forming Inverter: Visualizing Control Algorithms as Circuit Elements,” in *IEEE Transactions on Power Electronics*, doi: 10.1109/TPEL.2020.3015158.

[J4] P. Ge, Y. Zhu, T. Green and F. Teng, “Resilient Secondary Voltage Control of Islanded Microgrids: An ESKBF-Based Distributed Fast Terminal Sliding Mode Control Approach,” in *IEEE Transactions on Power Systems*, doi: 10.1109/TPWRS.2020.3012026.

[J5] Y. Gu, Y. Li, Y. Zhu and T. Green, “Impedance-Based Whole-System Modeling for a Composite Grid via Embedding of Frame Dynamics,” in *IEEE Transactions on Power Systems*, doi: 10.1109/TPWRS.2020.3004377.

Conference Paper:

[C1] X. Xiang, X. Zhang, Y. Zhu, G. P. Chaffey, Y. Gu and T. C. Green, “The Resonant Modular Multilevel DC Converters for High Step-ratio and Low Step-ratio Interconnection in MVDC Distribution Network,” *IECON 2019 - 45th Annual Conference of the IEEE Industrial Electronics Society*, Lisbon, Portugal, 2019, pp. 5686-5693, doi: 10.1109/IECON.2019.8926939.

Additional papers about impedance measurement based on the work in Chapter 5 are currently in preparation.

Notes:

[J1] is the journal paper published from the work in chapter 2 and the eigenvalue sensitivity analysis in chapter 3. [J2] is the journal paper published from the participation analysis and the grey-box approach in chapter 3. [J3] and [J5] contribute to some of the underpinning ideas in impedance models in this thesis and are introduced in Chapter 1 and Chapter 2. [J4] and [C1] are from cooperation with

fellow researchers in the group where the author helped with experimental verification, and their contents are not included in this thesis.

6.3 Future Work

6.3.1 Root-cause Analysis in Hybrid Systems

With the development of high-voltage DC (HVDC) transmissions, it would be worthwhile extending impedance-based small-signal stability analysis to hybrid AC/DC systems. Some research work has explored the application of impedance models for root-cause tracing in hybrid AC/DC systems [89], but the approach is based on the RMA method hence only provides a partial solution. By extending the two-port impedance model ($d-q$) to three-port models ($d-q$ and dc), the root-cause analysis proposed in this thesis can be extended to hybrid systems. Eigenvalue sensitivity with respect to AC/DC interlink apparatus and DC apparatus could be accomplished and compared with AC apparatus. Such an extension is planned in the next stage of the research work.

6.3.2 Impedance Measurement Improvement

Recognising that this thesis has only taken a first look into impedance measurement, there is still work to be fulfilled to further verify the results. In addition, potential improvements to achieve better measurement accuracy can be envisaged.

A larger-scale test system needs to be built, in which interactions between hardware IBR and emulated power system can be established with interesting oscillatory modes to observe. Such a system can be used to verify the proposed noise analysis process in a more complicated environment.

Further, as pointed out in this thesis, the harmonics existed in the noise can cause significant measurement error. A potential solution is to predict the phase of harmonics and inject signals which are orthogonal to harmonics. In fact, low-order harmonics (3rd, 5th, 7th etc) tend to have a consistent phase angles with respect to the fundamental of the grid frequency, hence predicting the phase

of harmonics is potentially feasible. Through such a process, the impact of low-order harmonics on measurement results could perhaps be eliminated.

Additionally, a possible enhancement towards impedance measurement with required accuracy is that, noticed in Fig. 5.11, the injection amplitude in different frequency ranges could vary according to the noise impact and approximations on the admittance. For example, according to Fig. 5.11, the voltage injection amplitude could be set smaller than 15 V for frequency lower than 200 Hz and higher than 700 Hz because the noise impact in these ranges is relative small. Moreover, the injection amplitude could be set as adaptive so the amplitude is optimised as the admittance is solved. In such way, the amplitude is always as small as possible to avoid, as far as possible, exciting modes of the system, and the error is confined in the required range.

Another direction for research is to combine impedance measurement with an artificial intelligence (AI) algorithm to improve the measurement. This topic has been explored in very recent years [61] for identifying impedance at different operating points but more work could be done to optimise the measurement process. Because impedance measurement is a repeated process, and the noise environment in the grid may follow certain patterns, with the help of AI, it could be possible to make better use of ambient data, and achieve faster measurement and more accurate results with smaller injections.

Appendix A

Mathematical Proofs

A.1 Proof of one zero-valued eigenvalue

If λ is a non-repeated eigenvalue of A , the number of zero-valued eigenvalue of $Y^{\text{nodal}}(\lambda)$ does not exceed one. This can be proved by contradiction.

Assume that λ is a non-repeated eigenvalue of A and $Y^{\text{nodal}}(\lambda)$ has more than one eigenvalues equal zero. In a simple case, consider $Y^{\text{nodal}}(\lambda)$ has two zero-eigenvalues γ_1 and γ_2 . Combining the assumption with equation (2.33), we know that λ will therefore be a non-repeated root of equation $Y_{\text{det}}^{\text{nodal}}(s) = 0$.

According to property 3.1, the determinant of $Y^{\text{nodal}}(s)$ can be expressed as the following polynomial of s :

$$Y_{\text{det}}^{\text{nodal}}(s) = \prod_k \text{eig}(Y^{\text{nodal}}(s)) = \Gamma(s) \cdot \gamma_1(s) \cdot \gamma_2(s), \quad (\text{A.1})$$

where $\Gamma(s)$ is the product of all the non-zero eigenvalues of $Y^{\text{nodal}}(s)$ at $s = \lambda$, i.e., $\Gamma(\lambda) \neq 0$. Based on the assumption, at $s = \lambda$ we have $\gamma_1(\lambda) = \gamma_2(\lambda) = 0$, hence the polynomials of $\gamma_1(s)$ and $\gamma_2(s)$ can be written as

$$\begin{aligned} \gamma_1(s) &= \gamma_1'(s) \cdot (s - \lambda)^{k_1} \\ \gamma_2(s) &= \gamma_2'(s) \cdot (s - \lambda)^{k_2}, \end{aligned} \quad (\text{A.2})$$

where $\gamma'_1(s)$ and $\gamma'_2(s)$ are polynomials of s and $\gamma'_1(\lambda) \neq 0$, $\gamma'_2(\lambda) \neq 0$, k_1 and k_2 are integers and $k_1 \geq 1$, $k_2 \geq 1$. Substituting (A.2) into (A.1) yields

$$Y_{\det}^{\text{nodal}}(s) = \Gamma(s) \gamma'_1(s) \gamma'_2(s) (s - \lambda)^{k_1 + k_2}. \quad (\text{A.3})$$

Since $k_1 + k_2 \geq 2$, it is clear that λ is a repeated root of equation $Y_{\det}^{\text{nodal}}(s) = 0$, which contradicts the assumption that λ is a non-repeated root of this equation. Therefore, the number of zero-valued eigenvalues of Y^{nodal} does not exceed one.

A.2 Proof of critical admittance-eigenvalue

At a steady point (λ_0, ρ_0) , γ is the only zero eigenvalue of Y^{nodal} , and $Y_{\det}^{\text{nodal}}(s, \rho)$ can be expressed as the product of all the eigenvalues of Y^{nodal} :

$$Y_{\det}^{\text{nodal}}(\lambda_0, \rho_0) = \prod_N \text{eig}(Y^{\text{nodal}}(\lambda_0, \rho_0)) = \Gamma \cdot \gamma = 0, \quad (\text{A.4})$$

where the subscription 0 means the value before perturbation, Γ is the product of all none-zero eigenvalues of $Y^{\text{nodal}}(\lambda)$, so that Γ is a none-zero coefficient. It can be clearly seen that $Y_{\det}^{\text{nodal}}(s, \rho)$ is analytical around (λ_0, ρ_0) . Now we consider the case where a small perturbation is added on ρ_0 and the frequency point s keeps the same, the variation on Y_{\det}^{nodal} is

$$\begin{aligned} \Delta Y_{\det}^{\text{nodal}} &= \left. \frac{\partial Y_{\det}^{\text{nodal}}}{\partial \rho} \right|_{\lambda_0, \rho_0} \Delta \rho \\ &= \Gamma \Delta \gamma + \gamma \Delta \Gamma + \Delta \gamma \Delta \Gamma \approx \Gamma \Delta \gamma, \end{aligned} \quad (\text{A.5})$$

where the fact $\gamma = 0$ is applied, and the higher order infinitesimal $\Delta \gamma \Delta \Gamma$ is suppressed.

Under the same perturbation, the mode λ_0 is moved to $\lambda_0 + \Delta \lambda$. At the new steady point, the critical admittance-eigenvalue is still zero, such that

$$Y_{\det}^{\text{nodal}}(\lambda_0 + \Delta \lambda, \rho_0 + \Delta \rho) = 0 \quad (\text{A.6})$$

Applying Taylor's expansion to (A.6), and suppressing the higher orders term gives

$$\frac{\partial Y_{\det}^{\text{nodal}}}{\partial s} \Big|_{\lambda_0, \rho_0} \Delta\lambda + \frac{\partial Y_{\det}^{\text{nodal}}}{\partial \rho} \Big|_{\lambda_0, \rho_0} \Delta\rho = 0. \quad (\text{A.7})$$

Substituting (A.5) into (A.7) leads to

$$\begin{aligned} \Delta\gamma &= -\frac{1}{\Gamma} \frac{\partial Y_{\det}^{\text{nodal}}}{\partial s} \Big|_{\lambda_0, \rho_0} \Delta\lambda. \\ |\Delta\gamma| &= \left| -\frac{1}{\Gamma} \frac{\partial Y_{\det}^{\text{nodal}}}{\partial s} \Big|_{\lambda_0, \rho_0} \right| \cdot |\Delta\lambda|. \end{aligned} \quad (\text{A.8})$$

Equation (A.8) proves that when there's a small variation on ρ , $|\Delta\gamma|$ is proportional to $|\Delta\lambda|$, so that $\Delta\gamma$ could reflect how parameters will affect the mode λ .

A.3 Proof of Lemma 1

A reduced case is first proved where G_ρ is a scalar transfer function and the pole λ is a zero of $H_\rho = G_\rho^{-1}$, that is,

$$H_\rho(\lambda) = 0. \quad (\text{A.9})$$

A perturbation in ρ induces a corresponding perturbation in λ , that is

$$H_{\rho+\Delta\rho}(\lambda + \Delta\lambda) = 0. \quad (\text{A.10})$$

Since H_ρ is analytic around its zero λ , we have the following first-order Taylor expansion of (A.10)

$$H_{\rho+\Delta\rho}(\lambda) + H'_{\rho+\Delta\rho}(\lambda)\Delta\lambda = 0 \quad (\text{A.11})$$

in which H' represents the derivative of H . Combining (A.9)-(A.11) yields

$$H_{\rho+\Delta\rho}(\lambda) - H_\rho(\lambda) + H'_\rho(\lambda)\Delta\lambda + (H'_{\rho+\Delta\rho}(\lambda) - H'_\rho(\lambda)) \Delta\lambda = 0 \quad (\text{A.12})$$

and equivalently

$$\Delta H_\rho(\lambda) + H'_\rho(\lambda)\Delta\lambda + \Delta H'_\rho(\lambda)\Delta\lambda = 0. \quad (\text{A.13})$$

Suppressing the high-order infinitesimal $\Delta H'_\rho(\lambda)\Delta\lambda$ in (A.13) yields

$$\Delta\lambda = -H'_\rho(\lambda)^{-1} \cdot \Delta H_\rho(\lambda). \quad (\text{A.14})$$

As λ is a non-repeated pole for G_ρ , the residue of G_ρ at λ is

$$\text{Res}_\lambda G_\rho = \lim_{s \rightarrow \lambda} (s - \lambda)G_\rho(s) = \lim_{s \rightarrow \lambda} \frac{s - \lambda}{H_\rho(s)} = \frac{1}{H'_\rho(\lambda)} \quad (\text{A.15})$$

in which the second equal sign results from L'Hôpital's rule. Combining (A.14) and (A.15) yields

$$\Delta\lambda = -\text{Res}_\lambda G_\rho \cdot \Delta H_\rho(\lambda). \quad (\text{A.16})$$

This is the reduced case of Lemma 1 with G_ρ being a scalar transfer function.

Now we prove the case where G_ρ is a square matrix and the pole λ is a zero for the determinant of H_ρ , that is,

$$\det(H_\rho(\lambda)) = 0. \quad (\text{A.17})$$

We take $\det(H_\rho) \triangleq H_{\det}$ as a scalar transfer function so a similar result to (A.14) is obtained

$$\Delta\lambda = -H'_{\det}(\lambda)^{-1} \Delta H_{\det}(\lambda). \quad (\text{A.18})$$

Expanding H_{\det} along a column yields

$$H_{\det} = \sum_h H_{\rho hl} F_{\rho hl} \quad (\text{A.19})$$

in which F_ρ is the cofactor matrix for H_ρ and the subscript hl denotes the element in a matrix at the h -th row and l -th column. It is clear to see from (A.19) that

$$\frac{\partial H_{\det}}{\partial H_{\rho hl}} = F_{\rho hl} \quad (\text{A.20})$$

and hence

$$\begin{aligned}\Delta H_{\det} &= \sum_{h,l} \frac{\partial H_{\det}}{\partial H_{\rho hl}} \Delta H_{\rho hl} \\ &= \sum_{h,l} F_{\rho hl} \Delta H_{\rho hl} = \langle \overline{F}_{\rho}, \Delta H_{\rho} \rangle\end{aligned}\tag{A.21}$$

where the complex conjugate $\overline{\cdot}$ is associated with the Frobenius inner product $\langle \cdot, \cdot \rangle$ for complex matrices defined in (B.4).

Since G_{ρ} is now a matrix, its residue needs to be calculated element-wise

$$\begin{aligned}\text{Res}_{\lambda} G_{\rho} &= \lim_{s \rightarrow \lambda} (s - \lambda) G_{\rho}(s) \\ &= \lim_{s \rightarrow \lambda} ((s - \lambda) H_{\rho}(s)^{-1}) \\ &= \lim_{s \rightarrow \lambda} \left(\frac{s - \lambda}{H_{\det}(s)} F_{\rho}(s)^{\top} \right) = \frac{F_{\rho}(\lambda)^{\top}}{H'_{\det}(\lambda)}\end{aligned}\tag{A.22}$$

where we make use of the fact that

$$H_{\rho}(s)^{-1} = F_{\rho}(s)^{\top} / H_{\det}(s).\tag{A.23}$$

Combining (A.18), (A.21) and (A.22) yields Lemma 1

$$\begin{aligned}\Delta \lambda &= -H'_{\det}(\lambda)^{-1} \langle \overline{F_{\rho}(\lambda)}, \Delta H_{\rho}(\lambda) \rangle \\ &= \langle -\overline{\text{Res}_{\lambda} G_{\rho}}^{\top}, \Delta H_{\rho}(\lambda) \rangle = \langle -\text{Res}_{\lambda}^* G_{\rho}, \Delta H_{\rho}(\lambda) \rangle.\end{aligned}\tag{A.24}$$

A.4 Proof of Eigenvalue Sensitivity Matrix

Expanding $Y_{\det}^{\text{nodal}}(\lambda)$ along row k yields

$$Y_{\det}^{\text{nodal}}(\lambda) = \sum_{i=1}^n Y_{ki}^{\text{nodal}} C_{ki},\tag{A.25}$$

where C_{ki} is the cofactor of Y_{ki}^{nodal} . According to (A.25) it is clear to have

$$\frac{\partial Y_{\text{det}}^{\text{nodal}}(\lambda)}{\partial Y_{ki}^{\text{nodal}}} = C_{ki}. \quad (\text{A.26})$$

Considering a small perturbation is added on a system parameter ρ , leading to a perturbation on Y_{ki}^{nodal} and λ , i.e.

$$\begin{aligned} Y_{ki}^{\text{nodal}} &= Y_{ki0}^{\text{nodal}} + \Delta Y_{ki}^{\text{nodal}} \\ \lambda &= \lambda_0 + \Delta\lambda, \end{aligned} \quad (\text{A.27})$$

where the subscript 0 refers to the value before perturbation. At the new steady state, the eigenvalue λ still satisfies (2.33), hence we have

$$Y_{\text{det}}^{\text{nodal}}(\lambda, Y_{ki}^{\text{nodal}}) = Y_{\text{det}}^{\text{nodal}}(\lambda_0 + \Delta\lambda, Y_{ki0}^{\text{nodal}} + \Delta Y_{ki}^{\text{nodal}}) = 0. \quad (\text{A.28})$$

Since $Y_{\text{det}}^{\text{nodal}}$ is analytical around its zero λ , applying the first-order Taylor expansion to (A.28) and suppressing the high-order of infinitesimal items yields

$$\frac{\partial Y_{\text{det}}^{\text{nodal}}(\lambda)}{\partial Y_{ki}^{\text{nodal}}} \Delta Y_{ki}^{\text{nodal}} + Y_{\text{det}}^{\text{nodal}'}(\lambda) \Delta\lambda = 0, \quad (\text{A.29})$$

where

$$Y_{\text{det}}^{\text{nodal}'}(\lambda) \triangleq \left. \frac{dY_{\text{det}}^{\text{nodal}}(s)}{ds} \right|_{s=\lambda}. \quad (\text{A.30})$$

Substituting (A.26) into (A.29) yields the result of $\frac{\partial\lambda}{\partial Y_{ki}}$

$$\frac{\Delta\lambda}{\Delta Y_{ki}^{\text{nodal}}} = \frac{\partial\lambda}{\partial Y_{ki}^{\text{nodal}}} = S_{\lambda,ik} = -\frac{C_{ki}}{Y_{\text{det}}^{\text{nodal}'}(\lambda)}, \quad (\text{A.31})$$

where C is the cofactor matrix of $Y^{\text{nodal}}(\lambda)$ and C_{ki} is its element. S_{λ} can then be deduced as

$$S_{\lambda} = -\frac{1}{Y_{\text{det}}^{\text{nodal}'}(\lambda)} C^{\top} = -\frac{1}{Y_{\text{det}}^{\text{nodal}'}(\lambda)} \text{adj}(Y^{\text{nodal}}(\lambda)). \quad (\text{A.32})$$

A.5 proof of equation (3.31)

Since λ is considered as a non-repeated eigenvalue of the system, for a system with n nodes, the rank of $Y^{\text{nodal}}(\lambda)$ is $n - 1$, hence $Y^{\text{nodal}}(\lambda)$ has one and only one zero-eigenvalue γ . Accordingly, the rank of its adjugate matrix $\text{adj}(Y^{\text{nodal}}(\lambda))$ is 1, with only one non-zero-eigenvalue γ^\dagger . It is known that rank-1 matrix can be expressed as the outer product of two vectors, such that

$$\text{adj}(Y^{\text{nodal}}(\lambda)) = u_s \otimes w_s = u_s w_s^\top, \quad (\text{A.33})$$

where u_s and w_s are two column-vectors of n -order. Now we prove u_γ , which is the right eigenvector of $Y^{\text{nodal}}(\lambda)$ corresponding to γ , is proportional to x .

For γ^\dagger we have

$$\text{adj}(Y^{\text{nodal}}(\lambda)) \cdot u_\gamma^\dagger = \gamma^\dagger \cdot u_\gamma^\dagger, \quad (\text{A.34})$$

where u_γ^\dagger is a non-zero right-eigenvector corresponding to γ^\dagger . Left-multiplying Y^{nodal} in (A.34) and rearranging the equation yields

$$Y^{\text{nodal}}(\lambda) \cdot u_\gamma^\dagger = 0 \cdot u_\gamma^\dagger, \quad (\text{A.35})$$

where we use fact $Y^{\text{nodal}}(\lambda) \cdot \text{adj}(Y^{\text{nodal}}(\lambda)) = I \cdot Y_{\text{det}}(\lambda) = 0$, and I is an identity matrix. (A.35) proves that u_γ^\dagger is also a right-eigenvector of $Y^{\text{nodal}}(\lambda)$ corresponding to γ , i.e., the non-zero eigenvectors u_γ^\dagger and u_γ are linear combinations of each other. Reversely, u_γ is also the right eigenvector of $\text{adj}(Y^{\text{nodal}}(\lambda))$ corresponding to γ^\dagger . Combined with (A.33) it is clear to have

$$\begin{aligned} \text{adj}(Y^{\text{nodal}}(\lambda)) \cdot u_\gamma &= u_s w_s^\top u_\gamma = \gamma^\dagger \cdot u_\gamma \\ u_s &= \frac{\gamma^\dagger}{w_s^\top u_\gamma} \cdot u_\gamma. \end{aligned} \quad (\text{A.36})$$

Since $\frac{\gamma^\dagger}{w_s^\top u_\gamma}$ is a scalar, u_s is proportional to u_γ . Similarly, we can prove w_s^\top is proportional to w_γ^\top . As a result,

$$u_s w_s^\top = \eta \cdot u_\gamma w_\gamma^\top, \quad (\text{A.37})$$

where η is a scalar. From (A.33) it is clear that

$$\text{tr}(\text{adj}(Y^{\text{nodal}}(\lambda))) = w_s^\top u_s = \eta \cdot w_\gamma^\top u_\gamma. \quad (\text{A.38})$$

Because u_γ and w_γ are normalized as $w_\gamma^\top u_\gamma = 1$, $\eta = \text{tr}(\text{adj}(Y^{\text{nodal}}(\lambda)))$. Substituting η into (A.37) yields equation (3.31).

A.6 proof of Premise 5.3

The Gaussian noise in this system is mainly caused by thermal noise in electronic system and is usually assumed as WGN with mean of zero [136]. WGN is originally recognised as a WSS process.

Now we prove that an harmonic $H_i(t)$ is also a WSS process. An harmonic $H_i(t)$ can be expressed as

$$H_i(t) = A_i \sin(2\pi f_i t + \theta_i), \quad \theta_i \sim U(0, 2\pi), \quad (\text{A.39})$$

where A_i is the amplitude, f_i is harmonic frequency, θ_i is the phase and also a random variable with uniform distribution on $(0, 2\pi)$. Based on law of the unconscious statistician, the expected value of $H_i(t)$ can be calculated as

$$E(H_i(t)) = \int_0^{2\pi} \frac{A_i}{2\pi} \sin(2\pi f_i t + \theta_i) d\theta_i = 0. \quad (\text{A.40})$$

Therefore, the expected value of $H_i(t)$ is 0 is independent of t . Meanwhile, the autocorrelation of $H_i(t)$ can be calculated as

$$\begin{aligned} R_{H_i H_i}(\tau) &= \int_0^{2\pi} H_i(t) H_i(t - \tau) dt \\ &= A_i^2 \int_0^{2\pi} \sin(2\pi f_i t + \theta_i) \cdot \sin(2\pi f_i t + \theta_i - 2\pi f_i \tau) dt \\ &= -\frac{A_i^2}{2} \int_0^{2\pi} \cos(4\pi f_i t + 2\theta_i - 2\pi f_i \tau) dt + \frac{A_i^2}{2} \int_0^{2\pi} \cos(2\pi f_i \tau) dt \\ &= A_i^2 \pi \cos(2\pi f_i \tau). \end{aligned} \quad (\text{A.41})$$

(A.41) proves that the autocorrelation of $H_i(t)$ is a function only of the time difference τ . Based on the definition of WSS in Appendix B.4, $H_i(t)$ is a WSS process.

Based on the above, the noise, which is summation of WGN and harmonics, is a WSS process.

Appendix B

Mathematical Preliminaries

We summarise the mathematical preliminaries used in this paper to assist the reader and to make the paper self-contained.

B.1 Residue

In complex analysis, the residue of a complex function $G(s)$ is defined as the g_{-1} coefficient of the Laurent series [137] of $G(s)$. This is, given the Laurent series of $G(s)$ around λ

$$G(s) = \sum_{h=-\infty}^{\infty} g_h \cdot (s - \lambda)^h \quad (\text{B.1})$$

the residue of G at λ is defined as

$$\text{Res}_\lambda G = g_{-1}. \quad (\text{B.2})$$

If λ is a non-repeated pole of G , the residue is found from

$$\text{Res}_\lambda G = \lim_{s \rightarrow \lambda} (s - \lambda)G(s). \quad (\text{B.3})$$

This property is used in the proof of Lemma 1 in Appendix B. The residue can be applied element-wise on a matrix of complex functions.

B.2 Frobenius Inner Product

For two complex-valued matrices V and W with the same dimension, the Frobenius inner product [138] of V and W is defined as

$$\langle V, W \rangle \triangleq \sum_{h,l} \bar{V}_{hl} W_{hl} \quad (\text{B.4})$$

where h and l are the row and column indices of the matrices, and $\bar{}$ denotes complex conjugation.

The complex conjugation in (B.4) ensures that the Frobenius inner product of a complex matrix with itself is a non-negative real number, and thus is induced the Frobenius norm $\|\cdot\|$

$$\|V\| \triangleq \sqrt{\langle V, V \rangle}. \quad (\text{B.5})$$

The Frobenius inner product and norm are derived from the common inner product in vector spaces, so the properties of the common inner product are naturally inherited. One of the most useful properties is the Cauchy inequality

$$|\langle V, W \rangle| \leq \|V\| \cdot \|W\| \quad (\text{B.6})$$

where the equality holds if and only if V and W are aligned in orientation. This property is used in (3.45) in Section III-C.

B.3 Complex Function Derivative

In this thesis we use two types of derivatives for complex functions. The first type of derivative is the derivative of a complex function over a real number, e.g. derivative of a transfer function over its internal parameter ρ , $\partial H_\rho(s)/\partial \rho$. This type of derivative is the same as a real-function derivative with the real part and complex part of $H_\rho(s)$ treated separately. The second type of derivative is the derivative of a complex function over another complex number, e.g. a transfer function over another transfer function, $\partial H/\partial G$. For such a case, the mapping from G to H has to be analytic so that $\partial H/\partial G$ exists. For the scope of this paper, most complex-to-complex mappings are analytic throughout the complex plane except at poles so the derivative is almost always proper. As a special

case, the derivative of a transfer function H over its complex argument s is called H' , that is,

$$H'(s) \triangleq \partial H(s)/\partial s. \quad (\text{B.7})$$

Both the complex and real derivatives can be applied to vectors and matrices with each element of the vectors and matrices treated as independent variables, and the resulted derivative is also a vector or matrix.

B.4 Wide-sense stationary stochastic process

Wide-sense stationary (WSS) process, sometimes also known as weak-sense stationary process, is a case of stationary process but not that restrictive. For a continuous-time random process $\{X(t), t \in \mathbb{R}\}$, $X(t)$ is a WSS process if

- 1) $E_X(t) = E_X$, for all $t \in \mathbb{R}$.
- 2) $R_{XX}(t_1, t_2) = R_{XX}(t_1 - t_2)$, for all $t_1, t_2 \in \mathbb{R}$.

The first condition means that $X(t)$ has a constant expectation value independent of t . The second condition means that its autocorrelation is a function only of the time difference $t_2 - t_1$, but independent of t_1 or t_2 . The above is defined for continuous-time process but the same conditions can also be extended to discrete-time process in the same manner.

B.5 Law of large numbers

From the law of large numbers, the average of the results obtained from a large number of trials should be close to the expected value and tends to become closer to the expected value as more trials are performed. Let X be a random variable with finite expected value $E(X)$ and finite non-zero variance σ^2 ,

$$\lim_{n \rightarrow \infty} \frac{1}{n} (X_1 + X_2 + \cdots + X_n) = E(X) \quad (\text{B.8})$$

B.6 Autocorrelation

Autocorrelation is the correlation of a signal with a delayed copy of itself as a function of delay [139]. It can help analyse the repeating patterns of signals such as noise.

For a continuous stochastic process $x(t)$, its autocorrelation $R_{xx}(\tau)$ can be calculated as

$$R_{xx}(\tau) = \int_{-\infty}^{\infty} x(t) \overline{x(t-\tau)} dt, \quad (\text{B.9})$$

where τ is the delay, and the bar represents conjugate complex. This is equivalent as the cross-correlation of $x(t)$ and itself. It is worth noting that if $x(t)$ is a continuous periodic function of period T , the integration period can be replaced by a period of length T , instead of from $-\infty$ to ∞ . And for measured noise with limited length, we can do periodic extension on the signal to treat it as periodic function.

Similarly, for discrete-time signal $x(n)$, its autocorrelation is

$$R_{xx}(l) = \sum_{n \in Z} x(n) \overline{x(n-l)}, \quad (\text{B.10})$$

where Z is the set of integers.

An important property for autocorrelation is that if $x(t)$ is a WSS process, its autocorrelation at $\tau = 0$ is the average power of $x(t)$, such that

$$R_{xx}(0) = E(x^2(t)). \quad (\text{B.11})$$

B.7 Wiener–Khinchin theorem

Wiener–Khinchin theorem states that for a WSS process $x(t)$ with autocorrelation function $R_{xx}(\tau)$, the Fourier transform of $R_{xx}(\tau)$ denotes the power spectral density (PSD) of $x(t)$, such that

$$S(f) = \int_{-\infty}^{\infty} R_{xx}(\tau) e^{-j2\pi f\tau} d\tau. \quad (\text{B.12})$$

B.8 Monte Carlo Method

So far, there is no consensus on how Monte Carlo should be defined [140]. The general principle can be understood as an algorithm using massive repeated random sampling to obtain numerical results. In this experiment, after determining the random variables of the noise, the process of impedance measurement can be emulated in the simulation for a number of times which gives the histogram of noise impact. In each simulation, random values are chosen based on the distributions of the random variables. When the repeated number is large, the histogram of noise impact will be very close to its probability density, such that the probability density function can be acquired by curve fitting.

Appendix C

Mathematical Illustrations

C.1 Illustration of LEMMA 1

We use a simple three-node system to illustrate Lemma 1. The whole-system impedance of this three-node system is

$$Y^{\text{sys}} = \begin{bmatrix} Y_{11}^{\text{sys}} & Y_{12}^{\text{sys}} & Y_{13}^{\text{sys}} \\ Y_{21}^{\text{sys}} & Y_{22}^{\text{sys}} & Y_{23}^{\text{sys}} \\ Y_{31}^{\text{sys}} & Y_{32}^{\text{sys}} & Y_{33}^{\text{sys}} \end{bmatrix} \quad (\text{C.1})$$

where each entry of Y^{sys} is a 2×2 transfer function matrix in dq frame. For instance, the first diagonal element is

$$Y_{11}^{\text{sys}} = \begin{bmatrix} Y_{11,dd}^{\text{sys}}(s) & Y_{11,dq}^{\text{sys}}(s) \\ Y_{11,qd}^{\text{sys}}(s) & Y_{11,qq}^{\text{sys}}(s) \end{bmatrix} \quad (\text{C.2})$$

which represents the whole-system admittance measured at the first node. Each element in Y_{11}^{sys} can be expressed as the sum of a series of pole-residue pairs, for example, $Y_{11,dd}^{\text{sys}}$ is

$$Y_{11,dd}^{\text{sys}}(s) = \frac{R_{11,1}^{dd}}{s - \lambda_1} + \frac{R_{11,2}^{dd}}{s - \lambda_2} + \cdots + \frac{R_{11,m}^{dd}}{s - \lambda_m} \quad (\text{C.3})$$

where $R_{11,i}^{dd}$ is the residue of $Y_{11,dd}^{\text{sys}}$ at the i -th pole (eigenvalue) λ_i for $i \in \{1, 2, \dots, m\}$. The residue of Y_{11}^{sys} at a particular pole λ (subscript i is dropped for brevity) is then given by

$$\text{Res}_{\lambda} Y_{11}^{\text{sys}} = \begin{bmatrix} R_{11,dd} & R_{11,dq} \\ R_{11,qd} & R_{11,qq} \end{bmatrix}. \quad (\text{C.4})$$

For a parameter perturbation $\Delta\rho$ in the apparatus at the first node, the corresponding admittance perturbation of this apparatus is

$$\Delta Z_1(\lambda) = \frac{\partial Z_1(\lambda)}{\partial \rho} \cdot \Delta\rho = \begin{bmatrix} \Delta Z_1^{dd} & \Delta Z_1^{dq} \\ \Delta Z_1^{qd} & \Delta Z_1^{qq} \end{bmatrix} \quad (\text{C.5})$$

which yields

$$\begin{aligned} \Delta\lambda &= \langle -\text{Res}_{\lambda}^* Y_{11}^{\text{sys}}, \Delta Z_1(\lambda) \rangle \\ &= -(R_{11,dd} \Delta Z_1^{dd} + R_{11,qd} \Delta Z_1^{dq} + R_{11,dq} \Delta Z_1^{qd} + R_{11,qq} \Delta Z_1^{qq}) \end{aligned} \quad (\text{C.6})$$

according to Lemma 1. $\Delta\lambda$ is a complex number whose direction is determined jointly by $-\text{Res}_{\lambda}^* Y_{11}^{\text{sys}}$ and $\Delta Z_1(\lambda)$.

Appendix D

System Data

D.1 Modified IEEE 14-bus System

This appendix gives the detailed parameters of the modified 14-bus system studied in this paper. The parameters of the synchronous generators are from the dynamic model built by KIOS centre at University of Cyprus [101]. The full data is attached below.

Attachment: IEEE 14-BUS MODIFIED TEST SYSTEM DATA

Nomenclature

Rated MVA	Machine-rated MVA; base MVA for impedances
Rated kV	Machine-rated terminal voltage in kV; base kV for impedances
H	Inertia constant in s
D	Machine load damping coefficient
r_a	Armature resistance in p.u.
x_d	Unsaturated d axis synchronous reactance in p.u.
x_q	Unsaturated q axis synchronous reactance in p.u.
x'_d	Unsaturated d axis transient reactance in p.u.
x'_q	Unsaturated q axis transient reactance in p.u.
x''_d	Unsaturated d axis subtransient reactance in p.u.
x''_q	Unsaturated q axis subtransient reactance in p.u.
x_l or x_p	Leakage or Potier reactance in p.u.
T'_{d0}	d axis transient open circuit time constant in s
T'_{q0}	q axis transient open circuit time constant in s
T''_{d0}	d axis subtransient open circuit time constant in s
T''_{q0}	q axis subtransient open circuit time constant in s
$S(1.0)$	Machine saturation at 1.0 p.u. voltage in p.u.
$S(1.2)$	Machine saturation at 1.2 p.u. voltage in p.u.
T_r	Regulator input filter time constant in s
K_a	Regulator gain (continuous acting regulator) in p.u.
T_a	Regulator time constant in s
V_{Rmax}	Maximum regulator output, starting at full load field voltage in p.u.
V_{Rmin}	Minimum regulator output, starting at full load field voltage in p.u.
K_e	Exciter self-excitation at full load field voltage in p.u.
T_e	Exciter time constant in s
K_f	Regulator stabilizing circuit gain in p.u.
T_f	Regulator stabilizing circuit time constant in s
E_1	Field voltage value,1 in p.u.
$SE(E_1)$	Saturation factor at E_1
E_2	Field voltage value,2 in p.u.
$SE(E_2)$	Saturation factor at E_2
P_{max}	Maximum turbine output in p.u.
R	Turbine steady-state regulation setting or droop in p.u.
T_1	Control time constant (governor delay) in s
T_2	Hydro reset time constant in s
T_3	Servo time constant in s
T_4	Steam valve bowl time constant in s
T_5	Steam reheat time constant in s
F	Shaft output ahead of reheater in p.u.

TABLE I
IEEE 14-BUS MODIFIED TEST SYSTEM MACHINE DATA

Type Operation	GENROU Sync. Gen.	GENROU Sync. Gen.	GENROU Condenser	GENROU Condenser
Default Unit no. (New Unit no.)	1(15)	2(16)	3(17)	6(19), 8(18)
Rated power (MVA)	448	100	40	25
Rated voltage (kV)	22	13.8	13.8	13.8
Rated pf	0.85	0.8	0.0	0.0
H (s)	2.656	4.985	1.520	1.200
D	2.000	2.000	0.000	0.000
r_a (p.u)	0.0043	0.0035	0.000	0.0025
x_d (p.u)	1.670	1.180	2.373	1.769
x_q (p.u)	1.600	1.050	1.172	0.855
x'_d (p.u)	0.265	0.220	0.343	0.304
x'_q (p.u)	0.460	0.380	1.172	0.5795
x''_d (p.u)	0.205	0.145	0.231	0.2035
x''_q (p.u)	0.205	0.145	0.231	0.2035
x_l or x_p (p.u)	0.150	0.075	0.132	0.1045
T'_{d0} (s)	0.5871	1.100	11.600	8.000
T'_{q0} (s)	0.1351	0.1086	0.159	0.008
T''_{d0} (s)	0.0248	0.0277	0.058	0.0525
T''_{q0} (s)	0.0267	0.0351	0.201	0.0151
$S(1.0)$	0.091	0.0933	0.295	0.304
$S(1.2)$	0.400	0.4044	0.776	0.666

TABLE II
IEEE 14-BUS MODIFIED TEST SYSTEM EXCITER DATA

Type	IEEET1	IEEET1	IEEET1	IEEET1
Default Unit no. (New Unit no.)	1(15)	2(16)	3(17)	6(19), 8(18)
Rated power (MVA)	448	100	40	25
Rated voltage (kV)	22	13.8	13.8	13.8
T_r (s)	0.000	0.060	0.000	0.000
K_a (p.u)	50	25	400	400
T_a (s)	0.060	0.200	0.050	0.050
V_{Rmax} (p.u)	1.000	1.000	6.630	4.407
V_{Rmin} (p.u)	-1.000	-1.000	-6.630	-4.407
K_e (p.u)	-0.0465	-0.0582	-0.170	-0.170
T_e (s)	0.520	0.6544	0.950	0.950
K_f (p.u)	0.0832	0.105	0.040	0.040
T_f (s)	1.000	0.350	1.000	1.000
E_1 (p.u)	3.240	2.5785	6.375	4.2375
$SE(E_1)$	0.072	0.0889	0.2174	0.2174
E_2 (p.u)	4.320	3.438	8.500	5.650
$SE(E_2)$	0.2821	0.3468	0.9388	0.9388

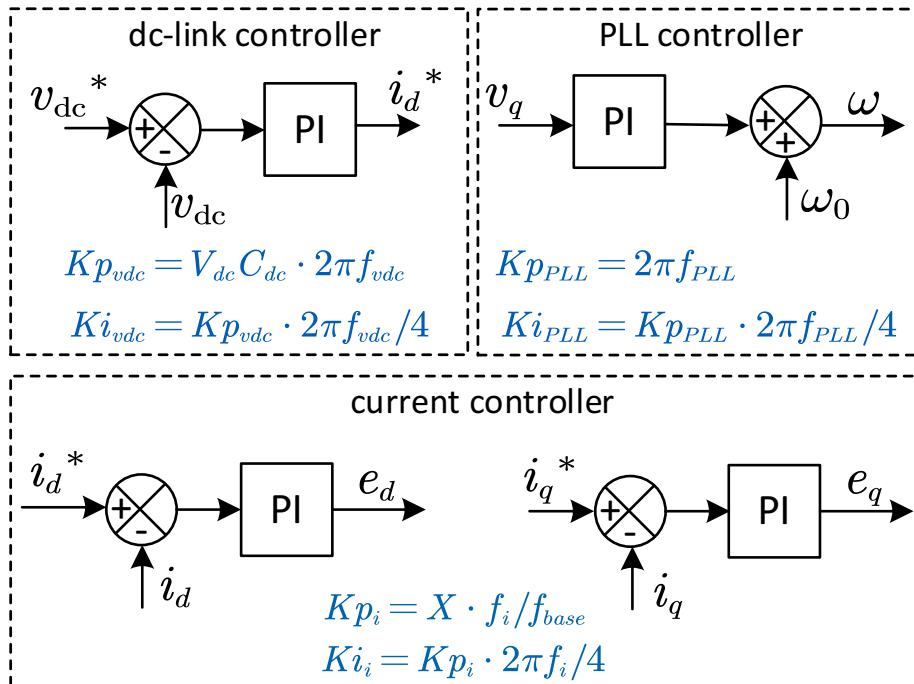
TABLE III
IEEE 14-BUS MODIFIED TEST SYSTEM GOVERNOR DATA

Type	BPA_GG	BPA_GG
Default Unit no. (New Unit no.)	1(15)	2(16)
Rated power (MVA)	448	100
Rated voltage (kV)	22	13.8
P_{max} (p.u)	0.870	1.050
R (p.u)	0.011	0.050
T_1 (s)	0.100	0.090
T_2 (s)	0.000	0.000
T_3 (s)	0.300	0.200
T_4 (s)	0.050	0.300
T_5 (s)	10.000	0.000
F	0.250	1.000

Grid-following Inverter

Parameter	A11	A12	A13
V_{dc} , dc-link voltage in p.u	2.500	2.500	2.500
C_{dc} , dc-link capacitor in p.u	1.25	1.25	1.25
X , series output reactance in p.u	0.03	0.03	0.03
R , series output resistance in p.u	0.01	0.01	0.01
f_{vdc} , dc-link control bandwidth in Hz	10	10	10
f_{PLL} , PLL control bandwidth in Hz	10	10	10
f_i , current control bandwidth in Hz	400	400	400

Grid-following Inverter control diagram



D.2 Modified NETS-NYPS 68-bus System

This appendix gives the detailed parameters of the modified 68-bus system studied in this paper. The parameters of the synchronous generators are mainly from the dynamic model in [104], while the generator at bus-15 is replaced by a grid-forming inverter in this thesis, together with 6 extra grid-following inverter. The full data is attached below.

Attachment: NETS-NYPS 68-Bus Modified Test System Data

Synchronous Machine Nomenclature

X	leakage reactance in p.u
R	resistance in p.u
x _d	d-axis synchronous reactance in p.u
x' _d	d-axis transient reactance in p.u
x'' _d	d-axis subtransient reactance in p.u
T' _d	d-axis open-circuit time constant in sec
T'' _d	d-axis open-circuit subtransient time constant in sec
x _q	q-axis synchronous reactance in p.u
x' _q	q-axis transient reactance in p.u
x'' _q	q-axis subtransient reactance in p.u
T' _q	q-axis open-circuit time constant in sec
T'' _q	q-axis open circuit subtransient time constant in sec
H	inertia constant in sec
D	damping coefficient

Synchronous Machine Data

Bus	X	R	x _d	x' _d	x'' _d	T' _d	T'' _d	x _q	x' _q	x'' _q	T' _q	T'' _q	H	D
1	0.013	0.025	0.100	0.031	0.025	10.2	0.05	0.069	0.0416667	0.025	1.5	0.035	42	0
2	0.035	0.070	0.295	0.070	0.050	6.56	0.05	0.28	0.0933333	0.05	1.5	0.035	30.2	0
3	0.030	0.061	0.250	0.053	0.045	5.7	0.05	0.237	0.0714286	0.045	1.5	0.035	35.8	0
4	0.030	0.059	0.262	0.044	0.035	5.69	0.05	0.258	0.0585714	0.035	1.5	0.035	28.6	0
5	0.027	0.054	0.330	0.066	0.050	5.4	0.05	0.31	0.0883333	0.05	0.44	0.035	26	0
6	0.022	0.045	0.254	0.050	0.040	7.3	0.05	0.241	0.0675	0.04	0.4	0.035	34.8	0
7	0.032	0.064	0.295	0.049	0.040	5.66	0.05	0.292	0.0666667	0.04	1.5	0.035	26.4	0
8	0.028	0.056	0.290	0.057	0.045	6.7	0.05	0.28	0.0766667	0.045	0.41	0.035	24.3	0
9	0.030	0.060	0.211	0.057	0.045	4.79	0.05	0.205	0.0766667	0.045	1.96	0.035	34.5	0
10	0.020	0.040	0.169	0.046	0.040	9.37	0.05	0.115	0.0615385	0.04	1.5	0.035	31	0
11	0.010	0.021	0.128	0.018	0.012	4.1	0.05	0.123	0.0241176	0.012	1.5	0.035	28.2	0
12	0.022	0.044	0.101	0.031	0.025	7.4	0.05	0.095	0.042	0.025	1.5	0.035	92.3	0
13	0.002	0.003	0.015	0.003	0.002	5.9	0.05	0.0143	0.0037	0.002	1.5	0.035	496	0
14	0.002	0.003	0.018	0.003	0.002	4.1	0.05	0.0173	0.0037931	0.0023	1.5	0.035	300	0
16	0.002	0.004	0.018	0.004	0.003	7.8	0.05	0.0167	0.00475	0.00275	1.5	0.035	450	0

Note:

- All synchronous machines have the base power of 100 MVA.
- Saturation factors of synchronous machine are omitted in this case.

Exciter Nomenclature

T_R	input filter time constant in sec
K_A	voltage regulator gain in p.u
T_A	voltage regulator time constant in sec
V_Rmax	maximum voltage regulator output in p.u
V_Rmin	minimum voltage regulator output in p.u
K_E	exciter constant in p.u
T_E	exciter time constant in p.u
E_1	Field voltage value,1 in p.u
S(E_1)	Saturation factor at E_1
E_2	Field voltage value,2 in p.u
S(E_2)	Saturation factor at E_2
K_F	stabilizer gain in p.u
T_F	stabilizer time constant in sec
K_P	regulator proportional gain in p.u
K_I	regulator integral gain in p.u
K_D	regulator derivative gain in p.u
T_D	regulator derivative time constant in sec

Exciter Data

Bus	T_R	K_A	T_A	V_Rmax	V_Rmin	K_E	T_E	E_1	S(E_1)	E_2	S(E_2)	K_F	T_F	K_P	K_I	K_D	T_D
1	0.01	1	0.02	10	-10	1	0.785	3.9267	0.07	5.2356	0.91	0.03	1	200	50	50	0.01
2	0.01	1	0.02	10	-10	1	0.785	3.9267	0.07	5.2356	0.91	0.03	1	200	50	50	0.01
3	0.01	1	0.02	10	-10	1	0.785	3.9267	0.07	5.2356	0.91	0.03	1	200	50	50	0.01
4	0.01	1	0.02	10	-10	1	0.785	3.9267	0.07	5.2356	0.91	0.03	1	200	50	50	0.01
5	0.01	1	0.02	10	-10	1	0.785	3.9267	0.07	5.2356	0.91	0.03	1	200	50	50	0.01
6	0.01	1	0.02	10	-10	1	0.785	3.9267	0.07	5.2356	0.91	0.03	1	200	50	50	0.01
7	0.01	1	0.02	10	-10	1	0.785	3.9267	0.07	5.2356	0.91	0.03	1	200	50	50	0.01
8	0.01	1	0.02	10	-10	1	0.785	3.9267	0.07	5.2356	0.91	0.03	1	200	50	50	0.01
9	0.01	1	0.02	10	-10	1	0.785	3.9267	0.07	5.2356	0.91	0.03	1	200	50	50	0.01
10	0.01	1	0.02	10	-10	1	0.785	3.9267	0.07	5.2356	0.91	0.03	1	200	50	50	0.01
11	0.01	1	0.02	10	-10	1	0.785	3.9267	0.07	5.2356	0.91	0.03	1	200	50	50	0.01
12	0.01	1	0.02	10	-10	1	0.785	3.9267	0.07	5.2356	0.91	0.03	1	200	50	50	0.01

Note:

- All are DC4B exciters .

PSS Nomenclature

KPSS	PSS gain in p.u
TW	washout time constant in sec
T11	first lead time constant in sec
T12	first lag time constant in sec
T21	second lead time constant in sec
T22	-second lag time constant in sec
T31	third lead time constant in sec
T32	third lag time constant in sec
VSSmax	maximum output limit in p.u
VSSmin	minimum output limit in p.u

PSS Data

Bus	KPSS	TW	T11	T12	T21	T22	T31	T32	VSSmax	VSSmin
1	20	15	0.15	0.04	0.15	0.04	0.15	0.04	0.2	-0.05
2	20	15	0.15	0.04	0.15	0.04	0.15	0.04	0.2	-0.05
3	20	15	0.15	0.04	0.15	0.04	0.15	0.04	0.2	-0.05
4	20	15	0.15	0.04	0.15	0.04	0.15	0.04	0.2	-0.05
5	20	15	0.15	0.04	0.15	0.04	0.15	0.04	0.2	-0.05
6	20	15	0.15	0.04	0.15	0.04	0.15	0.04	0.2	-0.05
7	20	15	0.15	0.04	0.15	0.04	0.15	0.04	0.2	-0.05
8	20	15	0.15	0.04	0.15	0.04	0.15	0.04	0.2	-0.05
9	20	15	0.15	0.04	0.15	0.04	0.15	0.04	0.2	-0.05
10	20	15	0.15	0.04	0.15	0.04	0.15	0.04	0.2	-0.05
11	20	15	0.15	0.04	0.15	0.04	0.15	0.04	0.2	-0.05
12	20	15	0.15	0.04	0.15	0.04	0.15	0.04	0.2	-0.05

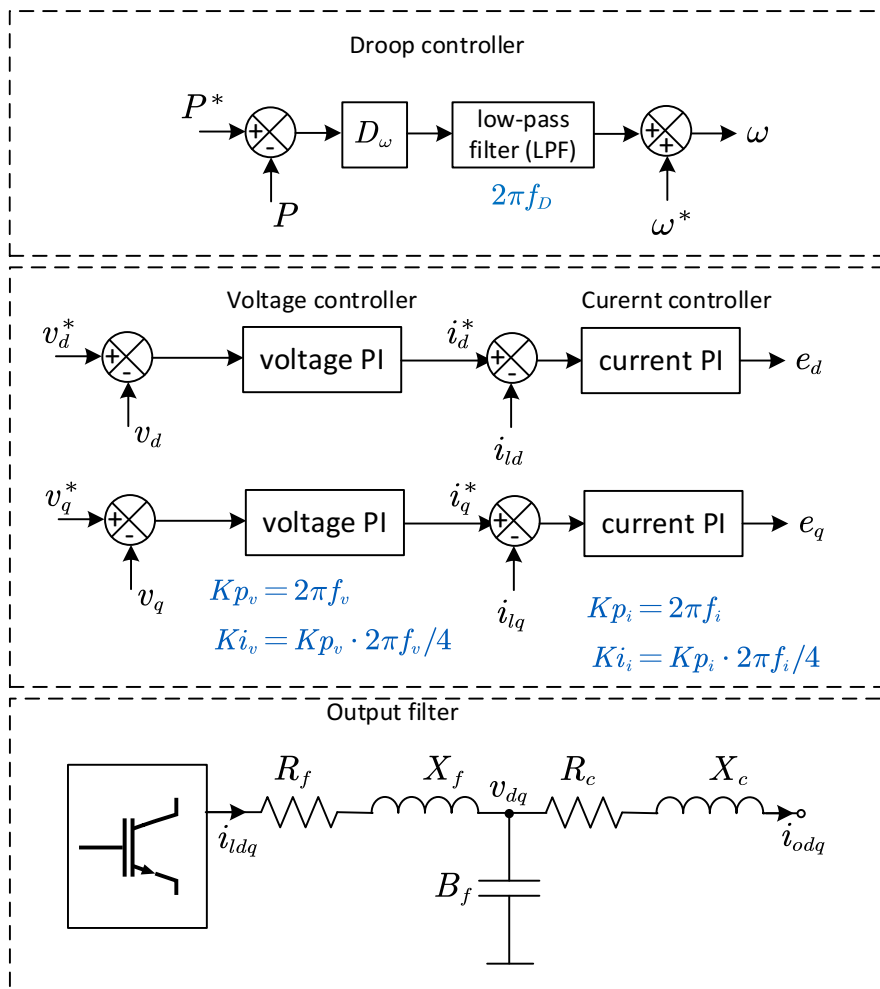
Note:

- All are three-order PSS.

Grid-forming Inverter

Parameter	A15
X_f , LCL filter invert-side reactance in p.u	0.200
R_f , LCL filter inverter-side resistance in p.u	0.020
B_f , LCL filter susceptance in p.u	0.080
X_c , LCL filter grid-side reactance in p.u	0.030
R_c , LCL filter grid-side resistance in p.u	0.00000955
D_ω , P-f droop Gain in p.u	0.005
f_d , droop-control bandwidth in Hz	20.000
f_v , voltage control bandwidth in Hz	100.000
f_i , current control bandwidth in Hz	250.000

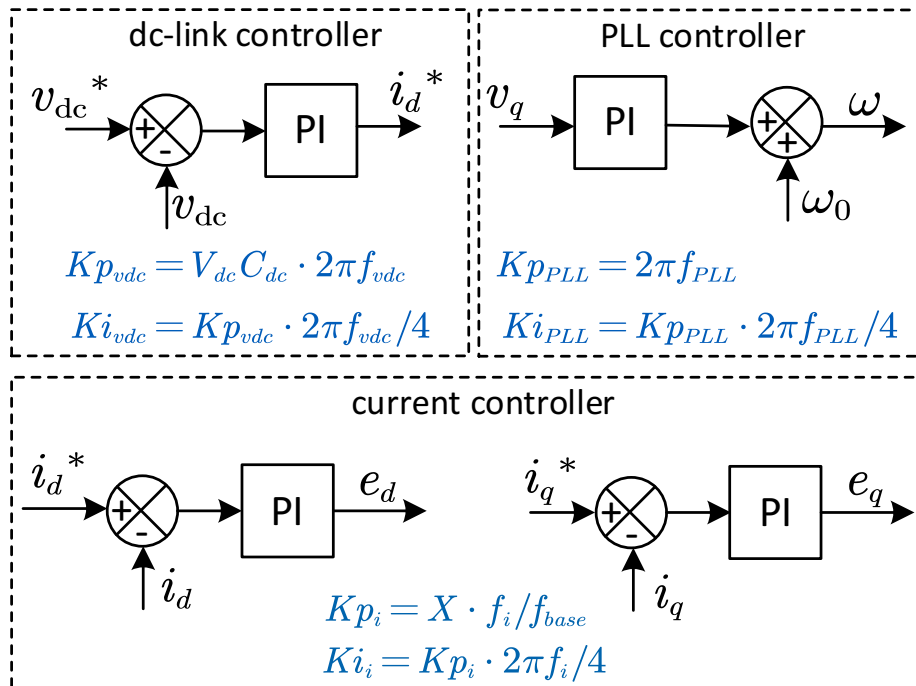
Grid-forming Inverter control diagram



Grid-following Inverter

Parameter	A17	A26	A28	A29	A58	A59
V_{dc} , dc-link voltage in p.u	2.500	2.500	2.500	2.500	2.500	2.500
C_{dc} , dc-link capacitor in p.u	7.500	7.500	7.500	7.500	7.500	7.500
X , series output reactance in p.u	0.005	0.005	0.005	0.005	0.005	0.005
R , series output resistance in p.u	0.002	0.002	0.002	0.002	0.002	0.002
f_{vdc} , dc-link control bandwidth in Hz	20.000	20.000	20.000	20.000	20.000	20.000
f_{PLL} , PLL control bandwidth in Hz	20.000	20.000	20.000	20.000	20.000	20.000
f_i , current control bandwidth in Hz	500.000	500.000	300.000	220.000	500.000	500.000

Grid-following Inverter control diagram



D.3 Triphase 10 kVA inverter schematic

The schematic of Triphase 10 kVA inverter is attached as shown in Fig. D.1. F1 is the input and F3 is the output. During the model running, contactors K1, K2, K3, K5, K6, KDC1, KDC2 are closed while others remain open, hence to configure the circuit as an AC-DC-AC circuit with an LCL output filter. Values of parameters are marked in the schematic.

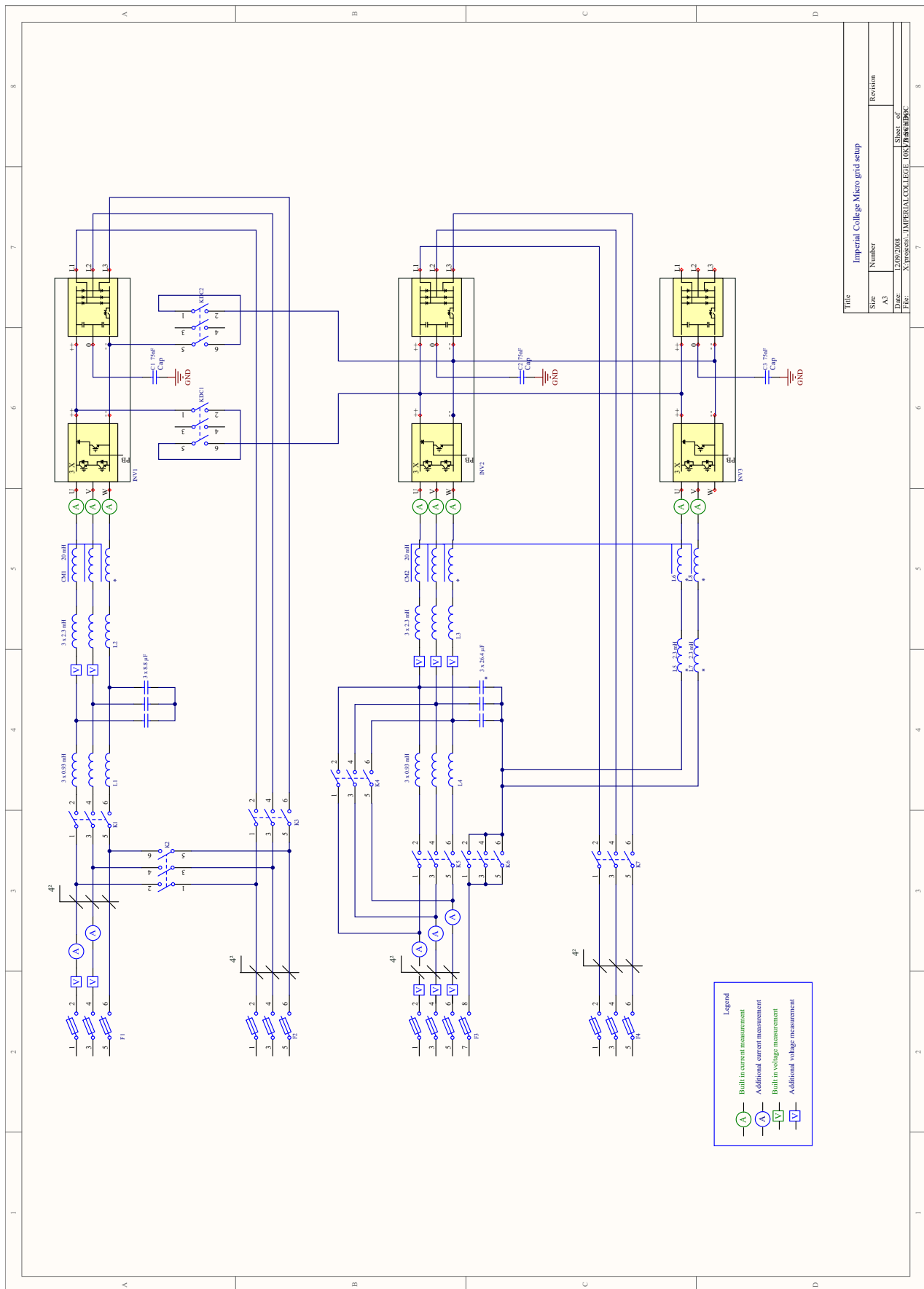


Figure D.1: Triphase 10 kVA inverter schematic.

Bibliography

- [1] REN21, “Renewables 2021 Global Status Report,” 2021. [Online]. Available: <https://www.ren21.net/reports/global-status-report/>
- [2] IEA, “Global Energy Review 2021,” 2021. [Online]. Available: <https://www.iea.org/reports/global-energy-review-2021/renewables>
- [3] NationGrid ESO, “Great Britain’s monthly electricity stats,” 2021. [Online]. Available: <https://www.nationalgrideso.com/electricity-explained/electricity-and-me/great-britains-monthly-electricity-stats>
- [4] F. Blaabjerg, Z. Chen, and S. Kjaer, “Power electronics as efficient interface in dispersed power generation systems,” *IEEE Transactions on Power Electronics*, vol. 19, no. 5, pp. 1184–1194, 2004.
- [5] H. Liu, X. Xie, J. He, T. Xu, Z. Yu, C. Wang, and C. Zhang, “Subsynchronous interaction between direct-drive pmsg based wind farms and weak ac networks,” *IEEE Transactions on Power Systems*, vol. 32, no. 6, pp. 4708–4720, 2017.
- [6] Q.-C. Zhong, “Power-electronics-enabled autonomous power systems: Architecture and technical routes,” *IEEE Transactions on Industrial Electronics*, vol. 64, no. 7, pp. 5907–5918, 2017.
- [7] Q.-C. Zhong and G. Weiss, “Synchronverters: Inverters that mimic synchronous generators,” *IEEE Transactions on Industrial Electronics*, vol. 58, no. 4, pp. 1259–1267, 2011.
- [8] J. Adams, V. A. Pappu, and A. Dixit, “Ercot experience screening for sub-synchronous control interaction in the vicinity of series capacitor banks,” in *2012 IEEE Power and Energy Society General Meeting*, 2012, pp. 1–5.
- [9] C. Buchhagen, C. Rauscher, A. Menze, and J. Jung, “Borwin1 - first experiences with har-

- monic interactions in converter dominated grids,” in *International ETG Congress 2015; Die Energiewende - Blueprints for the new energy age*, 2015, pp. 1–7.
- [10] H. Liu, L. Jin, D. Le, and A. A. Chowdhury, “Impact of high penetration of solar photovoltaic generation on power system small signal stability,” in *2010 International Conference on Power System Technology*, 2010, pp. 1–7.
- [11] S. Impram, S. Varbak Nese, and B. Oral, “Challenges of renewable energy penetration on power system flexibility: A survey,” *Energy Strategy Reviews*, vol. 31, p. 100539, 2020. [Online]. Available: <https://www.sciencedirect.com/science/article/pii/S2211467X20300924>
- [12] J. Enslin and P. Heskes, “Harmonic interaction between a large number of distributed power inverters and the distribution network,” *IEEE Transactions on Power Electronics*, vol. 19, no. 6, pp. 1586–1593, 2004.
- [13] M. Cespedes and J. Sun, “Renewable energy systems instability involving grid-parallel inverters,” in *2009 Twenty-Fourth Annual IEEE Applied Power Electronics Conference and Exposition*, 2009, pp. 1971–1977.
- [14] R. W. Kenyon, M. Bossart, M. Marković, K. Doubleday, R. Matsuda-Dunn, S. Mitova, S. A. Julien, E. T. Hale, and B.-M. Hodge, “Stability and control of power systems with high penetrations of inverter-based resources: An accessible review of current knowledge and open questions,” *Solar Energy*, vol. 210, pp. 149–168, 2020.
- [15] J. Guo, T. Chen, B. Chaudhuri, and S. Y. R. Hui, “Stability of isolated microgrids with renewable generation and smart loads,” *IEEE Transactions on Sustainable Energy*, vol. 11, no. 4, pp. 2845–2854, 2020.
- [16] OFGEM, “9 August 2019 power outage report,” 2020. [Online]. Available: <https://www.ofgem.gov.uk/publications/investigation-9-august-2019-power-outage>
- [17] J. Bialek, “What does the GB power outage on 9 august 2019 tell us about the current state of decarbonised power systems?” *Energy Policy*, vol. 146, p. 111821, 2020.
- [18] Ørsted, “Appendix D – Hornsea Technical Report Submitted by Ørsted,” 2016. [Online]. Available: https://www.ofgem.gov.uk/sites/default/files/docs/2019/09/eso_technical_report_-_appendices_-_final.pdf
- [19] P. Kundur, *Power system stability and control*. McGraw-hill New York, 1994, vol. 7.

- [20] G. O. Kalcon, G. P. Adam, O. Anaya-Lara, S. Lo, and K. Uhlen, "Small-signal stability analysis of multi-terminal vsc-based dc transmission systems," *IEEE Transactions on Power Systems*, vol. 27, no. 4, pp. 1818–1830, 2012.
- [21] N. Pogaku, M. Prodanovic, and T. C. Green, "Modeling, analysis and testing of autonomous operation of an inverter-based microgrid," *IEEE Transactions on Power Electronics*, vol. 22, no. 2, pp. 613–625, 2007.
- [22] Y. Gu, N. Bottrell, and T. C. Green, "Reduced-order models for representing converters in power system studies," *IEEE Transactions on Power Electronics*, vol. 33, no. 4, pp. 3644–3654, 2018.
- [23] Y. Wang, X. Wang, Z. Chen, and F. Blaabjerg, "Small-signal stability analysis of inverter-fed power systems using component connection method," *IEEE Transactions on Smart Grid*, vol. 9, no. 5, pp. 5301–5310, 2018.
- [24] I. J. Perez-arriaga, G. C. Verghese, and F. C. Schweppe, "Selective modal analysis with applications to electric power systems, part i: Heuristic introduction," *IEEE Transactions on Power Apparatus and Systems*, vol. PAS-101, no. 9, pp. 3117–3125, 1982.
- [25] T. Smed, "Feasible eigenvalue sensitivity for large power systems," *IEEE Transactions on Power Systems*, vol. 8, no. 2, pp. 555–563, 1993.
- [26] H.-K. Nam, Y.-K. Kim, K.-S. Shim, and K. Lee, "A new eigen-sensitivity theory of augmented matrix and its applications to power system stability analysis," *IEEE Transactions on Power Systems*, vol. 15, no. 1, pp. 363–369, 2000.
- [27] F. Gao, X. Zheng, S. Bozhko, C. I. Hill, and G. Asher, "Modal analysis of a pmsg-based dc electrical power system in the more electric aircraft using eigenvalues sensitivity," *IEEE Transactions on Transportation Electrification*, vol. 1, no. 1, pp. 65–76, 2015.
- [28] B. Pal, A. Coonick, I. Jaimoukha, and H. El-Zobaidi, "A linear matrix inequality approach to robust damping control design in power systems with superconducting magnetic energy storage device," *IEEE Transactions on Power Systems*, vol. 15, no. 1, pp. 356–362, 2000.
- [29] B. Chaudhuri, B. Pal, A. Zolotas, I. Jaimoukha, and T. Green, "Mixed-sensitivity approach to H_{∞} control of power system oscillations employing multiple FACTS devices," *IEEE Transactions on Power Systems*, vol. 18, no. 3, pp. 1149–1156, 2003.

- [30] J. Deng and X.-P. Zhang, "Robust damping control of power systems with tcsc: A multi-model bmi approach with h₂ performance," *IEEE Transactions on Power Systems*, vol. 29, no. 4, pp. 1512–1521, 2014.
- [31] P. W. Sauer, M. A. Pai, and J. H. Chow, *Power system dynamics and stability: with synchrophasor measurement and power system toolbox*. John Wiley & Sons, 2017.
- [32] NEPLAN, "EXCITER MODELS," 2015. [Online]. Available: https://www.neplan.ch/wp-content/uploads/2015/08/Nep_EXCITERS1.pdf
- [33] NEPLAN, "POWER SYSTEM STABILIZER MODELS MODELS," 2015. [Online]. Available: https://www.neplan.ch/wp-content/uploads/2015/08/Nep_PSSs1.pdf
- [34] Piotr Mars, Miłosz Miśkiewicz, Paweł Błaszczuk and Tomasz Kuczek, "Modeling of ABB solar inverters in power system simulations," 2018. [Online]. Available: <https://new.abb.com/news/detail/9998/modeling-of-abb-solar-inverters-in-power-system-simulations>
- [35] Z. Jiang, L. Yang, Z. Gao, and T. Moan, "Numerical simulation of a wind turbine with a hydraulic transmission system," *Energy Procedia*, vol. 53, pp. 44–55, 2014.
- [36] W. J. Lasantha Perera, "EMT and RMS model requirements, AECOM Australia," 2017. [Online]. Available: <https://aemo.com.au/en/energy-systems/electricity/national-electricity-market-nem/participate-in-the-market/network-connections/modelling-requirements>
- [37] J. Sun, "Impedance-based stability criterion for grid-connected inverters," *IEEE Transactions on Power Electronics*, vol. 26, no. 11, pp. 3075–3078, 2011.
- [38] X. Wang, L. Harnefors, and F. Blaabjerg, "Unified impedance model of grid-connected voltage-source converters," *IEEE Transactions on Power Electronics*, vol. 33, no. 2, pp. 1775–1787, 2018.
- [39] M. Cespedes and J. Sun, "Impedance modeling and analysis of grid-connected voltage-source converters," *IEEE Transactions on Power Electronics*, vol. 29, no. 3, pp. 1254–1261, 2014.
- [40] Y. Li, "Modeling and control of power electronic converters in power systems," Ph.D. dissertation, Imperial College London, 2020.
- [41] R. W. Erickson and D. Maksimovic, *Fundamentals of power electronics*. Springer Science & Business Media, 2007.

- [42] K. H. Ang, G. Chong, and Y. Li, "Pid control system analysis, design, and technology," *IEEE Transactions on Control Systems Technology*, vol. 13, no. 4, pp. 559–576, 2005.
- [43] F. Lewis, "EE 4314 control systems," 2007. [Online]. Available: <https://lewisgroup.uta.edu/ee4314/lectures/Bode%20perf%20spec.pdf>
- [44] Z. Miao, "Impedance-model-based ssr analysis for type 3 wind generator and series-compensated network," *IEEE Transactions on Energy Conversion*, vol. 27, no. 4, pp. 984–991, 2012.
- [45] B. Wen, D. Boroyevich, R. Burgos, P. Mattavelli, and Z. Shen, "Small-signal stability analysis of three-phase ac systems in the presence of constant power loads based on measured d - q frame impedances," *IEEE Transactions on Power Electronics*, vol. 30, no. 10, pp. 5952–5963, 2015.
- [46] F. Wang, J. L. Duarte, M. A. M. Hendrix, and P. F. Ribeiro, "Modeling and analysis of grid harmonic distortion impact of aggregated dg inverters," *IEEE Transactions on Power Electronics*, vol. 26, no. 3, pp. 786–797, 2011.
- [47] C. Zhang, M. Molinas, A. Rygg, and X. Cai, "Impedance-based analysis of interconnected power electronics systems: Impedance network modeling and comparative studies of stability criteria," *IEEE Journal of Emerging and Selected Topics in Power Electronics*, vol. 8, no. 3, pp. 2520–2533, 2020.
- [48] C. Zhang, X. Cai, M. Molinas, and A. Rygg, "On the impedance modeling and equivalence of ac/dc-side stability analysis of a grid-tied type-iv wind turbine system," *IEEE Transactions on Energy Conversion*, vol. 34, no. 2, pp. 1000–1009, 2019.
- [49] Wen, Bo and Boroyevich, Dushan and Burgos, Rolando and Mattavelli, Paolo and Shen, Zhiyu, "Analysis of D-Q small-signal impedance of grid-tied inverters," *IEEE Transactions on Power Electronics*, vol. 31, no. 1, pp. 675–687, 2016.
- [50] S. Hiti, V. Vlatkovic, D. Borojevic, and F. Lee, "A new control algorithm for three-phase pwm buck rectifier with input displacement factor compensation," *IEEE Transactions on Power Electronics*, vol. 9, no. 2, pp. 173–180, 1994.
- [51] H. Mao, D. Boroyevich, and F. Lee, "Novel reduced-order small-signal model of a three-phase pwm rectifier and its application in control design and system analysis," *IEEE Transactions on*

- Power Electronics*, vol. 13, no. 3, pp. 511–521, 1998.
- [52] J. Sun, Z. Bing, and K. J. Karimi, “Input impedance modeling of multipulse rectifiers by harmonic linearization,” *IEEE Transactions on Power Electronics*, vol. 24, no. 12, pp. 2812–2820, 2009.
- [53] Y. Li, Y. Gu, Y. Zhu, A. Junyent-Ferré, X. Xiang, and T. C. Green, “Impedance circuit model of grid-forming inverter: Visualizing control algorithms as circuit elements,” *IEEE Transactions on Power Electronics*, vol. 36, no. 3, pp. 3377–3395, 2021.
- [54] J. Huang, K. A. Corzine, and M. Belkhaty, “Small-signal impedance measurement of power-electronics-based ac power systems using line-to-line current injection,” *IEEE Transactions on Power Electronics*, vol. 24, no. 2, pp. 445–455, 2009.
- [55] Y. A. Familant, J. Huang, K. A. Corzine, and M. Belkhaty, “New techniques for measuring impedance characteristics of three-phase ac power systems,” *IEEE Transactions on Power Electronics*, vol. 24, no. 7, pp. 1802–1810, 2009.
- [56] S. Shah, P. Koralewicz, R. Wallen, and V. Gevorgian, “Impedance characterization of utility-scale renewable energy and storage systems,” in *2019 IEEE Energy Conversion Congress and Exposition (ECCE)*, 2019, pp. 2609–2616.
- [57] B. Gustavsen and A. Semlyen, “Rational approximation of frequency domain responses by vector fitting,” *IEEE Transactions on Power Delivery*, vol. 14, no. 3, pp. 1052–1061, 1999.
- [58] T. Roinila, M. Vilkkö, and J. Sun, “Online grid impedance measurement using discrete-interval binary sequence injection,” *IEEE Journal of Emerging and Selected Topics in Power Electronics*, vol. 2, no. 4, pp. 985–993, 2014.
- [59] A. Riccobono, M. Mirz, and A. Monti, “Noninvasive online parametric identification of three-phase ac power impedances to assess the stability of grid-tied power electronic inverters in lv networks,” *IEEE Journal of Emerging and Selected Topics in Power Electronics*, vol. 6, no. 2, pp. 629–647, 2018.
- [60] M. Zhang, X. Wang, and Q. Xu, “Data-driven modeling of power-electronics-based power system considering the operating point variation,” in *2021 IEEE Energy Conversion Congress and Exposition (ECCE)*, 2021, pp. 3513–3517.
- [61] M. Zhang, X. Wang, D. Yang, and M. G. Christensen, “Artificial neural network based identi-

- fication of multi-operating-point impedance model,” *IEEE Transactions on Power Electronics*, vol. 36, no. 2, pp. 1231–1235, 2021.
- [62] M. Liserre, R. Teodorescu, and F. Blaabjerg, “Stability of photovoltaic and wind turbine grid-connected inverters for a large set of grid impedance values,” *IEEE Transactions on Power Electronics*, vol. 21, no. 1, pp. 263–272, 2006.
- [63] J. Castello and J. M. Espi, “DSP implementation for measuring the loop gain frequency response of digitally controlled power converters,” *IEEE Transactions on Power Electronics*, vol. 27, no. 9, pp. 4113–4121, 2012.
- [64] Y. Zhu, J. Wu, R. Wang, Z. Lin, and X. He, “Embedding power line communication in photovoltaic optimizer by modulating data in power control loop,” *IEEE Transactions on Industrial Electronics*, vol. 66, no. 5, pp. 3948–3958, 2019.
- [65] X. Feng, J. Liu, and F. Lee, “Impedance specifications for stable dc distributed power systems,” *IEEE Transactions on Power Electronics*, vol. 17, no. 2, pp. 157–162, 2002.
- [66] A. A. A. Radwan and Y. A.-R. I. Mohamed, “Linear active stabilization of converter-dominated dc microgrids,” *IEEE Transactions on Smart Grid*, vol. 3, no. 1, pp. 203–216, 2012.
- [67] S. Sudhoff, S. Glover, P. Lamm, D. Schmucker, and D. Delisle, “Admittance space stability analysis of power electronic systems,” *IEEE Transactions on Aerospace and Electronic Systems*, vol. 36, no. 3, pp. 965–973, 2000.
- [68] M. Belkhat, “Stability criteria for ac power systems with regulated loads,” Ph.D. dissertation, Purdue University, 1997.
- [69] J. Sun, “Small-signal methods for ac distributed power systems—a review,” *IEEE Transactions on Power Electronics*, vol. 24, no. 11, pp. 2545–2554, 2009.
- [70] A. A. A. Radwan and Y. A.-R. I. Mohamed, “Analysis and active-impedance-based stabilization of voltage-source-rectifier loads in grid-connected and isolated microgrid applications,” *IEEE Transactions on Sustainable Energy*, vol. 4, no. 3, pp. 563–576, 2013.
- [71] B. Wen, D. Dong, D. Boroyevich, R. Burgos, P. Mattavelli, and Z. Shen, “Impedance-based analysis of grid-synchronization stability for three-phase paralleled converters,” *IEEE Transactions on Power Electronics*, vol. 31, no. 1, pp. 26–38, 2016.
- [72] R. Burgos, D. Boroyevich, F. Wang, K. Karimi, and G. Francis, “On the ac stability of high

- power factor three-phase rectifiers,” in *2010 IEEE Energy Conversion Congress and Exposition*, 2010, pp. 2047–2054.
- [73] A. G. MacFarlane and I. Postlethwaite, “The generalized nyquist stability criterion and multi-variable root loci,” *International Journal of Control*, vol. 25, no. 1, pp. 81–127, 1977.
- [74] C. Desoer and Y.-T. Wang, “On the generalized nyquist stability criterion,” *IEEE Transactions on Automatic Control*, vol. 25, no. 2, pp. 187–196, 1980.
- [75] K. Padiyar, *Structure preserving energy functions in power systems: theory and applications*. CRC Press, 2018.
- [76] Y. Gu, Y. Li, Y. Zhu, and T. C. Green, “Impedance-based whole-system modeling for a composite grid via embedding of frame dynamics,” *IEEE Transactions on Power Systems*, vol. 36, no. 1, pp. 336–345, 2021.
- [77] E. Ebrahimzadeh, F. Blaabjerg, X. Wang, and C. L. Bak, “Bus participation factor analysis for harmonic instability in power electronics based power systems,” *IEEE Transactions on Power Electronics*, vol. 33, no. 12, pp. 10 341–10 351, 2018.
- [78] Y. Zhan, X. Xie, H. Liu, H. Liu, and Y. Li, “Frequency-domain modal analysis of the oscillatory stability of power systems with high-penetration renewables,” *IEEE Transactions on Sustainable Energy*, vol. 10, no. 3, pp. 1534–1543, 2019.
- [79] H. Wang and J. Sun, “Impedance-based stability modeling and analysis of networked converter systems,” in *2019 20th Workshop on Control and Modeling for Power Electronics (COMPEL)*, 2019, pp. 1–8.
- [80] A. Semlyen, “s-domain methodology for assessing the small signal stability of complex systems in nonsinusoidal steady state,” *IEEE Transactions on Power Systems*, vol. 14, no. 1, pp. 132–137, 1999.
- [81] S. Gomes, N. Martins, and C. Portela, “Modal analysis applied to s-domain models of ac networks,” in *2001 IEEE Power Engineering Society Winter Meeting. Conference Proceedings (Cat. No.01CH37194)*, vol. 3, 2001, pp. 1305–1310 vol.3.
- [82] W. Xu, Z. Huang, Y. Cui, and H. Wang, “Harmonic resonance mode analysis,” *IEEE Transactions on Power Delivery*, vol. 20, no. 2, pp. 1182–1190, 2005.
- [83] Z. Huang, Y. Cui, and W. Xu, “Application of modal sensitivity for power system harmonic

- resonance analysis,” *IEEE Transactions on Power Systems*, vol. 22, no. 1, pp. 222–231, 2007.
- [84] Y. Cui and W. Xu, “Harmonic resonance mode analysis using real symmetrical nodal matrices,” *IEEE Transactions on Power Delivery*, vol. 22, no. 3, pp. 1989–1990, 2007.
- [85] Y. Cui and X. Wang, “Modal frequency sensitivity for power system harmonic resonance analysis,” *IEEE Transactions on Power Delivery*, vol. 27, no. 2, pp. 1010–1017, 2012.
- [86] H. Hu, Z. He, Y. Zhang, and S. Gao, “Modal frequency sensitivity analysis and application using complex nodal matrix,” *IEEE Transactions on Power Delivery*, vol. 29, no. 2, pp. 969–971, 2014.
- [87] Z. Liu, J. Rong, G. Zhao, and Y. Luo, “Harmonic assessment for wind parks based on sensitivity analysis,” *IEEE Transactions on Sustainable Energy*, vol. 8, no. 4, pp. 1373–1382, 2017.
- [88] Y. Zhan, X. Xie, and Y. Wang, “Impedance network model based modal observability and controllability analysis for renewable integrated power systems,” *IEEE Transactions on Power Delivery*, vol. 36, no. 4, pp. 2025–2034, 2021.
- [89] H. Zong, C. Zhang, X. Cai, and M. Molinas, “Oscillation propagation analysis of hybrid ac/dc grids with high penetration renewables,” *IEEE Transactions on Power Systems*, pp. 1–1, 2022.
- [90] Y. Li, Z. Shuai, X. Liu, Y. Chen, Z. Li, Y. Hong, and Z. J. Shen, “Stability analysis and location optimization method for multiconverter power systems based on nodal admittance matrix,” *IEEE Journal of Emerging and Selected Topics in Power Electronics*, vol. 9, no. 1, pp. 529–538, 2021.
- [91] D. Yang and Y. Sun, “Siso impedance-based stability analysis for system-level small-signal stability assessment of large-scale power electronics-dominated power systems,” *IEEE Transactions on Sustainable Energy*, vol. 13, no. 1, pp. 537–550, 2022.
- [92] Y. Liao, X. Wang, and X. Wang, “Frequency-domain participation analysis for electronic power systems,” *IEEE Transactions on Power Electronics*, vol. 37, no. 3, pp. 2531–2537, 2022.
- [93] Z. Shen, “Online measurement of three-phase ac power system impedance in synchronous coordinates,” Ph.D. dissertation, Virginia Polytechnic Institute and State University, 2013.
- [94] T. Roinila, M. Vilkkko, and J. Sun, “Broadband methods for online grid impedance measurement,” in *2013 IEEE Energy Conversion Congress and Exposition*, 2013, pp. 3003–3010.
- [95] Y. Zhu, Y. Gu, Y. Li, and T. C. Green, “Participation analysis in impedance models: The grey-

- box approach for power system stability,” *IEEE Transactions on Power Systems*, vol. 37, no. 1, pp. 343–353, 2022.
- [96] Y. Zhu, Y. Gu, Y. Li, and T. Green, “Impedance-based root-cause analysis: Comparative study of impedance models and calculation of eigenvalue sensitivity,” *IEEE Transactions on Power Systems*, pp. 1–1, 2022.
- [97] Z. Xu, S. Wang, F. Xing, and H. Xiao, “Study on the method for analyzing electric network resonance stability,” *Energies*, vol. 11, no. 3, 2018. [Online]. Available: <https://www.mdpi.com/1996-1073/11/3/646>
- [98] N. Zhang, J. Yang, Y. Wang, H. Li, and C. Kang, “Chapter two - decoupled linear ac power flow models with accurate estimation of voltage magnitude in transmission and distribution systems,” in *New Technologies for Power System Operation and Analysis*, H. Jiang, Y. Zhang, and E. Muljadi, Eds. Academic Press, 2021, pp. 23–48. [Online]. Available: <https://www.sciencedirect.com/science/article/pii/B978012820168800002X>
- [99] Mathworks Help Center, “Exact linearization algorithm.” [Online]. Available: <https://uk.mathworks.com/help/slcontrol/ug/exact-linearization-algorithm.html>
- [100] “Future power networks.” [Online]. Available: <https://github.com/Future-Power-Networks/Publications>
- [101] “Ieee 14bus network.” [Online]. Available: <https://www2.kios.ucy.ac.cy/testsystems/index.php/ieee-14-bus-modified-test-system/>
- [102] T. Green and M. Prodanović, “Control of inverter-based micro-grids,” *Electric Power Systems Research*, vol. 77, no. 9, pp. 1204–1213, 2007, distributed Generation. [Online]. Available: <https://www.sciencedirect.com/science/article/pii/S037877960600191X>
- [103] Y. Li, Y. Gu, and T. Green, “Revisiting grid-forming and grid-following inverters: A duality theory,” *IEEE Transactions on Power Systems*, pp. 1–1, 2022.
- [104] A. K. Singh and B. C. Pal, “IEEE PES task force on benchmark systems for stability controls report on the 68-bus 16-machine 5-area system,” *IEEE Power Energy Soc*, vol. 3, 2013.
- [105] B. Qi, K. N. Hasan, and J. V. Milanović, “Identification of critical parameters affecting voltage and angular stability considering load-renewable generation correlations,” *IEEE Transactions on Power Systems*, vol. 34, no. 4, pp. 2859–2869, 2019.

- [106] D. Crevier and A. Mercier, "Estimation of higher frequency network equivalent impedances by harmonic analysis natural waveforms," *IEEE Transactions on Power Apparatus and Systems*, vol. PAS-97, no. 2, pp. 424–431, 1978.
- [107] S. Kannan, J. Meyer, P. Schegner, and J. Rens, "A novel non-invasive harmonic resonance detection in public lv networks," in *2021 IEEE 11th International Workshop on Applied Measurements for Power Systems (AMPS)*, 2021, pp. 1–6.
- [108] S. Kannan, J. Meyer, J. Rens, and P. Schegner, "A novel extended noninvasive harmonic resonance detection technique for public low-voltage networks," *IEEE Transactions on Instrumentation and Measurement*, vol. 71, pp. 1–11, 2022.
- [109] V. Valdivia, A. Lázaro, A. Barrado, P. Zumel, and C. Fernández, "Impedance identification method of three-phase balanced voltage source inverters based on load current steps," in *2010 IEEE 12th Workshop on Control and Modeling for Power Electronics (COMPEL)*, 2010, pp. 1–7.
- [110] V. Valdivia, A. Lázaro, A. Barrado, P. Zumel, C. Fernández, and M. Sanz, "Impedance identification procedure of three-phase balanced voltage source inverters based on transient response measurements," *IEEE Transactions on Power Electronics*, vol. 26, no. 12, pp. 3810–3816, 2011.
- [111] L. Fan and Z. Miao, "Time-domain measurement-based DQ-frame admittance model identification for inverter-based resources," *IEEE Transactions on Power Systems*, vol. 36, no. 3, pp. 2211–2221, 2021.
- [112] L. Czarnecki and Z. Staroszczyk, "Dynamic on-line measurement of equivalent parameters of three-phase systems for harmonic frequencies," *European transactions on electrical power*, vol. 6, no. 5, pp. 329–336, 1996.
- [113] G. Francis, R. Burgos, D. Boroyevich, F. Wang, and K. Karimi, "An algorithm and implementation system for measuring impedance in the d-q domain," in *2011 IEEE Energy Conversion Congress and Exposition*, 2011, pp. 3221–3228.
- [114] Y. Familant, K. Corzine, J. Huang, and M. Belkhat, "Ac impedance measurement techniques," in *IEEE International Conference on Electric Machines and Drives, 2005.*, 2005, pp. 1850–1857.

- [115] Z. Shen, M. Jaksic, P. Mattavelli, D. Boroyevich, J. Verhulst, and M. Belkhat, "Design and implementation of three-phase ac impedance measurement unit (imu) with series and shunt injection," in *2013 Twenty-Eighth Annual IEEE Applied Power Electronics Conference and Exposition (APEC)*, 2013, pp. 2674–2681.
- [116] M. Cespedes and J. Sun, "Three-phase impedance measurement for system stability analysis," in *2013 IEEE 14th Workshop on Control and Modeling for Power Electronics (COMPEL)*, 2013, pp. 1–6.
- [117] D. Martin, E. Santi, and A. Barkley, "Wide bandwidth system identification of ac system impedances by applying perturbations to an existing converter," in *2011 IEEE Energy Conversion Congress and Exposition*, 2011, pp. 2549–2556.
- [118] M. Cespedes and J. Sun, "Adaptive control of grid-connected inverters based on online grid impedance measurements," *IEEE Transactions on Sustainable Energy*, vol. 5, no. 2, pp. 516–523, 2014.
- [119] J. Liu, X. Feng, F. Lee, and D. Boroyevich, "Stability margin monitoring for dc distributed power systems via current/voltage perturbation," in *APEC 2001. Sixteenth Annual IEEE Applied Power Electronics Conference and Exposition (Cat. No.01CH37181)*, vol. 2, 2001, pp. 745–751 vol.2.
- [120] X. Feng and F. Lee, "On-line measurement on stability margin of dc distributed power system," in *APEC 2000. Fifteenth Annual IEEE Applied Power Electronics Conference and Exposition (Cat. No.00CH37058)*, vol. 2, 2000, pp. 1190–1196 vol.2.
- [121] M. Harris, A. Kelley, J. Rhode, and M. Baran, "Instrumentation for measurement of line impedance," in *Proceedings of 1994 IEEE Applied Power Electronics Conference and Exposition - ASPEC'94*, 1994, pp. 887–893 vol.2.
- [122] M. Jaksic, Z. Shen, I. Cvetkovic, D. Boroyevich, R. Burgos, and P. Mattavelli, "Multi-level single-phase shunt current injection converter used in small-signal dq impedance identification," in *2014 IEEE Applied Power Electronics Conference and Exposition - APEC 2014*, 2014, pp. 2775–2782.
- [123] M. A. Salmani and C. S. Edrington, "Small-signal stability assessment of the power electronic-based ac systems using impedance measurement-based technique," in *2013 North American*

Power Symposium (NAPS), 2013, pp. 1–6.

- [124] X. Yue, Z. Fang, F. Wang, Z. Zhang, and H. Shi, “A novel adaptive frequency injection method for power electronic system impedance measurement,” *IEEE Transactions on Power Electronics*, vol. 29, no. 12, pp. 6700–6711, 2014.
- [125] D. Yang, X. Wang, M. Ndreco, W. Winter, R. Juhlin, and A. Krontiris, “Automation of impedance measurement for harmonic stability assessment of mmc-hvdc systems,” in *18th International Workshop on Large-scale Integration of Wind Power into Power Systems as well as on Transmission Networks for Offshore Wind Power Plants*, 2019, 18th Wind Integration Workshop ; Conference date: 16-10-2019 Through 18-10-2019.
- [126] M. Li, H. Nian, B. Hu, Y. Xu, Y. Liao, and J. Yang, “Adaptive frequency adjustment method for impedance measurement,” *IEEE Journal of Emerging and Selected Topics in Power Electronics*, vol. 10, no. 1, pp. 518–531, 2022.
- [127] S. Shah, P. Koralewicz, V. Gevorgian, and R. Wallen, “Sequence impedance measurement of utility-scale wind turbines and inverters – reference frame, frequency coupling, and mimo/iso forms,” *IEEE Transactions on Energy Conversion*, vol. 37, no. 1, pp. 75–86, 2022.
- [128] T. Roinila, T. Messo, and E. Santi, “Mimo-identification techniques for rapid impedance-based stability assessment of three-phase systems in dq domain,” *IEEE Transactions on Power Electronics*, vol. 33, no. 5, pp. 4015–4022, 2018.
- [129] G. Francis, “An algorithm and system for measuring impedance in dq coordinates,” Ph.D. dissertation, Virginia Tech, 2010.
- [130] Z. Shen, M. Jaksic, P. Mattavelli, D. Boroyevich, J. Verhulst, and M. Belkhat, “Three-phase ac system impedance measurement unit (imu) using chirp signal injection,” in *2013 Twenty-Eighth Annual IEEE Applied Power Electronics Conference and Exposition (APEC)*, 2013, pp. 2666–2673.
- [131] Z. Staroszczyk, “A method for real-time, wide-band identification of the source impedance in power systems,” *IEEE Transactions on Instrumentation and Measurement*, vol. 54, no. 1, pp. 377–385, 2005.
- [132] B. Palethorpe, M. Sumner, and D. Thomas, “Power system impedance measurement using a power electronic converter,” in *Ninth International Conference on Harmonics and Quality of*

Power. Proceedings (Cat. No.00EX441), vol. 1, 2000, pp. 208–213 vol.1.

- [133] L. Fan, Z. Miao, P. Koralewicz, S. Shah, and V. Gevorgian, “Identifying dq-domain admittance models of a 2.3-mva commercial grid-following inverter via frequency-domain and time-domain data,” *IEEE Transactions on Energy Conversion*, vol. 36, no. 3, pp. 2463–2472, 2021.
- [134] G. F. Lauss, M. O. Faruque, K. Schoder, C. Dufour, A. Viehweider, and J. Langston, “Characteristics and design of power hardware-in-the-loop simulations for electrical power systems,” *IEEE Transactions on Industrial Electronics*, vol. 63, no. 1, pp. 406–417, 2016.
- [135] H. Pishro-Nik, *Introduction to probability, statistics, and random processes*. Kappa Research, LLC, 1994, vol. 7.
- [136] “White noise.” [Online]. Available: https://www.probabilitycourse.com/chapter10/10_2_4_white_noise.php
- [137] E. M. Stein and R. Shakarchi, *Complex analysis*. Princeton University Press, 2010, vol. 2.
- [138] S. R. Garcia and R. A. Horn, *A second course in linear algebra*. Cambridge University Press, 2017.
- [139] “Autocorrelation.” [Online]. Available: <https://en.wikipedia.org/wiki/Autocorrelation>
- [140] “Monte carlo method.” [Online]. Available: https://en.wikipedia.org/wiki/Monte_Carlo_method#:~:text=Monte%20Carlo%20methods%2C%20or%20Monte,might%20be%20deterministic%20in%20principle.